CHAOS AND COMPLEXITY OF MAGNETIC SPIN-WAVE SOLITARY

WAVE DYNAMICS IN THE COMPLEX CUBIC QUINTIC

GINZBURG-LANDAU EQUATION

by

Justin Quinn Anderson

A thesis submitted to the Faculty and the Board of Trustees of the Colorado School of Mines in partial fulfillment of the requirements for the degree of Doctorate of Philosophy (Physics).

Golden, Colorado

Date _____

Signed: _____
Justin Quinn Anderson

Signed: _____
Dr. Lincoln D. Carr
Thesis Advisor

Signed: _____
Dr. Mingzhong Wu
Thesis Advisor

Golden, Colorado

Date _____

Signed: _____
Dr. Uwe Greife
Professor and Head
Department of Physics

ABSTRACT

We report the development, implementation and complete experimental vindication of a model for complex dynamical behaviors in spin wave envelopes propagating in nonlinear, dissipative driven, damped systems. These backward volume spin waves evolve under attractive nonlinearity in active magnetic thin film-based feedback rings where the major loss mechanisms present in the film are directly compensated by periodic linear amplification. Such a quasi-conservative evolution allows for the self-generation of spin waves and the observation of long-time behaviors $\mathcal{O}(\text{ms})$ which persist for hundreds to tens of thousands of the fundamental round trip time $\mathcal{O}(100 \text{ ns})$.

The cubic-quintic complex Ginzburg-Landau equation is developed as a predictive, descriptive model for the evolution of spin wave envelopes. Over 180000 nodes hours of computation are used to execute more than 10000 simulations in order characterize the model's six dimensional parameter space. This exploration of parameter space was conducted in full generality, spanning a minimum of eight orders of magnitude for each of three loss terms and five orders of magnitude for higher order nonlinearities. Nine distinct classes of behavior were identified, including four categories of dynamical pattern formation. This work contains the first predicted long time dynamical behaviors for spin waves and analogous physical systems.

All four categories of dynamical pattern formation that were identified numerically were then cleanly realized experimentally. Additionally we observed the first known examples of dynamical behaviors for dark solitary waves self-generated under attractive nonlinearity. Our experimental verification of these dynamical regimes show that such ideas are not simply theoretical but in fact occur in the real physical world and are observable in an approachable, tunable spin-wave system which matches the conditions of many other real-world physical systems. It further established that the relatively simple cubic-quintic complex Ginzburg-Landau equation provides a highly accurate, effective, and predictive description of complex

spin wave dynamics and should replace the commonly used nonlinear Schrödinger equation for these systems.

Finally, simulations which model the ring dynamics on the scale round trips were conducted using 130000 node hours over 3000 unique numerical simulations. This yielded a robust general solution for stable bright solitary wave trains evolving under periodic amplification which is the numerical equivalent to the bright solitary wave train initial condition perturbed experimentally to generate soliton fractals and chaotic solitons. Using this novel dynamical equilibrium as an initial condition we developed a mechanism for the generation of bright soliton fractals.

Our experimental and numerical works on complex spin wave envelopes in magnetic thin films suggest these systems provide for an approachable, table top, experiment for the study of fundamental nonlinear wave physics. The cubic-quintic complex Ginzburg-Landau model further provides for means for both prediction and verification of results. The physics reported here are expected to be wildly applicable to related fields of physics that are described by isomorphic forms of our model. This includes fields such as nonlinear optics, nonlinear hydrology and Bose-Einstein condensation.

TABLE OF CONTENTS

LIST OF FIGURES

LIST OF TABLES

LIST OF ABBREVIATIONS

nonlinear Schrödinger equation . . . . NLS

spin wave envelope . . . . SWE

backward volume spin wave . . . . BVSW

cubic-quintic complex Ginzburg-Landau equation . . . . CGCGL

yttrium iron garnet . . . . YIG

active magnetic thin film-based feedback ring . . . . AFR

high-performance computing . . . . HPC

ACKNOWLEDGMENTS

Acknowledgements intentionally left blank.

the fool on the hill

sees the sun going down

and the eyes in his head

see the world spinning round.

- Paul McCartney

CHAPTER 1

MOTIVATION AND CONTEXT

We report on the development, evaluation, and experimental vindication of a driven damped model for spin wave envelopes in magnetic thin film-based active feedback rings (AFR); a problem with applications across an extraordinary range of physical systems and fundamental nonlinear dynamical studies. Such systems have typically been modeled by an integrable nonlinear Schrödinger equation (NLS) derived either via a slowly varying envelope approximation or through conservation considerations and a Hamiltonian formalism on an infinite and lossless thin film [1–3]. These conservative models, however, are fundamentally unable to reproduce the complex and chaotic dynamical behaviors that have been experimentally observed in magnetic thin films over the past two decades. Previously observed dynamics include bright and dark envelope solitons [4–10, 10–19], soliton trains [20, 21], möbius solitons [22], Fermi-Pasta-Ulam and spatial recurrence [23, 24], soliton fractals [25], random solitons [26], chaotic spin waves [27–29], multiple solitons [30], and chaotic solitons [31, 32].

Most of these phenomena were observed on AFRs as such feedback geometries are ubiquitous across science and physics in general. Rings are commonly used to study wave dynamics when one seeks to study resonant phenomena such as quantized wavenumber, periodic pumping, self-generation. AFRs, so-called for the presence of periodic linear amplification, allow for the direct compensation of major loss mechanisms present within a propagation medium. This permits one to drive a system into *quasi-conservative* regimes where the major loss mechanisms are directly compensated on the time scale of a single round trip ($\mathcal{O}(100$ ns$)$). This enables the observation of dynamics on scales of several to tens of thousands of round trip times $\mathcal{O}(\text{ms})$. Dissipation would otherwise prohibit dynamics with lifetimes of this order.

A driven, damped model is necessary to account for both the periodic nature of amplification within feedback rings and the sustained losses, nonlinearities and dispersions present within magnetic thin film propagation media. To date, significant research efforts have been made into studying solitons in dissipative physical systems governed by analogous models. A growing body of experimental evidence indicates these systems exhibit strong saturable gains [5, 28]. These considerations, along with an overall desire to develop the simplest model which nonetheless reproduces observed experimental results, suggests that a suitable model may be generated via the phenomenological introduction of gain and loss terms to a standard NLS. This driven damped model, to be called the *cubic-quintic complex Ginzburg-Landau equation* (CQCGL), was developed and evaluated numerically to determine its merit both as a descriptive and predictive modeling equation for the study of spin wave envelope soliton trains driven from equilibrium in active magnetic thin film-based feedback rings.

Significant work, including over 300,000 node hours of computation generating 10 TB of data, have been completed to verify the efficacy of the CQCGL within the context of magnetic thin film-based active feedback rings. This includes the modification and verification of existing NLS evolution codes to include gains and losses as well as the development of scripts for efficiently executing this code on high-performance computing (HPC) environments. HPC was necessary to fully examine the dynamical behavior of solitary waves driven out of equilibrium across a massive six or higher-dimensional parameter space. Robust procedures for post-processing, data management, and the rigorous quantification of complex dynamical behaviors have also been established. This work has resulted in three collaborative publications with an experimental research group at Colorado State University as well as two distinct numerical schemes [31, 33, 34].

This new model has wide applications as isomorphic forms of the nonlinear Schrödinger equation are used to simulate nonlinear phenomena across many distinct physical systems. This includes Ginzburg-Landau type equations that describe the envelope evolution of mode-locked lasers, and superconductivity [35]; the cubic nonlinear Schrödinger equation treats

2

deep water waves [1] and the dynamics of spin wave envelopes in magnetic thin films [36, 37]; a driven damped nonlinear Schrödinger equation models exciton-polariton and magnon Bose-Einstein condensates (BECs) [38]; and the Gross-Pitaevskii equation models the mean field of atomic and molecular BECs [39, 40].

This thesis is organized as follows. In Chapter 2 the necessary background on spin waves, thin films and AFRs will be introduced. The derivation and motivation behind the cubic-quintic complex Ginzburg-Landau equation will be given within Chapter 3. The numerical and analytical methods used to generate and quantify the complex dynamical behaviors reported in this work are introduced in Chapter 4. A numerical exploration of the CQCGLs parameter space is presented in Chapter 5 and the experimental verification of those results is given in Chapter 6. A summary of unpublished work including the development and evaluation of an iterative numerical scheme for the GLNLS is given in Chapter 7. Finally, a summary of results and an outlook on future work are given in Chapter 8.

CHAPTER 2

OVERVIEW OF SPIN WAVES: EXPERIMENT AND THEORY

All of the work presented in this thesis is focused on the excitation, detection or numerical simulation of spin wave envelopes (SWEs) propagating in active magnetic thin film-based feedback rings. This chapter introduces the underlying and important physical features of these waves and the apparatus and film in which they propagate. The information presented in this chapter is influenced significantly by Stancil's *Theory of Magnetic Waves*, MZ Wu's *Nonlinear Spin Waves in Magnetic Film Feedback Rings* and by PhD theses from MZ Wu's group from Scott, Wang and Janantha[2, 41–44]. Those works, and the references therein, are highly recommended for additional reading on the topic.

2.1 Physics of Spin Waves

Spin waves are fundamentally an excitation of a collection of magnetic moments which may then propagate through a material. These waves are called *spin* waves due to the fact that magnetic moments in most materials are primarily determined by the angular momenta of electron spins. Such moments precess if exposed to a fixed external magnetic field. This precession is described by the magnetic torque equation first introduced by Landau and Lifshitz [45],

$$\frac{\mathrm{d}\mathbf{M}}{\mathrm{d}t} = -|\gamma|\mathbf{M} \times \mathbf{H}, \tag{2.1}$$

where here $\mathbf{M}$ is the total magnetization vector, $\mathbf{H}$ is the external magnetic field and γ is the absolute electron gyromagnetic ratio. This type of precession is diagrammed in Figure 2.1 where a magnetic moment $\mathbf{M}$ precesses around an external magnetic field $\mathbf{H}$ applied in the z direction (up). The z-component of the magnetization may be written as $\mathbf{M}_z = \sqrt{\mathbf{M}^2 - \mathbf{m}^2}$ and here $\mathbf{m}$ is the variable component of the precession given by the sum of the x and y components. We note that if the dynamical component is circular, or $\mathbf{m}(t) \propto \exp^{i\omega t}$ where

ω is the frequency of precession, then it follows from Equation 2.1 that the magnitude of the magnetization, $|\mathbf{M}|$, is constant.
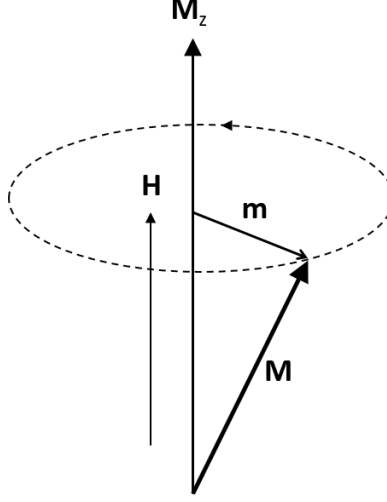
Figure 2.1: Diagram of Magnetic Moment Precession where a magnetization $\mathbf{M}$ is seen precessing about an external field $\mathbf{H}$ applied in the z direction. The z component and variable component of the magnetization are shown as $\mathbf{M_z}$ and $\mathbf{m}$, respectively.

A precession of coupled magnetic moments which propagate within an ordered magnetic medium is termed a spin wave. These coupled moments precess at the same frequency, ω, but typically out of phase, and interact with their neighbors through either magnetic dipolar or exchange effects. Spin waves which are dominated by magnetic dipolar interactions are called *magnetostatic spin waves* or *dipolar spin waves* and spin waves which are dominated by exchange interactions are called *exchange spin waves*. *Magnetostatic spin waves* are the focus of this work and will be discussed in further detail below. A diagram of a spin wave, given by a collection of coupled magnetic moments, is shown in Figure 2.2 where the wavelength λ and propagation vector k are illustrated by arrows. This is a typical example where neighboring magnetic moments are coupled causing them to precess at a fixed frequency but out of phase.

An initial analysis of spin wave dynamics may be made by solving the magnetostatic Maxwell equations within an infinite arbitrary magnetic material. These may be arrived at by applying the limit where dipolar fields dominate the coupling between spins and the
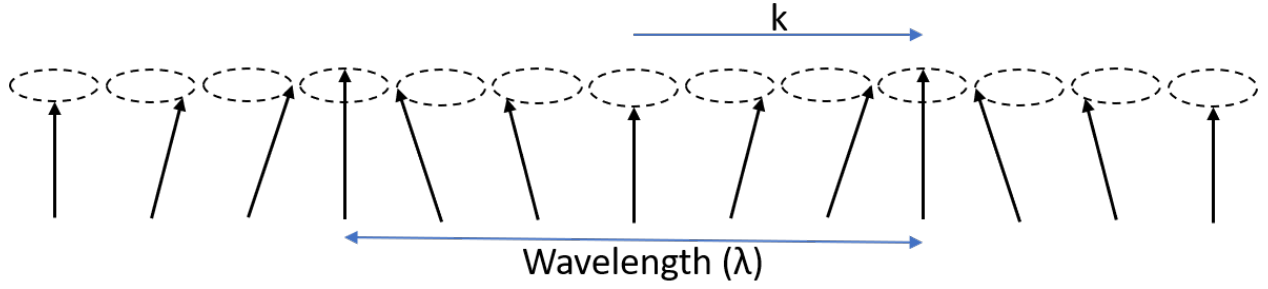
Figure 2.2: Diagram of a Spin wave where nearby magnetic moments coupled via exchange or magnetic dipolar interactions precess at a fixed frequency but slight of phase with their neighbors. The wave length λ and propagation vector k are shown.

exchange interaction can be ignored, given by $k_0 \ll k \ll \pi/a$ where a is the spacing between spins in the material and $k_0 \approx \omega(k)/c$ and c is the speed of light. Under this approximation only the slow waves which are strongly coupled to the magnetic material are considered and fast electromagnetic waves that have weaker coupling and vastly lower wavenumbers at the same frequency are ignored. The magnetostatic approximation to Maxwell's equations are given by

$$\nabla \times \mathbf{h} = 0, \tag{2.2}$$
$$\nabla \cdot \mathbf{b} = 0, \tag{2.3}$$
$$\nabla \times \mathbf{e} = i\omega\mathbf{b}. \tag{2.4}$$

Here $\mathbf{h}$ is the variable component of the full magnetic field, $\mathbf{H} = H_0\hat{\mathbf{z}} + \mathbf{h}$ and H_0 is the external field amplitude along the $\hat{z}$ direction. The associated variable electric field is given by $\mathbf{e}$ and $\mathbf{b}$ and $\mathbf{h}$ are related by

$$\mathbf{b} = \bar{\boldsymbol{\mu}} \cdot \mathbf{h}, \tag{2.5}$$

where $\bar{\boldsymbol{\mu}}$, the permeability tensor, is defined by

$$\bar{\boldsymbol{\mu}} = \mu_0 \left(\bar{\boldsymbol{I}} + \bar{\boldsymbol{\chi}}\right). \tag{2.6}$$

Here $\bar{\boldsymbol{I}}$ is the unit matrix and $\bar{\boldsymbol{\chi}}$ is the magnetic susceptibility tensor. The magnetostatic Maxwell equations are derived assuming constant tensors and uniform plane wave solutions:

6

$\{\mathbf{h}, \mathbf{e}\} \propto \exp\left(-\mathbf{k} \cdot \mathbf{r} - i\omega t\right)$. The permeability tensor in the absence of exchange interaction and anisotropy is

$$\hat{\boldsymbol{\mu}} = \mu_0 \begin{bmatrix} 1 + \chi & -i\kappa & 0 \\ i\kappa & 1 + \chi & 0 \\ 0 & 0 & 1 \end{bmatrix}. \tag{2.7}$$

Here $\chi = \omega_M \omega_H / (\omega_H^2 - \omega^2)$ and $\kappa = \omega_M \omega / (\omega_H^2 - \omega^2)$ and the characteristic frequencies, ω_M and ω_H are given by

$$\begin{aligned} \omega_M &= |\gamma| \mathbf{M}_s, \\ \omega_H &= |\gamma| \mathrm{H}. \end{aligned} \tag{2.8}$$

where γ is the absolute electron gyromagnetic ratio and μ_0 is the permeability of free space and M_s is the saturation magnetization. Equation 2.2 suggests we may define a scale potential

$$\mathbf{h} = -\nabla \psi. \tag{2.9}$$

Combining equations 2.3, 2.7, and 2.9 one may obtain a differential equation for the magnetostatic scalar potential

$$(1 + \chi)\left(\partial_{xx}\psi + \partial_{yy}\psi\right) - i\kappa \partial_x \partial_y \psi + i\kappa \partial_y \partial_x \psi + \partial_{zz}\psi = 0,$$

assuming ψ is a well behaved function we have $\partial_{xy}\psi = \partial_{yx}\psi$ and may write

$$(1 + \chi)\left(\frac{\partial^2 \psi}{\partial x^2} + \frac{\partial^2 \psi}{\partial y^2}\right) + \frac{\partial^2 \psi}{\partial z^2} = 0, \tag{2.10}$$

which is the well known Walker equation that describes magnetostatic modes in homogeneous magnetic media, and we have assumed χ and $\mathbf{k}$ are independent of position.

Assuming plane wave solutions, $\psi \propto \exp^{\mathbf{k} \cdot \mathbf{r}}$, to Equation 2.10 we may derive the dispersion relation for an unbounded magnetic sample without exchange interactions

$$(1 + \chi)\left(k_x^2 + k_y^2\right) + k_z^2 = 0. \tag{2.11}$$

Ultimately yeilding an expression for the spin wave dispersion relation

$$\omega^2 = \omega_H \left(\omega_H + \omega_M \sin^2(\theta)\right), \tag{2.12}$$

where one makes use of the magnetic susceptibility for an unbounded magnetic sample in the absence of exchange interactions and we have θ as the propagation angle with respect to $\hat{\boldsymbol{z}}$. Note there are two limiting cases for $\theta = 0$ and $\theta = \pi/2$ corresponding to an external field perpendicular and parallel to propagation. It is also worth highlightning that the frequency degeneracy in Equation 2.12 is completed addressed by including finite boundaries or exchange interaction. Both are considered below. Equation 2.12 may also be found by looking for nontrivial solutions of the constitutive relationship between $\mathbf{m}$ and $\mathbf{h}$ in the magnetostatic limit, or by solving the maxwell boundary problem in a finite sample for the so called uniform precession modes that are characterized by a magnetization that precesses in-phase throughout the entire sample.

2.1.1 Magnetostatic Approximation

The magnetostatic approximation warrants further discussion before we move forward, as it underpins all derivations present in thesis including that of our models. If one fully treats a plane wave propagating parallel to an applied field within a magnetic material you arrive at two sets of propagating waves with opposite polarization. The polarization which matches the natural precession of the magnetization, given by Equation 2.1, interacts strongly with the medium while the opposite polarization does not. The functional result is these two sets of waves can have vastly different wavenumbers for a given frequency, or vastly different frequencies for a given wavenumber. The waves that couple with the medium are usually called *slow spin waves* while the waves which do not are called *fast electromagnetic waves*. Qualitatively the magnetostatic approximation is the process of ignoring the *fast electromagnetic waves* in favor of the *slow spin waves*. This is justified since at a given wavenumber their excitation frequencies can vary by orders of magnitude.

More formally if we write down Maxwell's equations for a uniform plane wave propagating within a magnetized medium at any arbitrary direction we arrive at

$$\mathbf{h} = \frac{k_0^2 \mathbf{m} - \mathbf{k}\mathbf{k} \cdot \mathbf{m}}{k^2 - k_0^2}, \tag{2.13}$$

$$\mathbf{e} = \frac{\omega \mu_0 \mathbf{k} \times \mathbf{m}}{k_0^2 - k^2}, \tag{2.14}$$

$$\nabla \times \mathbf{h} = \frac{k_0^2 \mathbf{k} \times \mathbf{m}}{k_0^2 - k^2}. \tag{2.15}$$

In the limit of $|\mathbf{k}| \gg |\mathbf{k}_0|$ that Equation 2.13 remains finite so long as $\mathbf{k} \cdot \mathbf{m} \neq 0$ since there are terms quadratic in k in both the numerator and denominator. On the other hand equations 2.14 and 2.15 decay as $1/k$ in this limit. The application this limit, to first order, yields the magnetostatic approximation to Maxwell's equations given in equations 2.2, 2.3 and 2.4. We note both that this approximation is also valid in the $|\mathbf{k}_0| \gg |\mathbf{k}|$ limit and if $\mathbf{k} \cdot \mathbf{m} = 0$ since both Equation 2.13 and Equation 2.14 still vanish for large k.

As mentioned earlier *dipolar spin waves* or *magnetostatic spin waves* propagate when the coupling between spins is dominated by dipolar fields rather than the exchange interaction. Again, this given by the limit $k_0 \ll k \ll \pi/a$ where a is the spin spacing. This is most readily visualized if one solves the full, non-magnetostatic Maxwell's equations to find a version of the spin wave dispersion, Equation 2.12, where the effects of exchange are included. This is given by,

$$\omega^2 = \left(\omega_\mathrm{H} + \omega_\mathrm{M}\lambda_\mathrm{ex}k^2\right)\left(\omega_\mathrm{H} + \omega_\mathrm{M}\left(\lambda_\mathrm{ex}k^2 + \sin^2\theta\right)\right), \tag{2.16}$$

where again θ is the propagation angle with respect to $\hat{\mathbf{z}}$ and λ_ex is an exchange constant. As $\lambda_\mathrm{ex}k^2 \to 0$ we return to the expression for dispersion derived from the magnetostatic approximation, Equation 2.12. The exchange term $\lambda_\mathrm{ex}k^2$ will begin to impact dispersion as the magnitude of k increases.

This is shown in Figure 2.3 where the $\theta = \pi/2$ is shown as dashed red and $\theta = 0$ as solid blue. We set $\omega_\mathrm{H}/\omega_\mathrm{M} = 0.5$ and use $\lambda_\mathrm{ex} = 3.2 \times 10^{-12}\mathrm{rad/cm}$, the value measured for YIG films at microwave frequencies. We see that frequency does not develop a strong wavenumber dependence until well after $k = 10^4$ rad/cm. The region without wavenumber
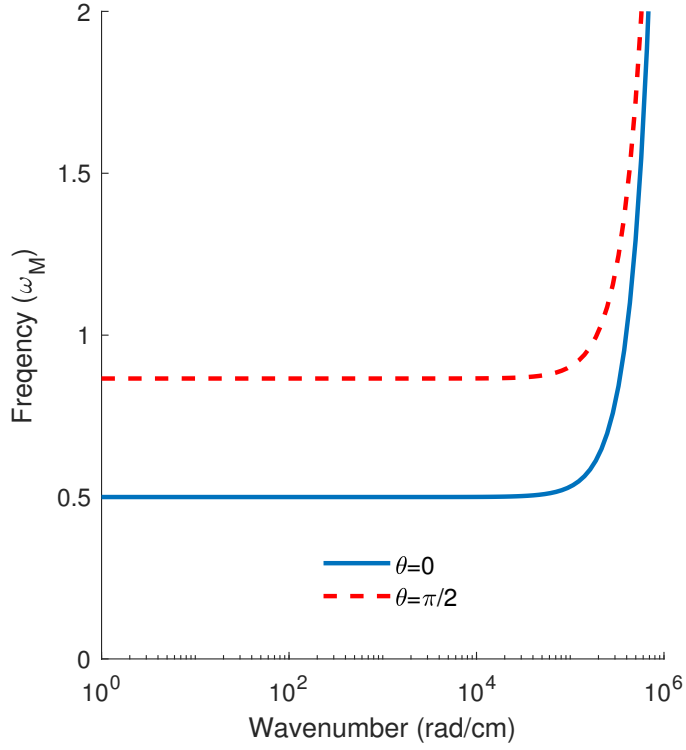
Figure 2.3: Effect of exchange interaction on spin wave dispersion where the case of $\theta = 0$ is shown in solid blue and $\theta = \pi/2$ as dashed red. In both cases the frequency does not develop a strong dependence on wavenumber until after $k = 10^4$ rad/cm, well beyond where the magnetostatic approximation remains valid. Spin waves below this threshold are *dipolar spin waves* and those in the exponential region are *exchange spin waves*. $\omega_{\mathrm{H}}/\omega_{\mathrm{M}} = 0.5$ and $\lambda_{\mathrm{ex}} = 3.2 \times 10^{-12}$ rad/cm for YIG films.

dependence, $\lambda_{\text{ex}}k^2 \ll 1$, is where *dipolar spin waves* or *magnetostatic spin waves* propagate, and *exchange spin waves* propagate in the exponential tail.

2.2   Spin Waves in Magnetic Thin Films

Consider now a magnetostatic spin wave propagating within a finite geometry (a thin magnetic film) of thickness d surrounded by dielectrics. We seek to solve Walker's Equation within the limiting case of a tangentially magnetized film with $\mathbf{k} \parallel \mathbf{H}_0$. Such a geometry, corresponding to $\theta = 0$ in equation 2.12, and supports the propagation of backwards volume spin waves which are the focus of this thesis. The case of $\mathbf{k} \perp \mathbf{H}_0$ supports surface spin waves while a normally, $\theta = \frac{\pi}{2}$, magnetized film supports forward volume spin waves. Neither of these cases are explicitly considered here but are covered in detail in the works of Stancil and Wu [2, 41]. All three excitation types will be briefly discussed below.

If a spin wave is excited within a fully saturated thin film and allowed to reach a steady state one can solve the boundary condition problem assuming the propagation of guided plane waves and their reflections. This yields a transcendental form of the dispersion relation for backward volume spin waves in a thin film,

$$\tan\left(\frac{kd}{2\sqrt{-(1+\chi)}} - \frac{(n-1)\pi}{2}\right) = \sqrt{-(1+\chi)}. \tag{2.17}$$

Kalinikos derived an approximate dispersion relation for the lowest order mode ($n = 1$) which may be explicitly solved for ω [46]. His result is

$$\omega^2 = \omega_{\text{H}}\left[\omega_{\text{H}} + \omega_{\text{M}}\left(\frac{1 - e^{-kd}}{kd}\right)\right]. \tag{2.18}$$

We note that in the limit of an infinite thin film, $d \to \infty$, Equation 2.18 reduces to Equation 2.12 in the appropriate $\theta = 0$ case. The approximation is valid only in the small precession angle limit where the variable magnetization is much less than the saturation magnization, $\mathbf{m} \ll \mathbf{M}_{\text{s}}$. This approximation was further derived under the magnetostatic condition and remains strictly valid only when $k_0 \ll k \ll \pi/a$.
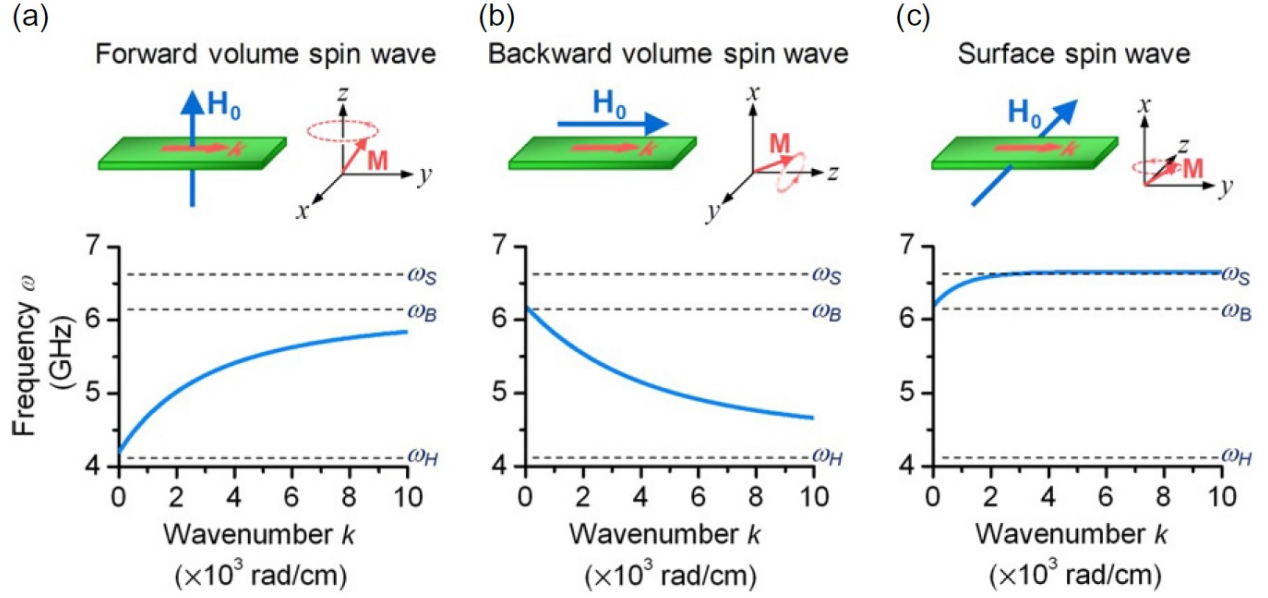
Figure 2.4: Dispersion for (a) forward volume, (b) backward volume and (c) surface spin waves in magnetic thin films. Reprinted with permission from Elsevier [41].

The geometry and Kalinikos derived expressions for the lowest order mode dispersion relation are plotted for (a) forward volume, (b) backward volume and (c) surface spin waves in Figure 2.4. In each case the orientation of the external magnetic field is illustrated relative to the film and the direction of propagation. The dispersion relations were calculated for a YIG film where $4\pi\mathbf{M}_\mathrm{s} = 1750$ G with an external saturation field magnitude of $H = 1500$ Oe. This figure is reprinted with permission. ω_H is given in 2.8 and the remaining characterstic frequences which describe the spin wave passbands are

$$\begin{aligned}
\omega_\mathrm{B} &= |\gamma|\sqrt{\mathbf{H}(\mathbf{H} + 4\pi\mathbf{M}_\mathrm{S})}, \\
\omega_\mathrm{S} &= |\gamma|(\mathbf{H} + 4\pi\mathbf{M}_\mathrm{S}/2).
\end{aligned} \tag{2.19}$$

We highlight that the forward volume spin waves are so called due to having a positive group velocity, whereas backward volume spin waves have a negative group velocity. This is evident in the dispersion curves in Figure 2.4(a) and (b). Surface spin waves also exhibit a positive group velocity. We define group velocity as,

$$v_\mathrm{g} = \frac{\partial\omega(k)}{\partial k}. \tag{2.20}$$

12

It is also crucial to note that the spin wave passband for backward and forward volume spin waves is entirely defined by the characteristic frequencies ω_B and ω_H which are both highly dependent on the magnitude of the external magnetic field. This allows for the direct tuning of spin wave frequency. The dispersion coefficient may also be tuned by varying the direction of the external magnetic field where the dispersion coefficient is defined as,

$$D = \frac{\partial^2 \omega(k)}{\partial k^2}, \tag{2.21}$$

This results in negative dispersion for forward volume and surface spin waves, and positive dispersion for backward volume waves. This an important degree of freedom for designing and running experiment.

2.3   Spin Wave Nonlinearity

There are two main sources of nonlinearity for spin waves in magnetic thin films. The first we will consider is the shift in frequency due to spin wave amplitude. Qualitatively if one considers the precession of a single magnetic moment, such as in Figure 2.1, any increase in precession angle (and thereby the magnitude of $\mathbf{m}$) will result in a decrease in $\mathbf{M_z}$ through the expression $\mathbf{M_z} = \sqrt{\mathbf{M}^2 - \mathbf{m}^2}$. This change in $\mathbf{M_z}$ can then result in a frequency shift of the dispersion curve.

Thus, when the precession angle becomes appreciable one must replace $\mathbf{M_s}$ in the dispersion relation with $\mathbf{M_z}$. Equation 2.18's dependence on $\mathbf{M_s}$ comes from the ω_M term, defined by Equation 2.8. The relation between $\mathbf{M_s}$ and $\mathbf{M_z}$ is simply derived. In a saturated sample one has,

$$\mathbf{M_s}^2 = \mathbf{M_x^2} + \mathbf{M_y^z} + \mathbf{M_z^2} \tag{2.22}$$

which may be readily solved for $\mathbf{M_z}$ for the case of circular precession,

$$\mathbf{M_z} = \mathbf{M_s}\sqrt{1 - \frac{|\mathbf{M_x}|^2 + |\mathbf{M_y}|^2}{2\mathbf{M_s^2}}} = \mathbf{M_s}\sqrt{1 - \frac{\mathbf{m}^2}{2\mathbf{M_s^2}}}. \tag{2.23}$$

Here $\mathbf{m}$ is the variable magnetization. We may define a unitless magnetization amplitude as

$$|u(z,t)|^2 = \frac{\mathbf{m}^2}{2\mathbf{M_s}}. \tag{2.24}$$

Assuming $|u| \ll 1$ one may further reduce Equation 2.23 to

$$\mathbf{M_z} = \mathbf{M_s}\sqrt{1 - |u|^2} \approx \mathbf{M_s}\left(1 - |u|^2\right). \tag{2.25}$$

The case of elliptical precession for backward volume spin waves is considered by Wu and Boardman and gives,

$$\mathbf{M_z} = \mathbf{M_s}\left[1 - \frac{1}{2}\left(1 + \frac{\omega_B^2}{\omega_H^2}\right)|u|^2\right] \tag{2.26}$$

This frequency shift is most easily identified by examining the dispersion relation for magnetostatic spin waves given in Equation 2.12 with $\theta = \pi/2$ corresponding to backward volume spin waves, our case of interest, and with $\mathbf{M_z}$ substituted for $\mathbf{M_s}$. This gives,

$$\omega^2 = \omega_H(\omega_H + \mathbf{M_z}). \tag{2.27}$$

In both the elliptical and circular precession cases we can see how an increase in spin wave power $|u|^2$ results in a decrease in $\mathbf{M_z}$, which would result in a decrease in frequency. This implies that nonlinearity is negative for backward volume spin waves. We may confirm this by substituting $\mathbf{M_s}$ in the dispersion relation with $\mathbf{M_z}$ and then directly evaluating the spin wave nonlinearity coefficient given by,

$$N = \frac{\partial \omega}{\partial |u|^2}. \tag{2.28}$$

For the elliptical precession of backward volume spin waves with ω close to ω_B we have,

$$N = -\frac{\omega_H\omega_M}{4\omega_B}(1 + \frac{\omega_H^2}{\omega_B^2}). \tag{2.29}$$

The axis of the elliptical precession was chosen arbitrarily to derive Equation 2.29. The other equally valid choice results in the swaping of ω_B and ω_H in Equation 2.26 which yields the following expression for the nonlinearity coefficientm

$$N = -\frac{\omega_H\omega_M}{4\omega_B}(1 + \frac{\omega_B^2}{\omega_H^2}). \tag{2.30}$$

When $\mathcal{O}(\omega_{\mathbf{H}}) \approx \mathcal{O}(\omega_{\mathbf{B}})$ both are close to $-\omega_{\mathrm{H}}\omega_{\mathrm{M}}/4\omega_{\mathrm{B}}$.

As with dispersion, the sign of the nonlinearity coefficient for spin waves in magnetic thin films can be adjusted by varying the direction of the external magnetic field. We determined above that the nonlinearity coefficient is negative for backward volume spin waves. It is also negative for surface spin waves, but is positive for forward volume waves. The sign of the effectively nonlinear ND will be important to determining the type of spin wave envelope excitation which can observed in magnetic thin films, and will be discussed in detail in Chapter 6. For now we mention again this tunability is a powerful degree of freedom for designing and running experiment.

The type of nonlinearity discussed so far and described by Equation 2.28 is a result of conservative four wave mixing. For spectrally narrow peaks in magnetic thin films the four wave mixing conservation equations are given by,

$$
\begin{aligned}
2\omega_1 &= \omega_2 + \omega_3, & (2.31) \\
2k_1 &= k_2 + k_3, & (2.32)
\end{aligned}
$$

and describe two modes, k_2 and k_3 with sufficient amplitude interacting to generate a third mode, k_3. If ring power is further increased additional modes may be generated via this four wave mixing process, resulting in a uniform frequency comb with spacing $f_{\mathrm{s}} = |\omega_1 - \omega_2|$.

This development process for increasing ring gain is shown in Figure 2.5 where in (a) the location of the original ring eigenmodes and the first mode generated via four wave mixing are shown on the dispersion curve for a backward volume spin wave. Figure 2.5(b) shows the development of additional equispaced modes through four wave mixing as ring gain is increased further. This process is known as *self-generation* and we will be discussed later.

The additional form of nonlinearity experienced by spin waves in magnetic thin films are the three wave splitting of one mode (ω_0) into two new half-frequency modes and three wave confluence where two half-frequency modes combine into a new mode (ω_3). These are respectively described by,
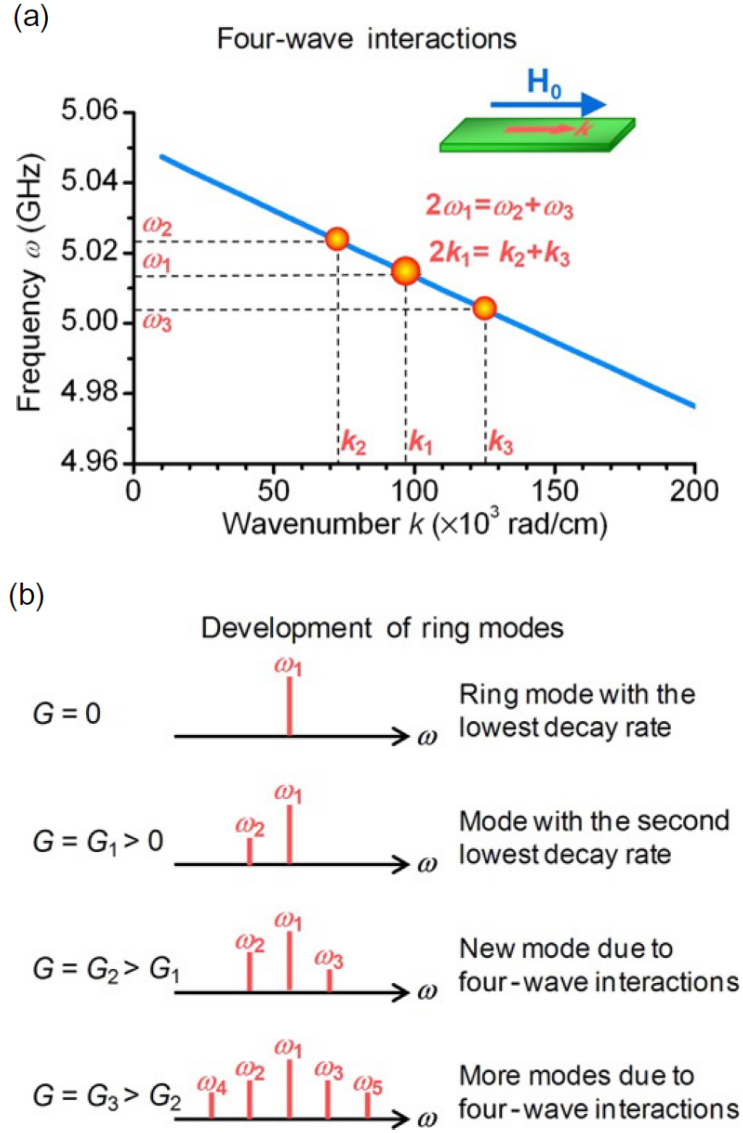
Figure 2.5: Generation of modes via four wave mixing where (a) shows the location of the new and old modes on the dispersion curve for backward volume spin waves and (b) shows development of additional ring eigenmodes through four wave mixing. Reprinted with permission from Elsevier [41].

$$\omega_0 = \omega_1 + \omega_2,$$
$$k_0 = k_1 + k_2,$$

and

$$\omega_1 + \omega_2 = \omega_3,$$
$$k_1 + k_2 = k_3.$$

For the case of backward volume waves these three wave processes can be considered an additional source of nonlinear losses where energy leaves the system via the splitting of low wavenumber ($\mathcal{O}(10)$ rad/cm) modes into modes with high wavenumbers ($\mathcal{O}(10^5)$ rad/cm). Such high wavenumber modes are not detectable in our experiments, as will be discussed later Chapter 6. Three wave modes may also be forbidden via conservation considerations by increasing the external field strength until no half-frequency bands remain in the passband, this occurs at around 600 Oe.

2.4 Active Magnetic Thin Film-based Feedback Rings

All of the experimental data presented in this work was generated on a single system at Colorado Statue University called an Active Magnetic Thin Film-based Feedback Ring (AFR). This system also informed the derivation and simulation of our model, to be discussed in chapters 3, 5 and 7. Data gathered on the AFR is presented in chapters 6 and 7.

A schematic of the AFR used is shown in Figure 2.6 and the system is composed of two main components: (1) an electronic feedback loop containing an amplifier/attenuator pair that is coupled via two microwave transducers to a (2) Ytrrium-Iron-Garnet thin film propagation media. An oscilliscope and spectrum analyzer are attached to the feedback loop via a directional coupler to allow for real time recording of time and frequency data. A microwave source may also be attached to the feedback loop using a directional coupler after the attenuator/amplifier pair but that is not used in any work presented here.
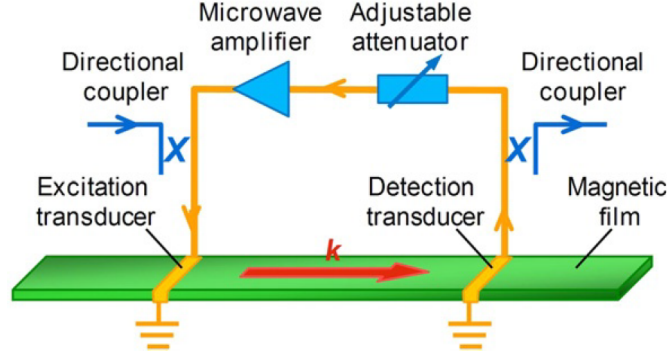
Figure 2.6: Schematic of an Active Magnetic Thin Film-based feedback ring that is constructed of an electronic feedback look containing a variable anttenuator and a fixed amplifier coupled to a Yttrium-Iron-Garnet thin film via two microwave transducers. Directional couplers also allow the feedback ring to be attached to a microwave source or to an oscilliscope or spectrum analyzer for the in-situ driving, observarion or recording of ring voltage. Reprinted with permission from Elsevier [41].

The AFR operates as an effective periodic boundary conditions for the spin wave propagation media, coupled with periodic amplification. Signals that are observed in the detection transducer are boosted, and then fed back into the film after a fixed delay, ϕ_e. The fixed electronic feedback loop delay, $\mathcal{O}(10 \text{ ns})$, is an order of magnitude smaller than the spin wave propagation time in the thin film, $\mathcal{O}(100 \text{ ns})$. Clean feedback is possible due to the fact that the films used are much longer than the separation between the excitation and detection transducers. Combined with 45 degree cuts on the film ends these considerations prevent end reflections from interfering with any dynamics circling the ring.

A direct consequence of the ring geometry is a resonance condition for spin wave ring eigenmodes,

$$\phi(f) = k(f)\ell + \phi_e = 2\pi n, \tag{2.33}$$

where ℓ is the transducer separation, ϕ_e is the above mentioned electronic phase shift introduced by the feedback loop, and k is the spin wave wavenumber for a given frequency. It is important to note that the spacing between ring eigenmodes is not fixed, owing to the nonlinearity discussed previously in Section 2.3.

The feedback ring is called active due to the present of periodic, linear amplification. This periodic gain can be tuned to compensate for the major loss mechanisms present within the thin film. Such a direct form of loss compensation enables the system to operate in an *quasi-conservative* regime where, over many round trips, energy is conserved in an average sense. It is this feature that enables the observation of complex dynamical behaviors with characteristic periods ranging from tens to hundreds of round trip times and that may persist for tens of thousands.

Active feedback also enables the so-called *self-generation* of spin waves where ring gain is increased until the lowest loss eigenmode begins to circulate. As additional ring eigenmodes enter the system they interact via four wave mixing, defined earlier in Equation 2.31. As ring gain is increased more, additional modes will be generated from this process ultimately generating an equispaced frequency comb. This process is shown schematically in Figure 2.5(b) and experimentally in Figure 2.7. In both cases gain is increased from top to bottom. Figure 2.7 shows the spectral (left) and temporal (right) ring data as gain is increased from where a single eigenmode circulates a ring to the full realization of a equispaced frequency comb in, corresponding to a bright solitary wave train. All experiments in this thesis use self-generated spin waves.

Additional considerations the AFR places on modeling spin wave dynamics will be discussed in Chapter 3 and a detailed description of running the AFR system as well as its design considerations is presented in crefchpt:nine.

2.5 Fitting Parameters

In this section we will detail the procedure for determining the experimental parameters via fitting. We explicit about our assumptions and do our best to quantify our error rigorously. The fitting is rather straight forward and involves two fitting parameters and two estimated parameters.

Experimentally we are able to record two curves as a function of frequency by attaching the YIG film to a Vector Network Analyzer; these are (1) transmission as a function of
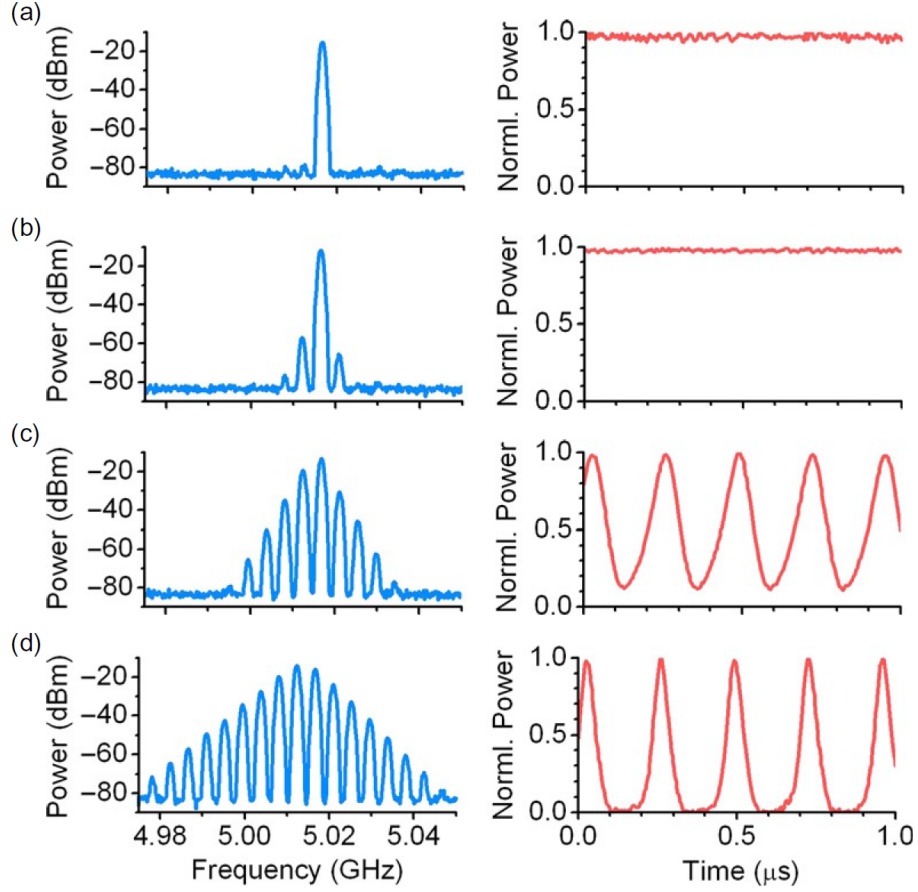
Figure 2.7: Spin wave self-generation. Experimental self-generation of a bright solitary wave through four-wave mixing as ring gain is increased. The left column shows with increasing gain: (a) the lowest loss ring eigenmode, (b) four wave mixing of the two lowest loss ring eigenmodes, (c) generation of additional modes through four wave mixing, and (d) a fully realized equispaced frequency comb corresponding to a bright soliton. The right column shows the equivalent temporal voltage data as gain is increased. Reprinted with permission from Elsevier [41].

frequency, $\mathrm{dB}(f)$, and (2) Phase shift as a function of frequency, $\phi(f)$. Our ultimate goal is to the determination of the Dispersion relation, from which we can estimate the experimental parameters for group velocity, v_g, dispersion, D, and nonlinearity, N.

This is accomplished by exploiting the ring resonance condition, Equation 2.33, and scaling by the observed passband,

$$k(f) = \frac{\phi(f) - \phi_e}{\ell}, \tag{2.34}$$

where ℓ is the transducer sepataion and ϕ_e is an electronic phase shift introduced by the VNA. We have access to the phase as a function of frequency from the VNA and ℓ is known, so we may solve for the wavenumber as a function of frequency using Equation 2.34. The unknown, ϕ_e, may be determined by graphically locating the high frequency end of the backward volume spin wave(BVSW) passband, or the ferromagnetic resonance frequency. This is a characteristic frequency for the problem given by, ω_B, and corresponds to the lowest mode, $k = 0$. Explicitly we have $k(\omega_\mathrm{B}) = 0$ which implies $\phi(\omega_\mathrm{B}) = \phi_e$ for the VNA loop.

Having determined $k(f)$ we may invert the data and identify a curve for $2\pi f(k) = \omega(k)$. We may use this curve to estimate our parameters directly, and may also fit a known expression for $\omega(k)$ and use that to do our parameter estimation. The known expression for the dispersion relation, valid for $kd \ll 1$, is given by

$$\omega(k) = \left[\omega_\mathrm{H}^2 + \omega_\mathrm{H}\omega_\mathrm{M}\left(\frac{1 - \mathrm{e}^{-kd}}{kd}\right)\right]^{1/2}, \tag{2.35}$$

where the characteristic frequencies ω_H and ω_M will be defined below and d is the Yttrium-Iron-Garnet thin film thickness. The characteristic frequencies are defined by,

$$\omega_{\mathrm{H}} = \gamma \left(\vec{H}_0 + \vec{H}_{\mathrm{a}} \right) = \gamma \vec{H}, \tag{2.36}$$

$$\omega_{\mathrm{B}} = \gamma \left[\vec{H} \left(\vec{H} + 4\pi \vec{M}_{\mathrm{S}} \right) \right]^{1/2}, \tag{2.37}$$

$$\omega_{\mathrm{S}} = \gamma \left(\vec{H} \frac{4\pi \vec{M}_{\mathrm{S}}}{2} \right), \tag{2.38}$$

$$\omega_{\mathrm{M}} = \gamma 4\pi \vec{M}_{\mathrm{S}}. \tag{2.39}$$

where γ is the gyromagnetic ratio and $\vec{H} = \vec{H}_0 + \vec{H}_{\mathrm{a}}$ is the total field defined by the external tangential magnetic field and the internal anisotropy field. We may use dispersion relation, given by Equation 2.35, to determine the experimental values for dispersion, group velocity and nonlinearity. These ex[ressions, evaluated for $k = 0$ are given by

$$D = \left. \frac{\partial^2 \omega(k)}{\partial k^2} \right|_{k=0} = \frac{\omega_{\mathrm{M}} \omega_{\mathrm{H}} d^2}{2\omega_{\mathrm{B}}} \left[\frac{1}{3} - \frac{\omega_{\mathrm{M}} \omega_{\mathrm{H}}}{8\omega_{\mathrm{B}}} \right], \tag{2.40}$$

$$V_{\mathrm{g}} = \left. \frac{\partial \omega(k)}{\partial k} \right|_{k=0} = -\frac{\omega_{\mathrm{M}} \omega_{\mathrm{H}} d}{4\omega_{\mathrm{B}}}. \tag{2.41}$$

The expression for nonlinearity, evaluated for $k = 0$ and $|u|^2 = 0$ is given by

$$N = \left. \frac{\partial \omega(k, |u|^2)}{\partial |u|^2} \right|_{k=0, |u|^2=0} = -\frac{\omega_{\mathrm{H}} \omega_{\mathrm{M}}}{2\omega_{\mathrm{B}}}. \tag{2.42}$$

There are several distinct sources of error involved this process. First, have error in our estimation of ω_{B} as graphically isolating its location is the most subjective part of the overall fitting process. Second, there are measurements errors for both ℓ and $\vec{H}_0$. Finally, if we choose to fit the dispersion we will have errors in our fit based on how far into k we choose to fit. Explicitly the dispersion curve we are fitting is valid for $kd \ll 1$, which means we can evaluate $k = \mathcal{O}(100\mathrm{rad/cm})$. The total passband is generally $\mathcal{O}(400\mathrm{rad/cm})$. Detailed estimations of the error if we vary the location of ω_{B} and the extent of the fit in k yields percent errors for parameter estimation below 5%.

CHAPTER 3

A MODEL OF SPIN WAVE ENVELOPE DYNAMICS

In this chapter we introduce the model used within this thesis to numerically evaluate spin wave envelope solitary wave dynamics within active magnetic thin thilm-based feedback rings. We begin with a simple derivation of the nonlinear Schrödinger equation using the slowly varying envelope approximation. We then explore and justify the modifications used to arrive at the our governing model: the cubic-quintic complex Ginzburg-Landau equation. As discussed in Section 1 this model is used as a descriptive and predictive tool for the study of complex nonlinear dynamics.

3.1 Nonlinear Schrödinger Equation

As detailed in Section 2.3 the substitution of $\mathbf{M_z}$ into the spin wave dispersion relation introduces a dependence on the magnetization amplitude $|u|^2$. The general functional form of a spin wave dispersion may therefore be written as

$$\omega = f\left(\omega, k, |u|^2\right). \tag{3.1}$$

Assuming spin wave propagation in the form of an envelope modulated carrier wave at an operating point (ω_0, k_0) such that

$$u(z,t) \propto e^{i(\omega_0 t - k_0 z)}. \tag{3.2}$$

If we then consider small modulations about the operating point defined by

$$\begin{aligned} k &= k_0 + \Delta k, \quad \Delta k \ll k_0 \\ \omega &= \omega_0 + \Delta\omega, \quad \Delta\omega \ll \omega_0, \end{aligned} \tag{3.3}$$

where a small perturbation in frequency $\Delta\omega$ results in a change of the same order in wave number, Δk. A tailor expansion of the general dispersion, Equation 3.1, about the operating

point yields

$$\omega - \omega_0 = \frac{\partial \omega}{\partial k} (k - k_0) + \frac{1}{2} \frac{\partial^2 \omega}{\partial k^2} (k - k_0)^2 + \frac{\partial \omega}{\partial |u|^2} + O\left((k - k_0)^3\right), \tag{3.4}$$

where we define group velocity, v_g, dispersion coefficient, D, and the nonlinearity coefficient, N in the usual way,

$$\begin{aligned} v_g &= \frac{\partial \omega(k)}{\partial k}, \\ D &= \frac{\partial^2 \omega(k)}{\partial k^2}, \\ N &= \frac{\partial \omega(k)}{\partial |u|^2}. \end{aligned} \tag{3.5}$$

In terms of usual operator language we have

$$\begin{aligned} \Delta \omega &= \omega - \omega_0 = i \frac{\partial}{\partial t} \\ \Delta k &= k - k_0 = -i \frac{\partial}{\partial z}. \end{aligned} \tag{3.6}$$

Combining equations 3.4, 3.5 and 3.6 we arrive at a partial differential equation describing the evolution of spin wave envelopes in a dispersive , nonlinear medium typicall known as nonlinear Schrödinger equation (NLS)

$$i\left(\frac{\partial}{\partial t} + v_g \frac{\partial u}{\partial z}\right) u = -\frac{1}{2} D \frac{\partial^2 u}{\partial z^2} + N|u|^2 u, \tag{3.7}$$

We may shift the NLS into the frame of the envelope by scaling out the group velocity through the transformation

$$z' = z + v_g t. \tag{3.8}$$

Then by the chain-rule we have

$$\begin{aligned} \frac{\partial u}{\partial t} &= \frac{\partial u}{\partial z'} \frac{\partial z'}{\partial t} + \frac{\partial u}{\partial t} = \frac{\partial u}{\partial t} - v_g \frac{\partial u}{\partial z'} \\ \frac{\partial u}{\partial z} &= \frac{\partial u}{\partial z'} \frac{\partial z'}{\partial z} = \frac{\partial u}{\partial z'}. \end{aligned} \tag{3.9}$$

Plugging Equation 3.9 into Equation 3.7 we arrive at

$$-i\frac{\partial u}{\partial t} = \frac{1}{2}D\frac{\partial^2 u}{\partial z^2} - N|u|^2 u, \tag{3.10}$$

which is the NLS of the usual form and we have set $z' = z$ for clarity. One may further reduce the NLS to a canonical form by using the scaled variables $t = \frac{-tN}{2}$ and $z = z\sqrt{\frac{-N}{D}}$. We note we the roles of $\Delta\omega$ and Δk could have easily been reversed in our taylor expansion of generalized dispersion in Equation 3.4. The result is an NLS-like equation with the roles of time and space reversed and redefined coefficients

$$\begin{aligned} \frac{\partial k}{\partial \omega} &= v'_g \\ \frac{\partial^2 k}{\partial \omega^2} &= D' \\ \frac{\partial k}{\partial |u|^2} &= N'. \end{aligned} \tag{3.11}$$

This newly defined equivalent to group velocity may likewise be scaled out, resulting in a form of the NLS which is commonly used to study envelopes in optical fibers,

$$-i\frac{\partial u}{\partial z} = \frac{1}{2}D'\frac{\partial^2 u}{\partial t^2} - N'|u|^2 u. \tag{3.12}$$

This methodology is known as the slowly varying envelope approximation and is commonly to derive wave equations to first order. The NLS for spin wave envelopes in magnetic materials may be derived rigorously from a Hamiltonian formalism [3]. It can also be derived directly from Maxwell's equations and a magnetic torque equation using appropriate boundary conditions and multi-scale methods [47].

3.2 Cubic-Quintic Complex Ginzburg-Landau Equation

The primary focus of this thesis is the development and application of a driven-damped NLS better suited to describe the rich nonlinear dynamics being observed spin waves in thin magnetic films. We are principally motivated by a series of experiments conducted at CSU in which a series of chaotic solitons are observed. The traditional NLS, derived early in this chapter and given by Equation 3.10, is fundamentally unable to reproduce the observed

phenomena as integral equations do not exhibit chaotic behaviors. These phenomena were produced by driving stable soliton systems out of equilibrium, into regimes where dynamics are influenced, potentially subtly, by losses and gains present in the system. In this section we detail the development of a generalized high-order NLS which is known as cubic-quintic complex Ginzburg-Landau equation, the simplest model capable of reproducing the complex dynamics observed by CSU. The development of this model remains principally interested in the low and intermediate ring gain cases where a stable, underlying bright soliton trains are observed to modulate chaotically.

A thorough analysis of timeseries from CSU and of their experimental apparatus motivates several significant limitations on a potential model [26, 31, 43]. The active feedback ring, as introduced earlier in Section 2, applies an instant, periodic, linear gain on signals passing through the active feedback loop. These signals also experience instant losses at both the injection and detection transducers and continuous losses while propagating through the film. Spin wave frequencies typical of CSU experiments typically have round trip times of $\mathcal{O}(100 \ ns)$. This experimental design suggests two distinct modeling methodologies: (1) Ignore the electronic feedback loop and amplifier and only model evolution within the magnetic thin film. Periodic boundary conditions will mimic propagation around the ring. (2) Explicitly model the electronic feedback loop. We refer to these as the continuum and iterative models, respectively.

The continuum model is a gross simplification of feedback ring evolution, but may be justified as a valid approximation if the period of envelope dynamics is much greater than a single round trip time. In this limit the effect of the instant amplifier gain is compensated by linear loss within the film and dynamics are driven, over many round trips, by other forces acting in the system including dispersion, nonlinearity and nonlinear losses. Low and intermediate ring gain CSU time series satisfy this condition, with dynamics occurring on the order of 100 round trips. In the high ring gain cases observed dynamics approach periods on the order of 10 round trips and we may anticipate that this approximation will be insufficient

to describe spin wave behavior. Further, losses and gains expressed in a continuum model will represent the average values experienced by ring signals over many round trips and will not be directly proportional to measurable material values. Such a model is considered in Chapter 5

An iterative model provides a more thorough description of the experiment but with a more undefined potential scope. One may choose to model evolution in a film with an additional periodic amplification present, introducing a single additional free parameter to the continuum model. Alternatively one may more explicitly model each stage of ring propagation from transducer effects to coaxial cable transmission loss. The most appealing feature of an iterative model is that it eliminates ambiguity over the relative scales of modulation and round trip time and allows for the direct comparison of model and experimental parameters. The development, implementation and investigation of an iterative model to evaluate dynamics on the scale of single round trips is given in Chapter 7.

3.2.1 Phenomenological Gain and Loss

Experimental studies of nonlinear losses in the propagation of backward volume spin waves in magnetic thin films propagating under the influences of both three and wave mixing have been conducted [5, 28]. In both cases it has been demonstrated that there is a strong saturation in the observed power at the detection transducer relative to the power fed into the excitation transducer. Fittings to these profiles suggest both cubic and quintic losses can be relevant at higher ring power. Similar studies have been conducted for mode locked lasers where saturable gains are used to often used to study dynamics. One possible form of saturable gain is given by

$$\frac{iS_g}{1 + \frac{|u|^2}{I_s}},$$ (3.13)

where S_g is a saturable gain coefficient, I_s is a weighting factor and $|u|^2$ is the magnitude of the unitless magnetiation amplitude defined in Equation 2.24. Saturable gains of this form have been studied extensively by in the context of highly dispersive mode locked lasers [48, 49].

Early numerical studies of saturable gain suggested that it was ill suited for producing stable, modulated soliton trains of the type observed by CSU. Saturable gain may be generalized through a Taylor expansion

$$\frac{iS_g}{1 + \frac{|u|^2}{I_s}} = \approx iS_g - iS_g\frac{|u|^2}{I_s} + iS_g\frac{|u|^4}{I_s^2} + O\left(\frac{|u|^6}{I_s^3}\right). \tag{3.14}$$

We keep up to fifth order gain to match previous experimental fits to the power saturation cuves, and include a matching fifth order nonlinearity. Such a quintic nonlinearity may be obtained by keeping an additional term of the slowly varying envelope approximation used to derive the NLS in Section 3.1. Last we assign unique coefficients to each new term and arrive at the result is the cubic-quintic complex Ginzburg-Landau equation

$$i\frac{\partial u}{\partial t} = \left[-\frac{D}{2}\frac{\partial^2 u}{\partial z^2} + iL + (N + iC)|u|^2 + (S + iQ)|u|^4\right]u, \tag{3.15}$$

where N and D are defined in Equation 3.5, S is a quintic nonlinearity given by

$$S = \frac{\partial^2 \omega}{\partial|u|^4}, \tag{3.16}$$

and L, C and Q are linear, cubic and quintic loss or gain terms, respectively and depending on sign. All coefficients are real, with any imaginary parts explicitly stated in the equation. The CQCGL is fully generalized, but in a limiting case of approximating saturable gain one has $Q = C^2/L$ and we necessarily impose $|u|^2 I_s \ll 1$ for the expansion to be valid.

CHAPTER 4

ANALYTICAL AND NUMERICAL METHODS

4.1 Numerical Methods

The numerical methods used here simulate the propagation of spin wave envelopes within active magnetic thin film-based feedback rings were intentionally easy to approach and implement. As described in in Section 1 it is the intention of this work to demonstrate that the cubic-quintic complex Ginzburg-Landau equation, derived in Section 3 and given in Equation 3.15, is predictive and descriptive across a wide range of physics systems. It was therefore necessary to make any numerical simulation of the model approachable with the hope that anyone could simply reproduce our work if they desired and expand on its accuracy or scope if needed. To that end we numerically simulated the CQCGLE using a standard Split-step method where time propagation is computed via an Adaptive Runge-Kutta and the complex potential including the spatial dispersion derivatives are computing with a Pseudo-spectral method. Both methods may be easily derived and implemented, and a majority of necessary code is also available in common resources such as *Numerical Recipes* [50]. The authors understanding of this topic was also heavily influenced by the PhD thesis of Victor Snyder [51].

The remainder of this chapter will be spent introducing these methods and discussing their numerical robustness in the context of simulating complex, driven damped systems.

4.1.1 Adaptive Runge-Kutta

Runge-Kutta are a family of high order finite differencing algorithms which are commonly used and well studied. We consider the case of Cash and Karp's fifth-order adaptive timestep Runge-Kutta method with an embedded fourth-order forumla. This implementation is included in *Numerical Recipes*. This method gives a fifth-order approximation to $u(t + \delta t)$ given $u(t)$, or in other words to the first-order ordinary differential equation

$$\frac{\mathrm{d}u}{\mathrm{d}t} = f(t, u),$$

over timestep δ_t. This approximations is given by

$$u(t + \delta_t) = u(t) + \frac{37}{378}K_1 + \frac{250}{621}K_3 + \frac{125}{594}K_4 + \frac{512}{1771}K_6 + \mathcal{O}(\delta_t^6), \qquad (4.1)$$

where the coefficients are

$$
\begin{aligned}
K_1/\delta_t =& u\left[t, u(t)\right], \\
K_2/\delta_t =& u\left[t + \frac{1}{5}\delta_t, u(t) + \frac{1}{5}K_1\right], \\
K_3/\delta_t =& u\left[t + \frac{3}{10}\delta_t, u(t) + \frac{3}{40}K_1 + \frac{9}{40}K_2\right], \\
K_4/\delta_t =& u\left[t + \frac{3}{5}\delta_t, u(t) + \frac{3}{10}K_1 + \frac{9}{10}K_2 + \frac{6}{5}K_3\right], \\
K_5/\delta_t =& u\left[t + \delta_t, u(t) - \frac{11}{54}K_1 + \frac{5}{2}K_2 - \frac{70}{27}K_3 + \frac{35}{27}K_4\right], \\
K_6/\delta_t =& u\left[t + \frac{7}{8}\delta_t, u(t) + \frac{1631}{55296}K_1 + \frac{175}{512}K_2 + \frac{575}{13824}K_3 + \frac{44275}{110592}K_4 + \frac{253}{4096}K_5\right].
\end{aligned}
\qquad (4.2)
$$

Finally an estimate of the truncation error in the embedded fourth-order forumla is

$$
\begin{aligned}
\Delta \;=\; & \left(\frac{37}{378} - \frac{2825}{27648}\right)K_1 + \left(\frac{250}{621} - \frac{18575}{48384}\right)K_3 \\
+ \; & \left(\frac{125}{594} - \frac{13525}{55296}\right)K_4 - \frac{277}{14336}K_5 + \left(\frac{512}{1771} - \frac{1}{4}\right)K_6,
\end{aligned}
\qquad (4.3)
$$

and provides a basis for adapting the step size. Following the *Numerical Recipes'* methodology, if on any given timestep the estimated truncation error is below some tolerance Δ_0 then the fifth-order approximation is accepted. In addition the timestep is adjusted so that

$$\delta_t^{\text{next}} = \frac{9}{10}\delta_t^{\text{now}}\left|\frac{\Delta}{\Delta_0}\right|^{1/5}. \qquad (4.4)$$

If the estimated error is instead higher than the tolerance the timestep size is reduced to

$$\delta_t^{\text{next}} = \frac{9}{10}\delta_t^{\text{now}}\left|\frac{\Delta_0}{\Delta}\right|^{1/4}, \qquad (4.5)$$

and the current timestep is attempted again under the same criteria. This is repeated until either the timestep succeeds or a predetermined number of attempts is reached and the simulation is aborted.

4.1.2 Psuedo-Spectral Methods

Pseudo-spectral methods exploit the fact that the derivatives of a function may be computed by simple multiplication on its fourier transform. Given a function $u(x)$ and its fourier transform $F[u(x)]$ the nth derivative of the function is given by $F^{-1}[(2\pi i x)^n F[u(x)]]$. This method can offer increased accuracy and decreased computation time for smooth functions through the use of Fast Fourier Transform algorithms, such as those provided in *Numerical Recipes*. We may expect the derivatives computed using this method to be well behaved, and exact the grid points. Discontinuities in the original function $u(x)$ on the scale of the lattice spacing will, however, introduce artifacts such as ringing into the transform which will result in significant errors being introduced during the inverse transformation. These errors generally are severe enough, however, to trigger failure in any reasonably tuned adaptive Runge-Kutta algorithm during any subsequent propagation.

The case for discrete fourier transforms is slightly more convoluted but may still be easily derived. For a discrete set of data $f(x_n)$ for $n = 1, 2, 3, ..., N$ and spacing δ_x the discrete fourier transformation and its inverse are defined as,

$$X_k = \sum_{n=0}^{N-1} x_n e^{\frac{-2\pi i}{N} kn}, \tag{4.6}$$

and

$$x_n = \frac{1}{N} \sum_{k=0}^{N-1} X_k e^{\frac{2\pi i}{N} kn}. \tag{4.7}$$

In the discrete case derivatives must be approximated by finite differencing. The form of the derivatives may be isolated from a standard central differences. For the first derivative we have

$$\frac{\Delta f(x_j)}{\Delta_x} = \frac{f(x_j + 1) - f(x_j - 1)}{\delta_x} = \frac{1}{\delta_x N} \sum_{k=1}^{N-1} \left[X_k e^{\frac{2\pi ikj}{N}} \left(e^{\frac{2\pi ik}{N}} - e^{\frac{-2\pi ik}{N}} \right) \right],$$

$$= \frac{2}{\delta_x N} \sum_{k=1}^{N-1} \left[X_k e^{\frac{2\pi ikj}{N}} \sin(\frac{2\pi k}{N}) \right]. \tag{4.8}$$

Which is the discrete fourier transform of x_n scaled by $\sin(\frac{2\pi k}{N})$. The second-order central difference may be similarly used to find an expression for the second derivative. This yields,

$$\frac{\Delta^2 f(x_j)}{\Delta_x^2} = \frac{2}{\delta_x^2 N} \sum_{k=1}^{N-1} \left[X_k e^{\frac{2\pi ikj}{N}} \left(\cos(\frac{2\pi k}{N}) - 1 \right) \right], \tag{4.9}$$

Similar to the first derivative the second is given by a multiplication on the discrete fourier transform, this time of the form $\left(\cos(\frac{2\pi k}{N}) - 1 \right)$.

4.1.3   Implimentation

The implementation of the of the above psuedo-spectal spatial derivatives and adaptive Runge-Kutta temporal propagation for the simulation of the CQCGLE via a split-step method is rather trivial. One needs initial and boundary conditions to utilize the existing algorithms in *Numerical Recipes*. For any given timestep we compute the local, instantaneous effects of the gains, losses and nonlinearity in x-space before computing the instantaneous dispersion in k-space via Equation 4.9. This is then propagated forward in time via the adaptive Runge-Kutta. Note that the set of N constants needed for computing the second derivative via Psueod-spectral methods is constant and independent of x_n so only needs to be computed once for each grid size.

We may easily recast the CQCGL given in Equation 3.15 into a first-order differential equation of the form given Equation 4.1.1 needed to make use of the Runge-Kutta algorithm. If $u_{ab} = u(z_a, t_b)$ corresponds to the scaled magnetization amplitude at some grid point a and time step b then we may write

$$\frac{\partial u_{ab}}{\partial t} = -i \left[-\frac{D}{2} \frac{\partial^2 u_{ab}}{\partial z^2} + iL + (N + iC)|u_{ab}|^2 + (S + iQ)|u_{jk}|^4 \right] u_{ab} \tag{4.10}$$

where we have divided by i. Numerically this will result in the swapping of real and imaginary parts during this evaluation. Dropping this transformation is a common mistake. If we define $\mathcal{F}$ and $\mathcal{F}^{-1}$ to be the discrete fourier transform as and its inverse as discussed above we can replace with the spatial derivative with our psuedo-spectral approximation giving

$$
\begin{aligned}
\frac{\partial u_{ab}}{\partial t} \approx -i\bigg(&-\frac{D}{2}\mathcal{F}^{-}1\left[\mathcal{F}(u_{ab})\left(\cos(\frac{2\pi k}{N})-1\right)\right] \\
&+iL+(N+iC)|u_{ab}|^2+(S+iQ)|u_{ab}|^4\bigg)u_{ab}.
\end{aligned}
\tag{4.11}
$$

This may then be evaluated using the adaptive Runge-Kutta method. This analysis can also be extended to higher dimensions. We also highlight the inclusion of additional derivative terms or gain loss terms will not increase the computational complexity of the above step. However gain and loss do generally require finer time discretization.

A stable initial condition can easily be generated via imaginary time propagation where $t \to -i\tau$ in the CQCGLE with $S, L, C, Q =$. This transforms the general solution of the time-dependent nonlinear Schrödinger equation given by a sum of weighted energy eigenfunctions into a sum of decaying exponentials. If we propagate forward in τ then higher energy modes will experience exponentially more decay than the ground state. The exponential decay can be combined with a periodic renormalization and then evolved forward in τ until only the lowest loss eigenmode will remain. This result can be used to converge any random initial condition to the ground state to machine precision. Imaginary time decay is used to create all initial conditions used in this work, including those used to verify convergence.

Numerical convergence is typically demonstrated by comparing a result to known, analytic solutions as temporal and spatial resolutions are increased. In the case of the CQCGLE where no there exist no or few known solutions we may not try to demonstrate a steady state solution in converged this same way. Complex dynamical solutions require careful care, particularly in the case of chaotic evolution where no two numerical simulations may be directly compared due to the exponential separation of nearby trajectories in phase space. It is also

not possible to show convergence in norm in the presence of gains and losses and nonlinearity prevents backwards time propagation. A more rigorous discussion of these issues as well as some examples are provided in Section 5.8.

4.2   Nonlinear Time Series Analysis

One often finds themselves presented with a set $\{x_1, x_2, \ldots, x_n\}$ of some observable quantity, x, having been measured at discrete values of a time-like variable t. Regardless of the nature of the generating system: numeric, experimental, deterministic, stochastic, finite or continuous, the fundamental goal is usually to quantitatively determine as much *information* as possible about the origins of the observed signal. Ideally one seeks to determine the observable's evolution rule, $D[x_m] = x_{m+1}, m < n$, and use that to study the physical and dynamical properties of the underlying generating system. In general one will have access to at worst a single observable quantity and at best an a priori knowledge of the generating system and its physical mechanisms. Even with significant a priori knowledge it is exceedingly rare to have access to a full phase space when conducting experiment or numerics. Thus the task of nonlinear time series analysis is ultimately the *characterization of an unknown phase space*.

For the purposes of this work it is assumed that a generating system (physical or numeric) in the form of a differential equation or discrete-time evolution rule is responsible for the observations. Any stochastic behavior will therefore be attributed to independent and identically distributed (IID) random noise isolated in system parameters or measurement processes. The general case of continuous-time dynamics may be written down as the partial differential equation (PDE) describing a field $\boldsymbol{\phi}(\mathbf{x}, t) = [\phi_1(\mathbf{x}, t), \phi_2(\mathbf{x}, t), \ldots, \phi_n(\mathbf{x}, t)]$ of n components,

$$\frac{\partial \boldsymbol{\phi}(\mathbf{x}, t)}{\partial t} = \mathbf{G}(\boldsymbol{\phi}(\mathbf{x}, t)), \tag{4.12}$$

where the vector field $\mathbf{G}$ is assumed to be well behaved, which in the context of this work signifies continuous, bounded and differentiable.

A measurement process, s, which maps $\phi(\mathbf{x}, t)$ to the real numbers is assumed to sampled every t_s to generate our time series,

$$s(\mathbf{x}, n) = s(\phi(\mathbf{x}, t_0 + nt_s)) + \eta_n, \tag{4.13}$$

where s is an unknown, and in general nonlinear, function of the underlying variables of the system, t_0 is the initial measurement time, η_n is the IID random noise associated with the measurement process and $n \in \{0, 1, 2, ..\}$. We will assume measurements occur at a fixed space coordinate and adopt the notation $s(n) = s(\mathbf{x}, n)$ for the remainder of this work. Likewise η_n is assumed to be insignificant unless specifically stated to be otherwise.

The remainder of this section will deal with the classification of data of the above form when the dynamical system responsible is nonlinear and exhibits chaos.

4.2.1 Chaos
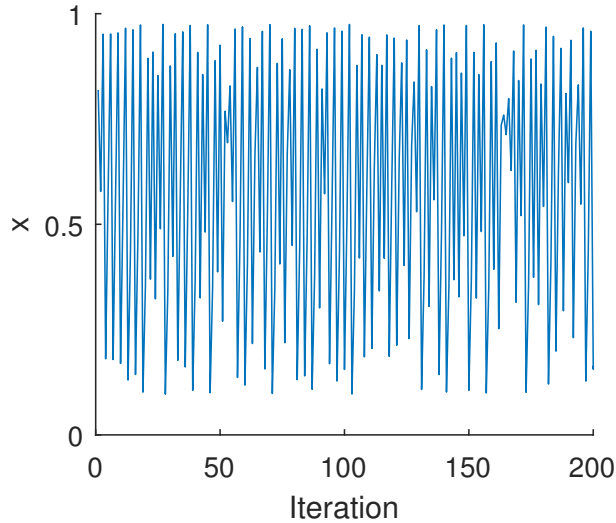
Figure 4.1: Timeseries of the Logistic map in a chaotic regime. 200 iterations of the Logistic map $x_{n+1} = rx_n(1 - x_n)$ with $r = 3.9$ and $x_0 = 0.5$. This is a chaotic regime of the one dimensional map.

Chaos is used to describe a dynamical system whose bounded evolution appears to be random. A typical numerical example, the logistic map is shown in Figure 4.1. The source of this apparently random behavior is the result of two defining features of chaotic data: (1) that

it is aperiodic (has broadband spectrum) and (2) trajectories show exponential sensitivity to initial conditions. The first steps towards a fundamental understanding of chaos were made by Henri Poincaré in his two-dimensional portrait of the three-body problem at the turn of the 19th century [52]. Chaos was not accepted as the third type of non-transient motion until half a century later when computing resources became powerful enough to allow Edward Lorenz to numerically evaluate his now famous differential equations and he noticed divergence when restarting simulations [53]. Lorenz' work would not have been possible without the significant contributions of Ellen Fetter and Margaret Hamilton who programmed, implemented and ran the numerical computations behind the now famous results [54]. By the early 1980s the theory and methods of nonlinear and chaotic time system analysis had established some footing with the works of Grassberger and Eckman and the term *Chaos* had been coined by Yorke [55–59]. Since its acceptance chaos has been observed experimentally in laser cavities, microwave magnetics, fluid dynamics, electronic circuits, wildlife populations, neural signals, and atmospheric data (to name a scant few).

The inherent instability and broadband nature of chaotic data have significant consequences on our standard approaches to time series analysis. Most importantly, no individual trajectory may be direcrtly compared to another experimental or computed orbit where now any numerical roundoff or inherent limit on experimental precision will render each trajectory unique. This implies there will be no explicit way to compare separately generated time series without the use of statistical quantities. Additionally the broadband spectra of additive noise is no longer distinguishable from the underlying chaotic dynamics via Fourier transforms, see Figure 4.2. In fact, the task of data separation in nonlinear systems is entirely nontrivial [60, 61].

The origins of chaos in nonlinearity imply we need to separate ourselves from the use of the ubiquitous and powerful linear time series technique of power spectra. While a linear system may be uniquely characterized by the sharp line spectra of its power spectrum (invariant measures of the series under perturbations of the initial conditions), we may **not** rely on the
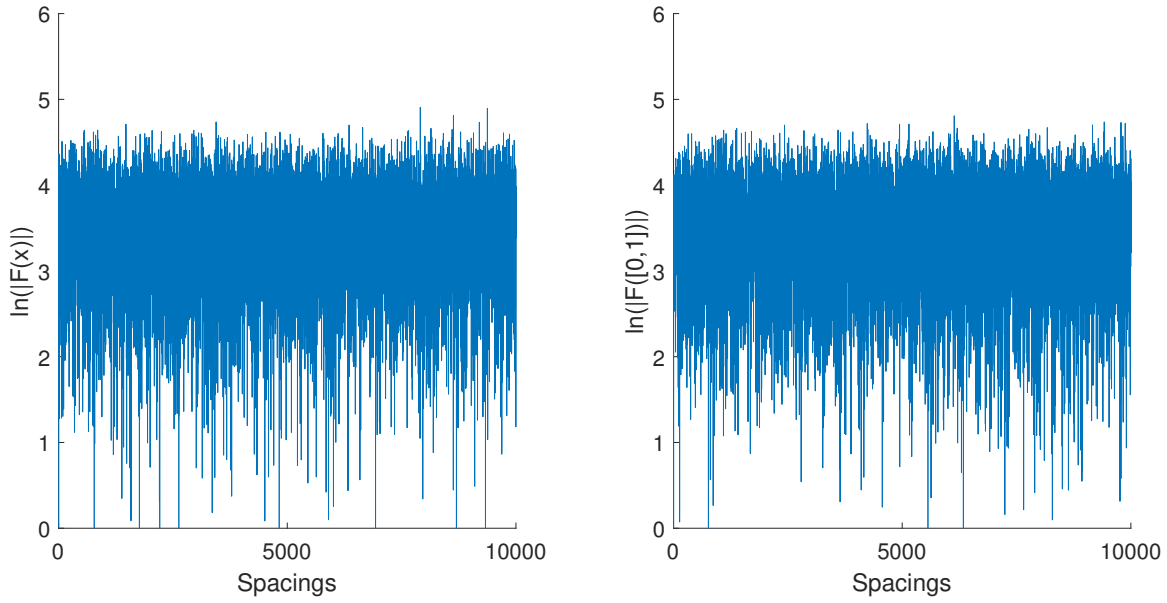
Figure 4.2: Fourier spectra of random noise and chaotic logistic map data. (left) Power spectrum of 20000 iterations of the Logistic map defined in. (right) Power spectrum of 20000 pseudo-random numbers from the normal distribution. Both spectrum generated by fast Fourier Transform.

power spectrum of chaotic signals as a means of identification across multiple trajectories.

The limited utility of the Fourier transform on nonlinear signals is easily understood from the perspective of the underlying dynamical system: A linear system of differential equations will be transformed into an algebraic problem in Fourier space; a marked reduction in complexity. The transformation of a nonlinear system of differential equations is instead into a series of convoluted integral equations in Fourier space. This is not in general an improvement [62]. Linear signals will also be invariant under translations in time, so sines and cosines present a natural basis. The same may not be said for nonlinear signals.

4.2.2 Phase Space and Attractor Reconstruction

The limitations of the tools of linear time series analysis are now well understood, however our ultimate goals for the analysis of chaotic signals remain the same. A new set of invariants for chaotic systems are necessary to characterize the dynamics in place of sharp lines in power spectra.

37

We earlier assumed that a deterministic dynamical system, $\mathbf{G}$, in the form of a differential equation or discrete-time evolution rule is responsible for the series $s(n)$. Once the state of $\mathbf{G}$ is defined for a time t_0 the state at all future times are fixed. Once an initial state is known we can study the dynamics of the system by studying the dynamics of the phase space points [60–62]. This state is specified by a vector in the phase space of the system. The dimensionality of this phase space represents the minimum number of variables necessary to uniquely define a state of the system. For the case of m coupled ODEs the dimensionality of this space is exactly m. This is easily seen for the case of a particle under constant potential in 3 dimensional Cartesian space. One must supply the 3-dimensional position and 3-dimensional velocity in order to guarantee a unique solution to 6-dimensional ODE generated by Newton's second law of motion. The omission of a single variable leaves us instead with an infinite family of solutions which makes describing dynamics unmanageable. For a PDE this phase space dimension is infinite.

Signals observed from physical systems are described by dissipative PDEs of the form defined by Equation 4.12. These signals are finitely sampled in space and in time. If the signal represents a well behaved observable, i.e. something experimentalists are likely to design experiments to observe, then the behavior is bounded within the measurement limits of the experimental apparatus. The experimentalist will of course strive to ensure their measurement limits are far beyond the dynamic limits of their observables, but one can be sure this limit is still far below infinity. Discrete sampling means we may treat a PDE as a large number, N, of couple ODEs for the purposes of discussing the time series $s(n)$. In the limit where $s(n)$ is no longer approximate, $t_s \to 0$ and $N \to \infty$, one recreates the original PDE for any space point x.

In reality the dimensionality, m, of our phase space is infinite and at best the approximation $N \gg 1$ is still too large to be tractable for analysis. We will instead exploit that the time series we're presented with is physical and the evolution is bounded in $s(n)$. This implies our dynamical system is evolving in some bounded region of the full phase space

known as the *attractor* of the system. Importantly, the attractor is invariant under dynamical evolution and reasonable perturbations (perturbations which do not push the solution outside the attractor itself, or which are on average smaller than the radius of the attractor) [55, 60, 61, 63]. The dynamical system **G** does not in general preserve the volume of the associated phase space, in fact within dissipative systems the phase space volume containing some initial conditions will contracted under the dynamics. Regardless, trajectories which evolve onto the attractor will in general remain there indefinitely, unless perturbed outside the set of initial conditions which evolve into the attractor.

It may then be expected that if one observes a *stationary* time series from a dynamical system that these dynamics are being carried out on an attractor of finite dimension $d_a \ll n$. There are four types of attractors which can exist in phase space corresponding to geometrical subspaces: fixed point (point), limit cycle (line), limit torus (surface) and strange (fractal). A dynamic which equally fills all directions in phase space (volume) is noise.

We remind the reader that an interesting consequence of determinism for autonomous ODEs is that trajectories in phase space must not cross. This implies that complex attractor behavior must occur in an attractor of dimension $d_a > 2$ where folding and mixing are possible. The mutually exclusive concepts of a finite attractor and exponential time divergence of initial conditions can only occur if the nonlinearity of the system allows the kind of folding described above. This allows for infinite trajectories in a finite area [60]. Of course, map-like systems can exhibit chaos on attractors with dimensions less than two.

Our task of extracting details of the dynamical system may be accomplished by reconstructing the attractor describing the observed evolution using the information available to us, $s(n)$. The process of converting a time series into state vectors is formally known as *time delay embedding* or *phase space reconstruction*. Since $s(n)$ is generally unknown and nonlinear it is unlikely one will be able to reconstruct the original phase space of the dynamical system. We argued above that knowledge of the total phase space is unnecessary if the motion we are interested in exists on an small (in comparison to the original phase

space) dimensional attractor. We instead seek to recreate the simplest space in which the embedded attractor is equivalent to the attractor in the full space. Formally one states attractors in the two spaces are equivalent if the embedding procedure is a one-to-one map and an immersion [58, 60]. The goal of embedding is to introduce the attractor into a space where the dynamics are completely unfolded.

Assuming an attractor of dimension D there are two tasks necessary to complete the embedding. First, To uniquely describe the dynamics of the system we much construct D independent variables from $s(n)$ for every time nt_s that is sampled. Equivalently we need to specify the D-dimensional state vector for every time $s(n)$ is sampled. Second we need to embed the attractor into a Cartesian vector space so we have a global representation of the dynamics where we can perform analysis [58, 60, 62].

The second problem was addressed in Whitney's embedding theorem in 1936 and later strengthened in 1991 by Sauer. They showned that for any attractor with a finite dimension, d_a, then almost every one-to-one immersion from the attractor to $\Re^m$ with $m > 2d_a$ forms an embedding [58, 60, 64, 65]. Note, the attractor dimension is not required to be integer valued [65].

The first problem was addressed by in Taken's delay embedding theorem in 1981, and was again strengthened in 1991 by Sauer. It is shown that for almost every smooth measurement function s and sampling time $t_s > 0$ the delay time embedding into $\Re^m$ with $m > 2d_a$ is an embedding if there are no periodic orbits of the system with period t_s or $2t_s$ and only a finite number of periodic orbits with period $pt_s, p > 2$ [65, 66]. The delay time embedding vectors are defined as,

$$\mathbf{s}(n) = [s(n - (m-1)\tau), s(n - (m-2)\tau), \dots, s(n - 2\tau), s(n - \tau), s(n)], \qquad (4.14)$$

where τ is the delay time and m is the embedding dimension defined above. The visual comparison of the original attractor of the 3-dimensional Lorenz equations (x(t),y(t),z(t)) and a reconstruction generated only the time series x(t) is shown in Figure 4.3. The variables

τ and m used in an embedding are known as the *embedding parameters*, and in general it is the goal of nonlinear time series analysis to determine these values. It is often argued that the relevant embedding parameter is $m\tau$, known as the delay window, since this represents the time spanned by an embedding vector[60, 67]. There are a great number of alternative methods to delay time embedding as well as generalizations which allow for variable τ which are beyond the scope of this work [68, 69].
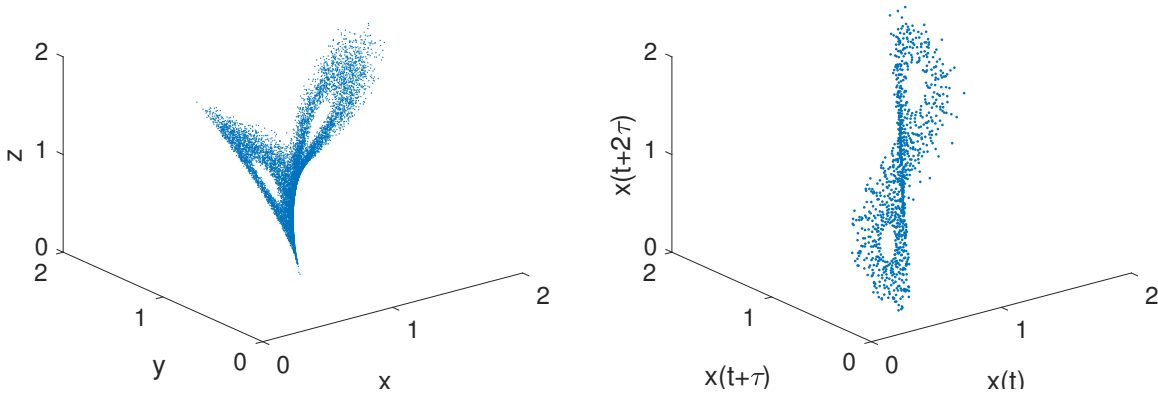
Figure 4.3: Full phase space and a reconstruction of the Lorenz attractor. (left) The phase space portrait of the Lorenz equation for 5000 iterations. (right) A reconstructed phase space from the same 5000 iterations of x(t). [53]

The Takens embedding procedure produces $N = n-(m-1)\tau$ points in the m-dimensional reconstructed phase space from a time series of finite length n. The embedding theorems assume $s(n)$ is a noise free time series of infinite length and provide no insight into the proper choice of m or τ for a physical, noisy, time series of finite length. One is generally trying to determine the dimension of the attractor, d_a, with no bounds on the proper choice of m. The embedding theorems provide a formal mathematical foundation for the analysis of nonlinear time series but provide little practical information beyond a proof of concept. One must return to the theory of dynamical systems and the geometry of attractors to attempt and choose the appropriate embedding parameters.

4.2.3 Embedding Parameters

For the case of noisy and finite time series the choice of embedding parameters is nontrivial. There exist systematic methods for determining approximations for these parameters from the time series itself. Sauer demonstrated that for any choice of dimension $m > 2 * d_a$ we expect a valid embedding space, so the choice of large embedding dimensions will in theory, assuming sufficient data, only have negative impact on the computing time involved in analysis [65]. The general approach to optimizing the embedding parameters is then using statistical tools to determine an approximation for the delay time or delay window and evaluating an invariant of the attractor as the dimensionality is increased. A plateau in the behavior of the invariant as a function of m is sought as evidence of satisfying the embedding theorem conditions. Useful invariants will be introduced below.

Methods for approximating the embedding parameters are a subject of much ongoing research and numerous approaches are suggested every year [67–83]. The author here follows the philosophy of Kantz in regards to the selection of an appropriate time delay. The dozens of methods available for the determination of the time delay attempt to exploit the same feature of state space: that a state vector is fundamentally comprised of independent variables. The best choice of τ is generically one which maximizes the independence, in some linear or nonlinear sense, of the delay separated components of our time series, $s(n)$. The methods differ in the ways they characterize this independence but ultimately produce τs on the same order of magnitude [69, 70, 75, 78, 82]. Kantz argues that results should not depend too sensitively on τ since this suggests the properties of the reconstructed attractor are not invariant under smooth transformations [60]. A violation of this invariance suggests one is not analyzing a signal generated on an attractor. Thus the use of a preferred method is suggested to generate a working estimate. If desired the performance of invariants can be optimized in practice by variation of τ [60].

The simplest tool for quantifying the independence of the delayed time series is the linear autocorrelation function where the value at lag τ is given by

$$C(\tau) = \frac{<s(n)s(n-\tau)> - <s>^2}{\sigma^2},$$

$$<s> \approx \frac{1}{N}\sum_{n=1}^{N} s(n),$$

$$\sigma^2 \approx \frac{1}{N-1}\left(\sum_{n=1}^{N} s(n)^2 - N<s>^2\right),$$

(4.15)

where the time series has been used to estimate the mean, $<s>$, and variance, σ^2. To within some factors of N the autocorrelation function may be seen as a ratio of variances,

$$C(\tau) \approx \frac{<s(n)s(n-\tau)> - <s(n)>^2}{<s(n)s(n)> - <s(n)>^2}.$$

The autocorrelation function is then the weighted *variance* of the delayed series with respect to the original normalized by the variance of the original. This ratio quantifies how points are distributed in the $\{s(n), s(n-\tau)\}$ series. $C(\tau) = 0$ suggests the points are distributed evenly over the plane, $C(\tau)! = 0$ suggests they crowd towards the appropriate diagonal. A good choice of τ may be argued to be the first zero crossing of $C(\tau)$ [60, 61, 84].

The autocorrelation function estimates the linear correlation between two time delayed state vectors, neglecting any nonlinear correlations present in the data. A more general characterization of the correlation is given by the average mutual information. The amount of information two measurements share is defined as the mutual information. This is a measure of how much knowing the first measurement influences our knowledge of the second. The mutual information is defined as

$$I_{AB}(a_i, b_j) = \log_2\left(\frac{P_{AB}(a_i, b_j)}{P_A(a_i)P_B(b_j)}\right),$$

(4.16)

where A and B are discrete random variables, a_i and b_j correspond to specific values. The probability and joint probabilities are defined in the usual way. Then the average mutual information is the mean of the mutual information across all choices of a_i and b_j. In the

context of our time series the probability distributions will have to be generated by binning and $A = s(n), B = s(n - \tau)$. We can then define the average mutual information as

$$I(\tau) = \sum_n P(s(n), s(n - \tau)) \log_2 \left[\frac{P(s(n), s(n - \tau))}{P(s(n))P(s(n - \tau))} \right]. \quad (4.17)$$

The average mutual information is positive definite and will approach zero when $P(s(n), s(n - \tau)) \to P(s(n))P(s(n - \tau))$, or when the two measurements are statistically independent. As τ increases the two signals will have less and less to do with each other, so it is expected $I(\tau)$ will be inversely proportional to the time delay. The first zero of the average mutual information is a good choice for τ [60, 61, 84, 85].

With several meaningful ways to determine τ we now want to focus on the remaining embedding parameters: the delay window and embedding dimension. The most common method for evaluating the embedding dimension is the false nearest-neighbor statistic, which is not utilized in this work [60]. We choose instead to focus on the delay window, from which an embedding dimension may be indirectly determined by the relation $\tau_w = m\tau_d$ where we've adopted the subscripts w and d to indicate window and delay, respectively. We focus on one popular methodology, the C-C method [67]. There have been recent attempts to improve upon this algorithm in the so called C-C-3 method, but this is not investigated in this work [83]. The C-C method relies on the so called BDS statistic [86]. The BDS measures the significance of calculations of correlation dimensions from the correlation integral as a dimensionless measure of nonlinear dependence [67, 83, 86]. The correlation integral will be discussed in depth in the following section. The C-C method evaluates the the BDS statistic for a variety of embedding dimension and length scales, and records the mean and variance as a function of τ. The minimum of the absolute sum of these quantities is argued to represent the optimal time of the dynamical system responsible for the time series analyzed, or in our language the delay window.

4.2.4 Phase Space Invariants

Now that we have reconstructed the attractor underlying the dynamics of our time series we want to classify the system. This is done through the identification of and quantification of invariants. We start by acknowledging the invariants are functions of the dynamical systems' attractor and are therefore dependent in some sense on our choice of of embedding parameters. Regardless of the appropriateness of these parameters one may easily apply the measures described here and arrive at numerical estimates of any number of invariants under the most erroneous of circumstances. Even infinite-dimensional noise can easily be construed as finite-dimensional dynamics under simple miss steps of analysis. That is to say that the methods of nonlinear time series analysis are not robust and are in fact prone to misinterpretation and superfluous characterization. The issue of naive application is so prevalent in the literature that many authors caution against any published numerical result not accompanied by am explicit discussion of the reconstructed phase space and the plateau measurements [60]. The previous sections were thorough regarding the motivations and underlying assumptions of this analysis so that we may now be perfectly explicit about the appropriate use of the following methods.

The two common invariants studied in the literature are dimension and the Lyapunov exponent, which describe the geometry and dynamics of the attractor, respectively. In this work we focus on estimations of dimension, which while subject to miss steps of analysis, are robust measures. Estimates of Lyapunov exponents, λ_k, which measure how quickly nearby trajectories in phase space separate are inherently unstable. First, for a D dimensional system there exist D distinct Lyapunov exponents. If the observed dynamics occur on an attractor of dimensionality, m, then there exist $D-m$ so-called spurious Lyapunov exponents which do not describe the dynamics on the attractor. The general solution to this issue is assuming the largest Lyapunov exponent describes dynamics on the attractor and seeking only to estimate that. However, algorithms which estimate the largest Lyapunov exponent are explicitly sensitive to choices to in embedding parameters and are also highly sensitive

to noise and the size of the recorded data series. The estimation in separation of nearby trajectories **requires** the isolation of nearby trajectories in the reconstructed phase space, and also that the (super)norm of their separation is accurate. Features on the scale of a single trajectory are going to be harder to measure than those on the scale of the entire attractor. While careful estimation (with convergence as a function of m) of Lyapunov exponents is no doubt possible and sometimes useful, we do not consider it in this work.

We seek instead to estimate the dimensional of the reconstructed attractor. This is most commonly done by the use of a generalized correlation integral as defined

$$C_q(\epsilon) = \int_{\mathbf{x}} d\mu(\mathbf{x}) \left[\int_{\mathbf{y}} d\mu(\mathbf{y}) \Theta(\epsilon - \|\mathbf{x} - \mathbf{y}\|) \right]^{q-1}, \qquad (4.18)$$

where μ is some measure defined in a phase space, $\mathbf{x}$ and $\mathbf{y}$ are phase space points and Θ is the Heaviside step function [60, 61, 84].

$$\Theta(x) = \begin{cases} 0 & : x \leq 0 \\ 1 & : \text{else} \end{cases} \qquad (4.19)$$

For a self-similar set we have,

$$C_q(\epsilon) \propto \epsilon^{(q-1)D_q}, \qquad \epsilon \to 0, \qquad (4.20)$$

so that we define the generalized dimension, D_q as,

$$D_q = \lim_{\epsilon \to 0} \frac{1}{q-1} \frac{\ln C_q(\epsilon)}{\ln \epsilon}. \qquad (4.21)$$

For a sequence of space time points, $y(n)$, we estimate the correlation integral by the correlation sum, also known as the Grassberger and Procaccio algorithm [55–57],

$$C_q(\epsilon) = \lim_{N \to \infty} \frac{(N - 2n_{\min} - 1)^{1-q}}{N - 2n_{\min}} \sum_{i=n_{\min}}^{N-n_{\min}} \left[\sum_{|j-i| < n_{\min}}^{N} \Theta(\epsilon - \|\mathbf{y}(i) - \mathbf{y}(j)\|) \right]^{q-1}, \qquad (4.22)$$

where $\|X\|$ is a norm and $n_{\min}$ is the Thieler correction used to eliminate the spurious effect of temporal correlations from the time series by eliminating the $n_{\min}$ closest points. Since the delay time embedding procedure involves the reconstruction of state-space vectors from a single time series, $s(n)$, points close in time will be highly correlated. Estimates of the

correlation dimension will be significantly underestimated if temporal correlation is assumed to be geometrical structure on the attractor [60, 61, 84, 87]. We define $t_{\min} = n_{\min} t_s$ and exclude all pairs closer than $t_{\min}$ in the correlation sum. This results in the loss of a fraction $2 n_{\min}/N$ of all pairs. The preferred method for determining a reasonable value for $t_{\min}$ is the space time separation plot, but won't be discussed here [60]. In practice a reasonable choice for $n_{\min}$ is $\sqrt{N}$ unless there are significant concerns about the amount of data available. A choice on this order will also eliminate any spurious temporal correlations that result from oversampling.

One might notice that in the definition of Equation 4.21 there are two limits which will cause us problems with real data sets. The limit $N \to \infty$ is violated explicitly by any finite data set and $\epsilon \to 0$ will have a lower bound imposed by the numerical quality of the signal. In practice the violation of $N \to \infty$ is generally not an issue so long as there is enough data to clearly define the reconstructed attractor. Any limit on $\epsilon \to 0$ will impose a restriction on on our ability to estimate Equation 4.20 on small scales. For values of $q \neq 2$ we also have to take the bracketed sum to nontrivial powers, which results in biased estimations of $C_{q\neq 2}$.

There are three dimensions which are typically considered corresponding to $q = 0, 1, 2$ in equations 4.20 and 4.22. These are known as the box-counting dimension, information dimension and correlation dimensions, respectively. In practice the box-counting dimension (the number of boxes of size ϵ needed to cover all data) is unusable as an algorithm as it requires extremely high resolution data. The desirable information dimension (the average Shannon information needed to locate a point with accuracy ϵ) is computationally intractable. The correlation dimension is by far the easiest to compute and estimate for finite data sets. In general D_q is not strongly dependent on q and D_2 is a reasonable approximation of D_1. If there is a strong D_q dependence then the underlying data is called multi-fractal and D_2 is not a particularly useful measure for the system. For these reasons we focus entirely on the estimation of the correlation dimension through the correlation sum with $q = 2$.

4.2.5 Practical Implementation Of Dimension Estimation

In practice the task of estimating the correlation dimension is ultimately one of identifying scaling regions in the behavior of the correlation sum. Where for $q = 2$ from equations 4.20 and 4.21 we have

$$C_2(\epsilon) \propto \epsilon^{D_q}, \qquad \epsilon \to 0, \tag{4.23}$$

and

$$D_2 = \lim_{\epsilon \to 0} \frac{\ln C_2(\epsilon)}{\ln \epsilon}. \tag{4.24}$$

This is an inherently subjective process where one looks looks at a $\log(C_2)$ vs $\log(\epsilon$ plot and attempts to visually identify scaling regions, then measure their slope. One may also look at $\mathrm{d}\log(C_2)/\mathrm{d}\log(\epsilon)$ and identify scaling regions via the local slope. This subjective process is another reason demonstrating saturation in the dimension estimate over increasing embedding dimension is so important - it gives one means of establishing error bars on the estimate.

It is important to keep in mind that there will be, generally, four distinct regions in a $\log(C_2)$ vs $\log(\epsilon$ plot. (1) For ϵ on the scale of the attractor the correlation sum has no scaling behavior, as the sum is now a function of the attractor's large scale geometries which are ϵ and $m > 2d_a$ (so that the attractor is unfolded) independent. (2) At smaller values of ϵ the true scaling region, if present, will be identifiable. In practice it is at most 2-3 octaves wide. (3) As ϵ is decreased further a regime dominated by noise is identifiable. As noise is space filling this region as scaling approaching m. Note that noise is present for all length scales, but usually only dominates at small length scales. If overall noise levels approach 2% then it is often impossible to identify even one octave of true scaling. The present of noise at all levels also means that estimations for the dimension will have some m-dependence for all $m > 2d_a$ and generally *increase* as embedding dimension is increased. The use of a time-delay window rather than a time delay can accomodate for this by increasing the effective time-delay for embeddings in higher dimensions. The use of a sup or maximum

norm measure can also impact this scaling. (4) At the lowest length scales statistics fail due to lack of neighbors. A good rule of thumb is to expect true scaling from, at best, roughly 1/4 attractor size down to 3 times the noise level. The relative location of the true scaling region will vary as one increases the embedding dimension, this is an artifact both of having finite data and the presence of noise. Using a sup norm or maximum norm will also lower this affect by introducing m scaling directly into the measure. While in theory the choice of norm should not impact the determination of the correlation dimension, in practice you should never *quantitatively* compare dimensions computed via different norms.

It is important to state that the issues and methods of this section are far from settled in the literature, the seminal works of Lorenz received over 2000 citations since 2018 and the works of Grassberger received over 400 citations. New methods for estimating embedding parameters and of computing dimensions are also actively being proposed including the use of machine learning and complex networks. To make matters even more complicated there is now significant research into so-called non-chaotic strange attractors, or attractors with fractal dimension but that do not represent chaotic dynamics. In the opinions of the authors of this work the best overall practices for estimating correlation dimension are simply to minimize assumptions, be open about parameters and quantify error. At a bare minimum anytime a correlation dimension is reported you should also supply the saturation of that estimate as a function of embedding dimension. If one is being completely thorough it also illuminating to conduct the same analysis you did on your actual data on surrogate data, or randomly generated data sets that have the same (1) distribution and (2) spectral properties. One may also examine a randomly sorted version of the original data to inspect a phase-randomized set with the same spatial distribution. Any of these, or the set of these, should provide an excellent null hypothesis to verify your estimates on correlation dimension.

Of on going research in the area of nonlinear timeseries analysis the authors would like to highlight the 0-1 method, which as its name suggests, provides a means of labeling dynamics as chaotic, or not. The method is exceedingly intuitive and beyond simple to implement,

requiring no complex overhead of any kind. It is also as robust to noise as the measures presented in this chapter, and has even shown some promise in identifying low dimensional or weak chaos. It is particularly useful for identifying chaotic regions as one varies parameters, which can serve as filter before one spends the time necessary to complete the careful analysis discussed above. Most importantly it can provide a quick, visual identification of potentially chaotic behavior. The underlying transformation of the 0-1 test produces variables which behave as a random walk in the presence of chaos (or sufficient noise), so one can quickly visualize the underlying behavior by plotting these variables and seeing if they are bounded. The formal process of identifying chaotic behavior in the 0-1 test is a robust estimation of the diffusion constant for the transformed variables.

4.2.6 Characterizing a Chaotic Soliton

Here we provide a step-by-step worked example of estimating the correlation dimension for the 3.0 dB ring gain Chaotic Soliton presented in Section 7. This is intended only to illustrate the points made above, and provide more useful. This is a higher ring gain than was reported in the collaborative PRL with CSU, but was recorded at the time [31]. At this higher ring gain, as discussed in detail in Section 7, there are now two solitary waves propagating within the ring and the dynamic may no longer be called a chaotically modulating soliton.

1) Decide on a repeatable procedure.
Estimates on dimension are, typically, only useful when compared to others produced with the same underlying procedure. The reality is, especially when choosing fitting regions, that the results are easily tunable. Use the same methods when you determine the time delay and Theiler windows across multiple time series and to justify your choice in scaling region. If working on data which exhibits multiple scales of complexity make educated guesses before conducting any nonlinear time series analysis on where you expect the scaling regions to appear. Be upfront, demonstrate saturation with increased embedding dimension. Provide

50

information on how many octaves you are fitting in your scaling region, and how good those fits are.

2) Familiarize yourself with the data.

Naive or batch processing for nonlinear time series measures is, at best, done in poor taste. Data should at a minimum be evaluated to ensure there are no transient effects, or that it is all the the result of evolving on a single attactor. The data should also be verified to have, at some scale, a broadband power spectra and to be of general high quality and high signal-to-noise ratio. Remember that any measure on the underlying dynamical variables should also be chaotic, so consider if there are alternatives to processing the raw data (e.g., energy) which may reduce the length of the time series and therefore the computation times. Consider pre-processing options including the 0-1 test. Beware oversampling, which can even render the 0-1 test moot (spurious temporal correlation making the data appear bounded).

Our data is two solitary waves propagating around the ring, both modulating, but with very different group velocities and amplitudes. The faster soliton is circling the ring every 5 round trips. Maximum soliton high will miss most of the dynamics, and round trip energy is quasi-conservative in this system so not an ideal chaos measure. We will use the full data binned to reduce the effective sampling rate by 10.

3) Determine embedding parameters

Choose an embedding parameter, typically either using the autocorrelation or mutual information. Verify visually via return plot (scatter plotting two reconstructed time-delay vectors) that the dynamics are unfolded. Estimates should be robust against reasonable variation in the choice of time delay. Visually verifying the first zero of the auto mutual information as a reasonable time delay choice is shown in Figure 4.4. The dynamics are well spread out in (a) where the time delay is the first zero crossing. In (b) and (c) the time delay is prime multiples of the first zero crossing and dynamics are pushed into the axes and the

diagonal, respectively.
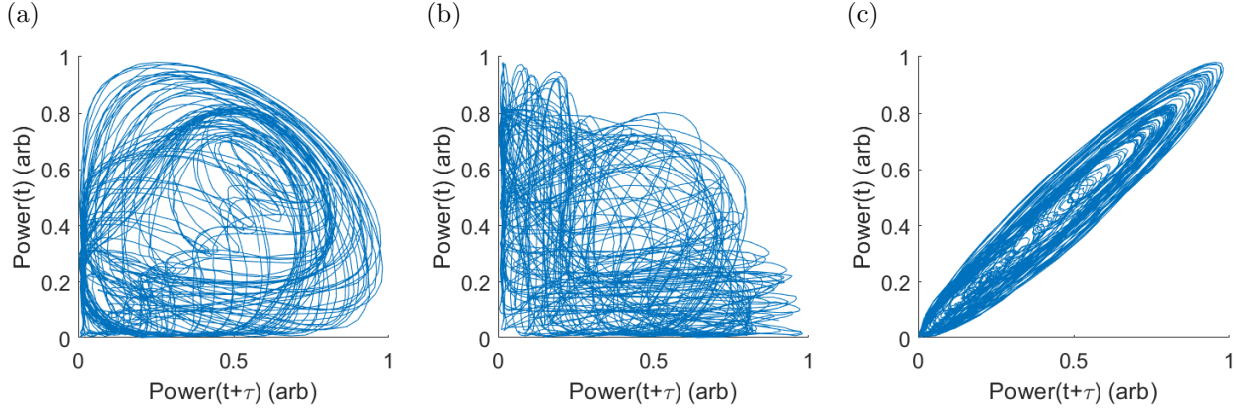
Figure 4.4: Visualizing time delays with return plots. All plots feature 1000 round trips of data from the 3.0dB CSU chaotic soliton experiment. (a) Return plot with the time delay set to the first zero of the average mutual information. Orbits occupy the available space. (b) Time delay set to 3x the delay used in (a), dynamics are now being pushed toward the axes and not evenly spread. (c) 11x the delay in (a), dynamics are completely unfolded and only occupy the diagonal.

4) Compute the correlation sums.

Compute the correlation sums for the data up to a reasonably embedding dimension. Usually 20 or 30 will suffice. Ideally you would like 10 or 15 embedding dimensions above the minimum. I.E. for an attractor of dimension $d_a = 5$ where a minimum embedding dimension of $m > 2 * d_a = 10$ is necessary computing up to embedding dimension 25 or 30 will allow you compute error bars on your estimate. Once you have the sums computing try to identify scaling regions. Computed correlation sums for the 3.0 dB chaotic soliton time series is shown in Figure 4.5. In (a) correlation sums corrsponding to even embedding dimensions are shown for clarity. In (b) the local derivative of the correlation sum, an pointwise estimate of correlation dimension, is shown. This is computed via triple point derivative and smoothed via moving average. The same scaling regions can be observed in both with noise dominating below $\ln(\epsilon) = 2.5$ and the scale of the attractor dominates above $\ln(\epsilon) = 1.5$. A true scaling window lies in the middle.
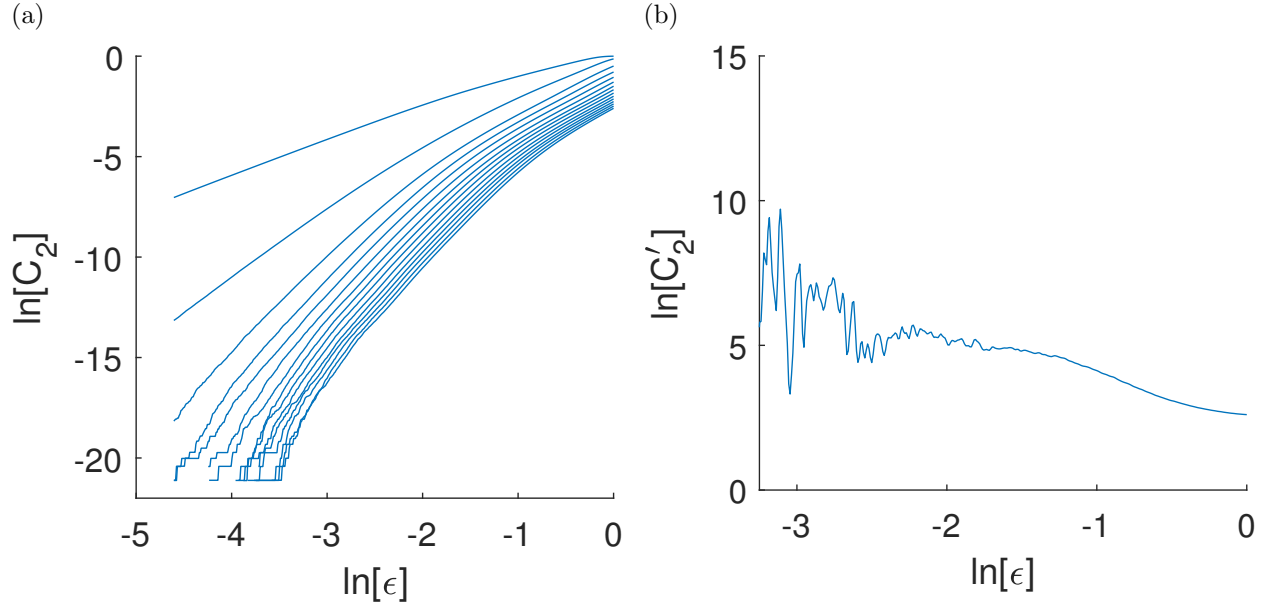
Figure 4.5: Correlation sums for 3.0 dB Chaotic Soliton (a) correlation sums for the even embedding dimensions (2-30). A true scaling region may be identified at roughly $2.5 > \ln(\epsilon) > 1.5$ above the the scale of the attractor may been seen to dominate and below noise and loss of neighbors dominates. (b) The local derivative of the correlation function for embedding dimension 30. The same scaling regions as before may be identified. Note the derivative is computed via triple-point and has been smoothed via moving average. This is a fairly convincing plateau for experimental data.

There are a few important points which should be emphasized here. (1) The relative location of the scaling region as a function of ϵ can be seen to shift as the embedding dimension is increased. As discussed above, this is an artifact of a finite data set, the presence of noise and the use of euclidean norm. (2) As we shift from the true scaling region towards either $\epsilon \to 0$ or $\epsilon \to -\infty$ the correlation sum **curves** towards $D_2 \to 0$ or $D_2 \to m$ as the local scaling becomes dominated by geometric features of the attractor or noise in m space. Fitting a linear line to a curve allows for complete tunability of the slope where one can increase the slope by shifting their fit towards smaller ϵ or lower it by shifting towards larger ϵ. This is why it is so important include shifts like this in your error bars for estimation, as it will indicate the region you are fitting is not on a curve. (3) The local dimension estimations from triple point derivative appear fairly noisy. This is very common and is again an artifact of finite data and the fact that when computing the correlation sum one does not include all possible neighbors for the sake of tractability. It is also important to realize we are looking for a scaling *region* of the correlation integral and a pointwise definition is not illuminating. (b) Serves as an additional way to verify the location of scaling regions and can offer some insight into the error of the estimation. Note that the scaling region shown in (b) is a fairly clean and convincing plateau for real data, which should reinforce ones skepticism about reported dimensions without supplimental information or saturation. Other examples with experimental data are shown in Kantz [60].

4) Fit the identified scaling region.

Linear fits should be made to the identified scaling regions and goodness of fit measures used to explicitly justify the choice of scaling region. In general scaling regions should be identified individuality for each embedding dimension. We recommend refitting with $\pm 5\%$ shifts on the edges of the scaling region as another means of quantifying error for this highly subjective step. This is to demonstrate the fitting region does not line on a curve, as discussed above. Saturation of correlation dimension across embedding dimension is shown in Figure 4.6. A

saturation in the measure of our invariant D_2 as a function of embedding dimension is shown in (a) and estimated to be 5.27±0.08 including variations caused by fitting location choice. The saturation is seen to begin at $m = 10 \approx= 2d_a$, but only embedding dimensions 15-30 were used for the estimation.

(a)

(b)
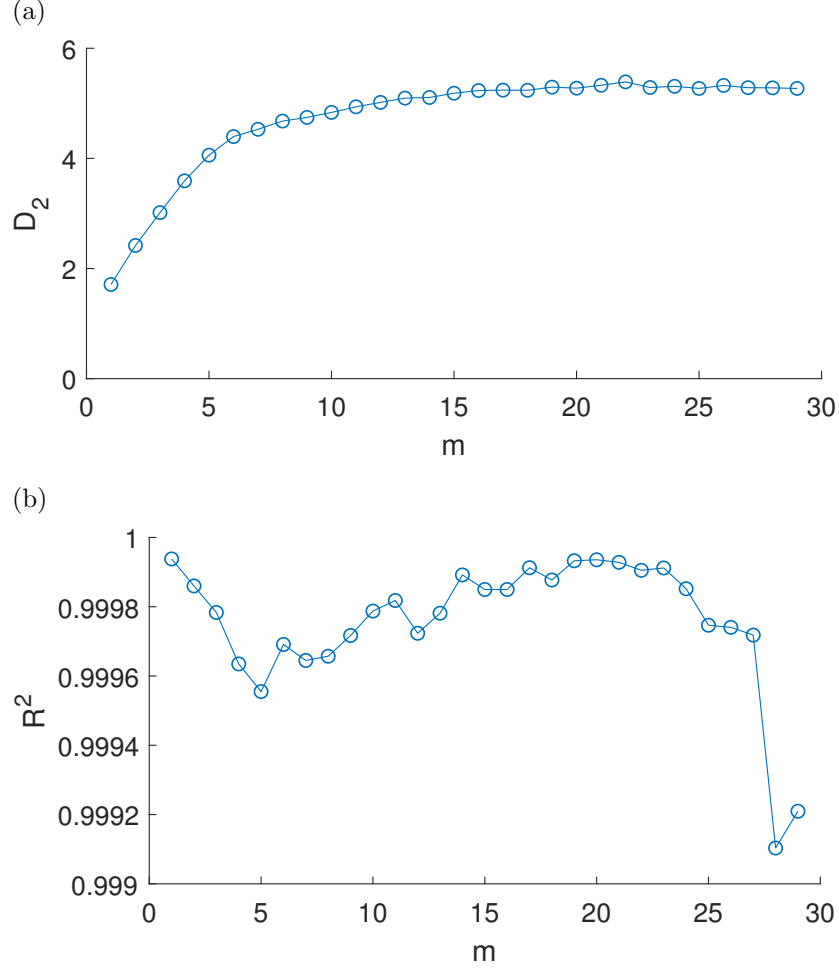
Figure 4.6: Correlation Dimension for 3.0 dB Chaotic Soliton (a) Saturation of estimation of correlation dimension from computed correlation sum for increasing embedding dimension. Saturation is seen to occur at $m = 15$. (b) $R^2 = 0.999$ for each the linear fit at each embedding dimension. Correlation dimension is estimated to be 5.27±0.08 including variations caused by fitting location.

4.2.7 TISEAN

A majority of the time series analysis tools used in this work are part of the TISEAN software package which includes implementations of all methods discussed above [60, 85].

The principle benefit of the TISEAN package is its implementation of a fast nearest neighbor search reduces the task from N^2 to an asymptotic limit $N \log N$. This allows for the practical evaluation of data sets orders of magnitude larger than a traditional Grassberger and Procaccio algorithm.

The algorithm $d2$ in the TISEAN package includes several novel optimizations for calculations of the correlation sum. It uses nearest neighbor searching at small length scales, where the algorithm's efficiency approaches $O(N)$ and for large length scales only portions of the data are evaluated. The algorithm demands a minimum number of points, which is specifiable, for each length scale that is evaluated. This allows one to ensure the statistical quality of each length scale while avoiding excessive calculations times.

The TISEAN package also includes implementations of Lyapunov spectrum, recurrence plots, surrogates data, nonlinear noise reduction, nonlinear modeling, space time separation plots, entropy and box counting, information dimension and traditional GP correlation sums.

CHAPTER 5

COMPLEX SOLITARY WAVE DYNAMICS, PATTERN FORMATION, AND CHAOS IN
THE CUBIC QUINTIC COMPLEX GINZBURG-LANDAU EQUATION

This chapter contains a manuscript in its entirety which was previously published in the
New Journal of Physics and contains work conceived and executed by myself with analysis
help from Rachel A. Ryan. This work was conducted under the advisement of Lincoln. D.
Carr and Mingzong Wu. Note that in this work the CQGLE is referred to as the gain-loss
nonlinear Schrödinger equation.

Associated reference [34]: Justin Q. Anderson, Rachel A. Ryan, Mingzhong Wu, and Lin-
coln D. Carr. Complex solitary wave dynamics, pattern formation and chaos in the gain-loss
nonlinear Schrödinger equation. *New Journal of Physics*, 16(2):23025, 2014. ISSN 13672630.
doi: 10.1088/1367-2630/16/2/023025. Supplemental materials, including animations, are
available at the journal:

https://iopscience.iop.org/article/10.1088/1367-2630/16/2/023025.

5.1 Abstract

A numerical exploration of a gain-loss nonlinear Schrödinger equation was carried out
utilizing over 180000 core hours to conduct more than 10000 unique simulations in an effort
to characterize the model's six dimensional parameter space. The study treated the problem
in full generality, spanning a minimum of eight orders of magnitude for each of three linear
and nonlinear gain terms and five orders of magnitude for higher order nonlinearities. The
gain-loss nonlinear Schrödinger equation is of interest as a model for spin wave envelopes in
magnetic thin film active feedback rings and analogous driven damped nonlinear physical
systems. Bright soliton trains were spontaneously driven out of equilibrium and behaviors
stable for tens of thousands of round trip times were numerically identified. Nine distinct
complex dynamical behaviors with lifetimes on the order of ms were isolated as part of six

identified solution classes. Numerically located dynamical behaviors include: (1) Low dimensional chaotic modulations of bright soliton trains; (2) spatially symmetric/asymmetric interactions of solitary wave peaks; (3) dynamical pattern formation and recurrence; (4) steady state solutions and (5) intermittency. Simulations exhibiting chaotically modulating bright soliton trains were found to qualitatively match previous experimental observations. Ten new dynamical behaviors, eight demonstrating long lifetimes, are predicted to be observable in future experiments.

5.2 Introduction

Related forms of the nonlinear Schrödinger equation are used to explore nonlinear phenomena in many distinct physical systems: Ginzburg-Landau equations describe the envelope evolution of mode-locked lasers, and superconductivity [35]; the cubic nonlinear Schrödinger equation treats deep water waves [1] and the dynamics of spin wave envelopes in magnetic thin films [36, 37]; a driven damped nonlinear Schrödinger equation models exciton-polariton and magnon Bose-Einstein condensates (BECs) [38]; and the Gross-Pitaevskii equation models the mean field of atomic and molecular BECs [39, 40]. With the increasing supply of cheap computing power these systems have become the subject of extensive and sometimes rigorous numerical study.

Magnetic thin films have demonstrated potential as a versatile toy system for experiments on fundamental nonlinear dynamics [41]. Over the past two decades yttrium-iron-garnet ($Y_3Fe_5O_{12}$, YIG) magnetic thin films have been fruitfully studied by numerous experimental groups and have demonstrated a rich variety of nonlinear phenomena. These include bright and dark envelope solitons [4–10, 10–19], soliton trains [20, 21], möbius solitons [22], Fermi-Pasta-Ulam and spatial recurrence [23, 24], soliton fractals [25], random solitons [26], chaotic spin waves [27–29], multiple solitons [30], and chaotic solitons [31, 32].

A majority of these phenomena were observed on active feedback rings; such feedback structures are ubiquitous within science and physics in general. Rings in particular are commonly used to study wave dynamics when one seeks a quantized wavenumber, periodic

pumping, self-generation, or other resonant phenomena. Active rings, so called for the presence of periodic linear amplification, allow for the direct compensation of the major loss mechanisms present within a system. This permits one to drive the system into quasi-conservative regimes, enabling the observation of dynamics on scales of several to tens of thousands of round trip times. Dynamics with lifetimes of this order would otherwise be prohibited by the presence of dissipation.

Yet, within the context of spin waves in magnetic thin films, little work has been carried out to develop an adequate theory for describing the rich range of behaviors evident within these recent experimental works. The integrable cubic nonlinear Schrödinger equation (NLS), while successful in quantitatively describing both dark and bright soliton trains, is unable to reproduce more complex phenomena such as the chaotic oscillation of soliton envelopes. However, there has been significant effort within the mode-locked laser community to study analogous driven and damped systems. Works on dissipation terms and saturation [88–91], the study of dissipative solitons dynamics [92–96] and other numerical studies of the cubic quintic complex Ginzburg-Landau equation [97, 98] are highly relevant to the development of a driven damped model for spin waves in magnetic thin films. These works explore the dynamics of solitary waves and their associated wave equations under the influences of gain and loss. For example, the dynamics of near steady-state dissipative solitons have been considered in detail; such studies include rigorous mappings of stable and unstable regions of parameter space [94–96]. There have also been significant investigations made into complex soliton dynamics in optical lattices [99, 100]. Similarly, initial transient behaviors have been the subject of significant research efforts by the mode-locked laser community. Transients are of interest for potential applications in signal processing and communication. To date there have been no efforts towards the characterization of long lifetime (> 1 ms) dynamics of soliton trains driven from equilibrium within active feedback rings. The work presented here demonstrates such an effort for a generalized nonlinear Schrödinger equation with a focus on applications to nonlinear spin waves propagating in an active feedback ring.

Our paper is outlined as follows. Section 5.3 introduces the model to be studied along with the associated operating limits; here the methodology and scope of the simulations are explicitly defined. Experimental contexts for the work are also considered in Section 5.3. Results in the form of eleven unique complex dynamical behaviors are presented and categorized in sections 5.4-5.8. Section 5.4 contains simulations of chaotically modulating soliton trains. Spatially symmetric and asymmetric solitary wave interactions are presented in Section 5.5. Four examples of dynamical pattern formation are given in Section 5.6. Two cases of steady state evolution are reported in Section 5.7. Intermittent solutions are discussed in Section 5.8. Finally, a discussion of numerical convergence and solution robustness is given in Section 5.9. The work is summarized in Section 5.10.

5.3   Model Overview

To study the long lifetime dynamics of soliton trains driven from equilibrium, motivated by the works discussed in Section 5.2, we propose a generalized governing equation for spin waves in magnetic thin film active feedback rings: the *gain loss nonlinear Schrödinger equation* (GLNLS),

$$i\frac{\partial u}{\partial t} = \left[-\frac{D}{2}\frac{\partial^2}{\partial x^2} + iL + (N + iC)|u|^2 + (S + iQ)|u|^4 \right] u \qquad (5.1)$$

where $u = u(x, t)$ is a dimensionless complex magnetization amplitude defined as $|u(x,t)|^2 = \mathbf{m}(x,t)^2/2\mathbf{M_s}^2$; here $\mathbf{m}(x,t)$ is the dynamic magnetization while $\mathbf{M_s}^2$ is the saturation magnetization; D is the dispersion coefficient; N and S are the cubic and quintic nonlinearity coefficients, respectively; t is the 'temporal' evolution coordinate; x is the 'spatial' coordinate of propagation boosted to the group velocity of the envelope; and L, C, and Q are the linear, cubic, and quintic gains (losses) if positive (negative). All parameters are taken to be real as the complex nature of the coefficients is explicitly accounted for in Equation 5.1. The local intensity of the magnetization amplitude is given by $|u(x,t)|^2$. The norm and energy at a

given time, t, are defined as

$$\|u(t)\|_2 = \int_0^L \mathrm{d}x \; |u(x,t)|^2, \tag{5.2}$$

and

$$E(t) = \int_0^L \mathrm{d}x \left[\frac{D}{2} \left| \frac{\partial u(x,t)}{\partial x} \right|^2 + (N + S|u(x,t)|^2)|u(x,t)|^2 \right], \tag{5.3}$$

respectively, where the integrals are taken over the length or circumference, $2\pi R$, of the feedback ring. All norms, intensities and energies given within figures and animations are scaled by $\|u(0)\|_2$, $\max[|u(x,0)|^2]$ and $\mathrm{abs}[E(0)]$ respectively where $t = 0$ corresponds to the initial condition used during numerical simulation. Numerical values given within the text are not scaled. The specific choice of initial condition is discussed later in this section.

The gain and loss present within the GLNLS may be viewed as an expansion of saturable loss expressions studied separately by Ablowitz and Akhmediev [89, 90, 94, 95]. The higher order nonlinearity, S, may be used either as a saturation of cubic nonlinearity or an additional self-steepening; both cases are studied in the literature [1]. The GLNLS omits other terms commonly included in cubic quintic complex Ginzburg-Landau equations such as spectral filtering, periodic pumping, and integral mean terms, as they are not needed in this physical context. We are likewise compelled by Occam's Razor to choose the simplest possible model which nevertheless reproduces measurements in magnetic thin film active feedback rings. NLS-like equations may be derived in magnetic thin films by use of a slowly varying envelope approximation [2], more rigorously through conservation considerations and a Hamiltonian formalism [3, 4], or directly from Maxwell's equations using multi-scale methods [101]. The operating limits of the GLNLS are motivated principally by experimental work on the excitation of chaotic solitons in YIG strip-based active feedback rings [31]. A block diagram of the active feedback ring experiment is shown in Figure 5.1. The ring is comprised of a nonlinear propagation medium, in this case a magnetically saturated crystalline YIG thin film, connected via two transducers to an electronic feedback loop. The electronics loop is constructed of a directional coupler, allowing real time observation at
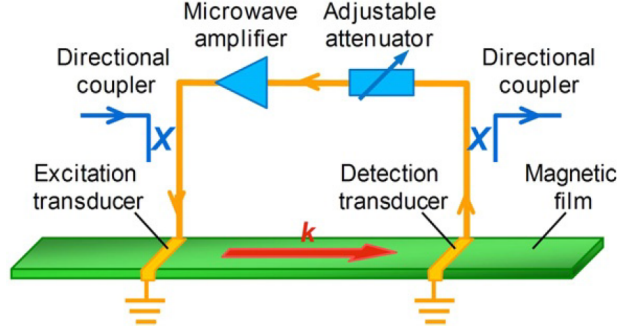
Figure 5.1: Diagram of active feedback ring experimental apparatus. Reprinted with permission from Elsevier [41].

an oscilloscope and/or spectrum analyzer, and an amplifier/attenuator pair for real time adjustment of ring gain. The GLNLS demonstrated qualitative agreement with the low dimensional chaotic modulation of a bright soliton train, as will be discussed in Section 5.4. Detailed experimental results are discussed in Wang *et al* . [31]. These experiments indicate that nonlinearity and dispersion are the dominant sources of envelope shaping for chaotic spin wave solitons and that the losses present in the ring are fully compensated for by the amplifier. This imposed two constraints on modeling. (1) The coefficients N and D must be orders of magnitude larger than L, C, and Q. (2) The linear amplifier must compensate both the linear and nonlinear losses present in the film, requiring a net averaged (over many round trips) linear gain, $L > 0$. Likewise, the dissipative terms represent the net gain and loss processes occurring in the ring averaged over several round trip times. One expects the use of this approximation, and therefore the model, to be valid when the time scale of envelope modulation is much greater than the soliton round trip time.

All simulations of the GLNLS were performed using adaptive time step Cash-Karp Runge-Kutta for temporal evolution and pseudospectral techniques for spatial propagation [50, 51]. Periodic boundary conditions modeled propagation around a ring. Note, a detailed discussion on numerical convergence for complex dynamics may be found in Section 5.9. Every simulation began as a bright soliton initial condition obtained via imaginary time

relaxation [102], the ground state solution to the GLNLS with S, L, C, and Q set as zero, with $|u(x,t)|^2 < 1$. Experimentally this corresponds to a stable bright soliton circling within a YIG strip-based active feedback ring, a solution analogous to a soliton train. Dynamical results were generated by driving this bright soliton initial condition out of equilibrium via numerical propagation under the influences of non-zero gain and loss terms. This is a process analogous to active feedback ring experiments where gains are increased beyond those which support stable bright soliton trains [14, 23, 25, 31, 103]. As previously motivated in Section 5.2 we are interested in identifying dynamical behaviors which are stable on timescales observable in magnetic thin film active feedback ring experiments, (> 1 ms) or 7000+ round trips, and analogous physical systems. For this reason any transient dynamics which occurred as a result of driving the bright soliton train out of equilibrium were not explicitly studied within this work, so long as such dynamics were numerically converged. Finally, a rigorous study of transient dynamics is more appropriately done via an iterative simulation method, rather than the slowly varying envelope approximation used here.

Physical GLNLS parameter values are obtained by fitting this initial condition to experimentally observed bright soliton train conditions. This choice of units also fixes the ratio of N/D used in simulations, while the amplitude of N and D dictate the simulation timescale. We assumed that the dimensionless spin wave intensity is directly proportional to the spin wave power, $|u(x,t)|^2 \propto P_{\text{out}}$, since experimental measurements of voltage are taken across a diode with quadratic behavior and are generally taken to be proportional to power. Values typical for a chaotic soliton experiment are $T = 165$ ns, the round trip time; $d = 0.55$ cm, the transducer separation; $T_{\text{e}} = 10$ ns, the electronic loop propagation time; $V_{\text{g}} = d/(T - T_{\text{e}}) = 3.5 \times 10^6$ cm/s, the group velocity; $N = -9.24 \times 10^9$ rad/s, the cubic nonlinearity; and $D = 510$ cm^2/s, the dispersion. Using these parameters one finds $[t] \approx 25$ ns where t is the scaled temporal unit used in simulations. This relation may be used to immediately transform code values for L, C, Q and S, which share units of inverse time, to physical values. For example the largest studied linear gain is $L = t^{-1} \approx 0.05\,\text{ns}^{-1}$ which

matches the order of experimentally approximated linear losses for magnetostatic backward volume spin waves in YIG thin films [103]. Experimentally a time series is recorded at the detection transducer with the full waveform being captured once a round trip after the signal has propagated a length d between the transducers and passed through the electronics loop. The length of the ring, ℓ, is taken to be the transducer separation, d, as the propagation delay is orders of magnitude smaller than the round trip time, $T_e < T$. Simulations explicitly model the entire feedback loop at the group velocity of the waveform. A time series may be reconstructed from numerical data by concatenating the simulated waveform after a temporal evolution of T or a spatial evolution of $d = \ell$. In this work we adopt the former convention to ease the direct comparison of simulations to the power vs. time data often observed experimentally for spin waves in magnetic thin films. Such a reconstructed time series is labeled $u_{\mathrm{ts}}(t)$ throughout the paper. A time series of solitary wave peak intensity at successive round trips is useful in studying modulating single solitary wave trains and is defined by

$$|u_{\mathrm{peak}}(t)|^2 = |\max\left[u(x, nT)\right]|^2, \ \ n = 0, 1, ..., N_{\mathrm{RT}}, \tag{5.4}$$

where T is the round trip time and N_{RT} is the total number of round trips.

Parameter space explorations were explicitly chosen to encompass the GLNLS operating regime for magnetic thin film systems, while extending into other limits that could be of interest to other systems where the GLNLS is a useful model. Along with the previously mentioned restriction on the sign of L only cases with cubic losses, $C \leq 0$, were considered. Both instances of saturating[1] quintic gains, $Q \geq 0$, and supplemental quintic losses, $Q \leq 0$, were studied. No sign restrictions were placed on quintic nonlinearity, S. The terms were explored in a decadal fashion across the GLNLS scaled values listed here

- $L = 10^n, \ \ n \in \{0, -1, -2, -3, -4, -5, -6, -7\}$,

---

[1]A typical expression for saturable gain is given by $iS_{\mathrm{g}}\left(1 + \frac{|u(x,t)|^2}{I_{\mathrm{s}}}\right)^{-1}$ where I_{s} and S_{g} are control parameters. Expanding denominator to third order yields $iS_{\mathrm{g}}\left(1 - |u(x,t)|^2 I_{\mathrm{s}}^{-1} + |u(x,t)|^4 I_{\mathrm{s}}^{-2} + ...\right)$, hence positive quintic gain being named *saturating*.

Table 5.1: Overview of identified long lifetime dynamical behaviors solution types and the range of GLNLS parameters which support them. The signs of quintic nonlinearity, S, and gain, Q, values are identified explicitly while the sign of linear gain is taken to be positive and cubic gain is taken to be negative as discussed in Section 5.3. The order of the quintic nonlinearity, S, is often directly compared to that of the cubic nonlinearity, N. The statement $\mathcal{O}(x) \pm y$ is meant to be read *order of x plus or minus y orders of magnitude.* For example the symmetric interaction dynamic is observed when the cubic loss, C, is within plus or minus one order of magnitude of the linear gain term, L.

Dynamical Pattern Type	Sec.	$|L|$	$|C|$	Sign	$|Q|$	$|S|$
Chaotic modulation	3	$\mathcal{O}(10^{-7})$	$\leq \mathcal{O}(L)$	$+$	$\leq \mathcal{O}(L)$	$\leq 10^{-2}$
				$-$	$\leq \mathcal{O}(L)$	—
Symmetric interaction	4.1	$10^{-3} - 10^{-5}$	$\mathcal{O}(L) \pm 1$	$+$	$< 10^{-2}$	$\leq \mathcal{O}(N)$
				$-$	$< 10^{-2}$	$\leq \mathcal{O}(N)$
Asymmetric interaction	4.2	$1 - 10^{-4}$	$\mathcal{O}(L)$	$+$	$\leq \mathcal{O}(L)$	$\leq \mathcal{O}(N)$
				$-$	$\leq \mathcal{O}(L)$	$\leq \mathcal{O}(N)$
Central peak recombination	5.1	$10^{-1} - 10^{-3}$	$\mathcal{O}(L) - 1$	$+$	—	—
				$-$	$\mathcal{O}(1)$	—
Complex co-propagation	5.2	$\geq 10^{-2}$	$\leq 10^{-1}$	$+$	—	—
				$-$	≥ 1	≥ 1
Spatial shifting	5.3	$10^{-1} - 10^{-3}$	$\mathcal{O}(10^{-1})$	$+$	$< 10^{-1}$	—
				$-$	$< 10^{-1}$	$\mathcal{O}(1)$
Breathers	5.4	$10^{-4} - 10^{-6}$	$\mathcal{O}(L) + 1$	$+$	—	$\leq 10^{-2}$
				$-$	10^{-1}	$\leq 10^{-2}$
Multi-peaked solitary wave	6.1	< 1	$\mathcal{O}(L) \pm 3$	$+$	$\leq \mathcal{O}(C)$	$\leq \mathcal{O}(N)$
				$-$	$\leq \mathcal{O}(C)$	$\leq \mathcal{O}(N)$
Co-propagating solitary wave	6.2	$10^{-3} - 10^{-5}$	$\mathcal{O}(10^{-2})$	$+$	$\leq \mathcal{O}(C)$	$\leq \mathcal{O}(N)$
				$-$	$\leq \mathcal{O}(C)$	$\leq \mathcal{O}(N)$

- $C \in \{0, -10^n\}, \quad n \in \{0, -1, -2, -3, -4, -5, -6\},$

- $Q \in \{0, \pm 10^n\}, \quad n \in \{0, -1, -2, -3, -4, -5, -6, -7\},$

- $S \in \{0, \pm 10^{-1}, \pm 10^{-2}\},$

for a total of eight possible values of L and C, five choices for S, and 17 unique choices for Q. Ignoring cases with solely gains present we performed 5,470 unique simulations. An additional 1,530 simulations were undertaken with random parameters. The value for any single parameter in these simulations was generated by multiplying a pseudo random number between zero and one, from the uniform distribution, by an order of magnitude and sign chosen at random, again with uniform weight, from a parameter's allowed values, as defined above. To avoid ambiguity all statements in this paper concerning the relative size of GLNLS parameters refer to the order of magnitude and not the sign.

Over 180000 core hours were utilized to conduct more than 10000 unique simulations and convergence studies. An initial study of 3500 simulations was undertaken to explore the extent of transient effects and the numerical convergence behaviors of the GLNLS. A summary and analysis of the subsequent 7000 simulations, corresponding to over 3 TB of data, are presented in sections 5.4-5.8. Approximately 1500 simulations were evaluated in detail; the remaining simulations were spot checked for consistency. Dozens of complex dynamical behaviors were identified during the course of simulation. We call this system complex because it displays a rich variety of dynamical behaviors, including chaos, robust emergent solitary-wave features, and generally multiple scales in both space and time. Solution types were divided into three stability cases, with each case corresponding to roughly 30% of observed dynamics. The three cases are temporally stable, intermittent and unstable. Temporally stable solutions demonstrated substantial observable lifetimes, greater than 1 ms or 7000+ round trips, and robustness to variations in initial conditions of at least 10%. Evolution was found to be least sensitive to changes in S and Q and most sensitive to perturbations in L. In general the effect of changes in initial conditions tended to degrade the lifetime

66

of dynamical behaviors and push solutions towards the intermittent case. Nine temporally stable distinct dynamics and two separate cases of intermittency are discussed below. A summary of the GLNLS parameter regimes which support these identified dynamics is given in Table Table 5.1.

5.4 Chaotic Modulation

The chaotic modulation of stable solitary wave trains was observed for solutions containing strongly saturated cubic nonlinearity, $S \geq 10^{-2}$, and the lowest studied ring gains, $L = 10^{-7}$, with matching orders of cubic and/or quintic losses. A single bright soliton is observed to circulate within an active feedback ring while exhibiting complex modulations in peak intensity. Low ring losses are anticipated for this solution type, as experimentally observed chaotically modulating soliton trains have lifetimes measured in seconds. The presence of a single stable bright soliton suggests that nonlinearity and dispersion are the dominate forces in peak shaping. These are two conditions used during the derivation of the GLNLS, Equation 5.1, as discussed previously in Section 5.3.

The chaotic nature of measured time series was verified by using standard phase space reconstruction techniques available in the open source Nonlinear Time Series (TISEAN) package to arrive at a stable correlation dimension, D_2 [85]. The correlation dimension, a phase-space invariant, was estimated via computation of the correlation sum for increasing embedding dimensions of the time series [60]. The standard embedding procedure of Taken and Sauer was followed using time-delayed reconstruction of the time series [65, 66]. The time delay was chosen as the first minimum of autocorrelation to maximize the linear independence of the time delayed vectors. As the phase space was reconstructed from a single time series, a Theiler window of ten times the single round trip time was used to avoid the misinterpretation of temporal correlation as geometrical structure on the attractor [87]. If the correlation dimension was observed to saturate with increasing embedding dimension the time series was said to have a stable correlation dimension. If the stable correlation dimension was not an integer then the system was said to be chaotic.
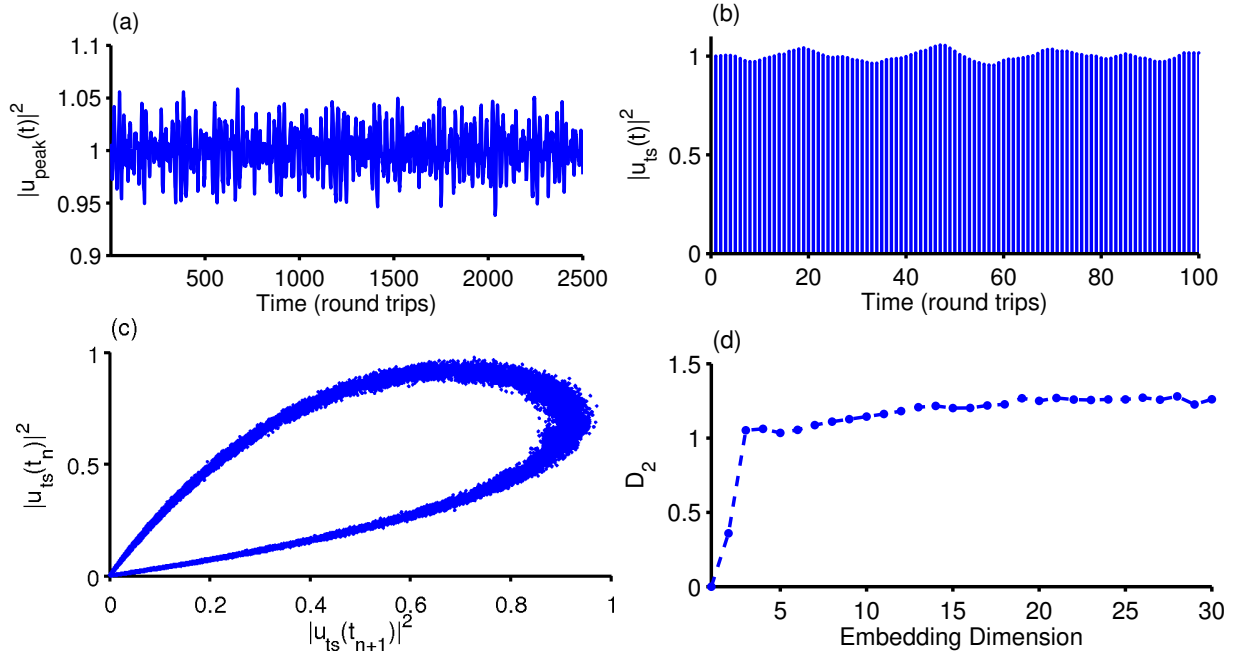
Figure 5.2: Low dimensional chaos of a modulated bright soliton train with 2.0% variation about the mean of peak intensity.(a) Peak intensity over 2500 round trips. (b) Time series over 100 round trip; each line shows the bright soliton during a single round trip. (c) Two dimensional return plot of 100000 round trips with a delay time of 1. (d) Correlation dimension vs. embedding dimension with a saturation at $D_2 = 1.26 \pm 0.03$. Dashed curve is provided as a guide to the eye; points represent actual data. Reproduced from [31].

We further required the correlation dimension to be stable across a wide range of embedding parameters as one expects the reconstructed attractor to be invariant under smooth transformations. This requirement was extremely conservative as it was computationally onerous and sensitive to noise. However, such a requirement forbids the optimization of phase space invariants by the tuning of embedding parameters, and the requirement of saturation across embedding dimension eliminates any assumptions required to study a single reconstruction. Additional indicators of chaos include broadband spectra and positive Lyapunov exponents [60]; note both these properties are shared with noise so a finite correlation dimension is necessary to demonstrate chaotic, rather than random, motion. The principle challenge to finding a stable correlation dimension was isolating a stationary solution.
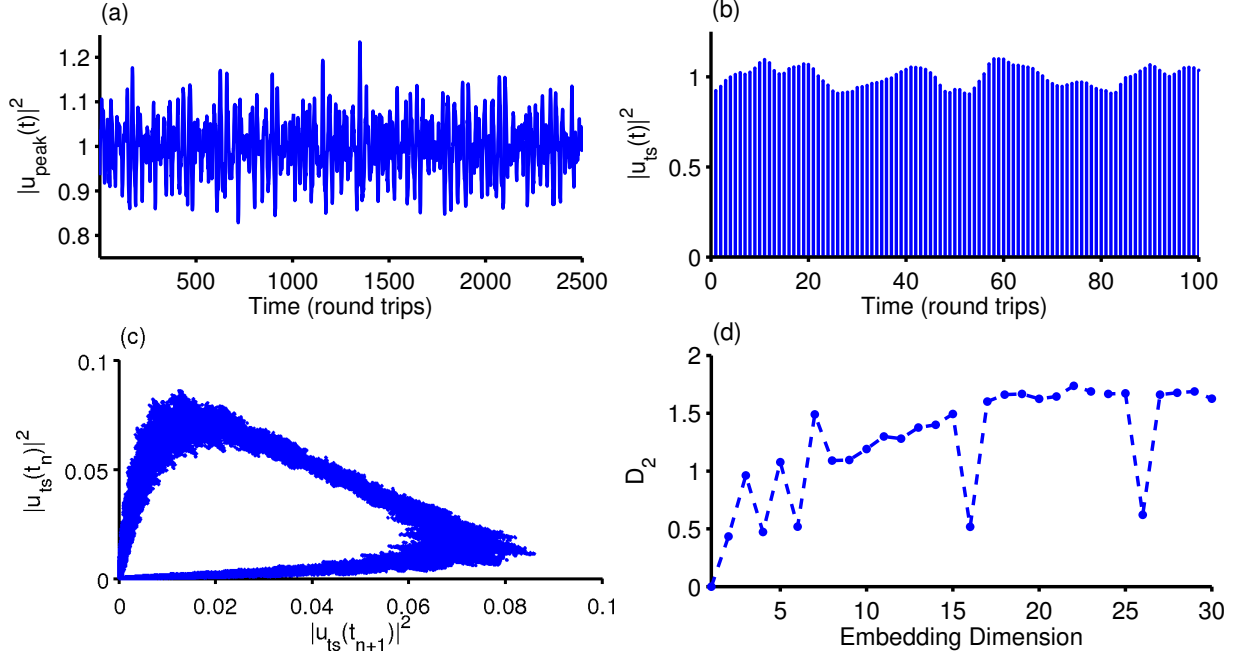
Figure 5.3: Low dimensional chaos of a modulated bright soliton train with 5.1% variation of the peak intensity and $D_2 = 1.66 \pm 0.07$. Panels treat the same variables as in Figure 5.2. Dashed curve is provided as a guide to the eye; points represent actual data. Reproduced from [31].

Two examples, with peak variations of 2.0% and 5.1% about their mean, are shown in Figure 5.2 and Figure 5.3, respectively. Percent peak variation is defined as

$$100 \frac{\text{var}\left(|u_{\text{peak}}(t)|^2\right)^{1/2}}{\text{mean}\left(|u_{\text{peak}}(t)|^2\right)}, \tag{5.5}$$

where u_{peak} was previously defined in Equation 5.4 and var is the sample variance. These values are chosen to match the peak variation of two low ring gain chaotic solitary wave trains observed experimentally by Wang *et al* . [31]. In both figures panel (a) shows the intensity of the single soliton peak for 2500 consecutive round trips while panel (b) shows 100 round trips as would be observed experimentally, as in Figure 5.4(d) below, and each vertical line is in fact a bright soliton of finite width. The single soliton peak intensity is immensely complex on inspection and is at worst random and at best chaotic or quasi-periodic. Figure 5.2(c) and Figure 5.3(c) show the phase space reconstruction for an embedding dimension of 2 and a time delay of 1, also known as a return plot, for 100000 round trips of the full time series.

69

The finite width and structure of the reconstructed attractor is one indication of chaotic, as opposed to random, motion. In Figure 5.2(d) and Figure 5.3(d) is shown correlation dimension versus embedding dimension for each variation case. Both cases saturate above an embedding dimension of 15 to a correlation dimension of 1.26 ± 0.03 and 1.66 ± 0.07, respectively. Error estimates are 95% confidence intervals given by two times the standard deviation for values of D_2 for embedding dimensions above saturation. This low dimensional chaos closely matches the low ring gain experimental observations by Wang *et al* where 2.0% variation yields a correlation dimension of $D_2 = 1.27 \pm 0.12$. However the numerically generated 5.1% peak variation does not reproduce the high dimension chaos, $D_2 = 3.83 \pm 0.21$, observed experimentally at matching variations [31]. The cause of D_2 collapse at embedding dimensions 6, 16 and 26 for the 5.1% modulation case has not been rigorously determined but is robust against reasonable perturbations in embedding parameters. The periodicity of the effect suggests the cause is related to sensitivities in the correlation sum to temporal correlations and finite time series. The embedding procedure is also sensitive to time series periodicity, which is present in these low dimensional examples [65, 66]. Low dimensional chaos often presents as widened Fourier peaks rather than pure broadband spectra. The oscillation of D_2 for low embedding dimension is a common phenomenon as the embedding procedure is not an accurate reconstruction of phase space unless the embedding dimension is at least twice the box counting dimension of the system's attractor [60].

We find numerically that amplitude of peak modulation and the dimensionality of the chaos are principally dependent on the magnitude of the saturating quintic nonlinearity, Q. The presence of both a linear gain and nonlinear loss term is necessary for a stable correlation dimension to be determined. Chaotic modulations of the train envelope are the most complex examples of a more general modulation behavior. Parameter space explorations yielded examples of bright soliton trains with no, periodic, multi-periodic or quasi-periodic modulations. We note these types of deepening modulations were experimentally observed as the first generations of soliton fractals [25].

5.5 Symmetric and Asymmetric Interacting Solitary Waves

When more than one solitary wave propagate with differing group velocities, enabling dynamics such as collisions, we say these waves interact. Two distinct cases where the spatial features of solitary wave interactions are symmetric or asymmetric under rotation are discussed below.

5.5.1 Symmetric interaction

Symmetric interaction solutions are highly complex, but ordered, gain driven interactions between a number of intensity peaks varying from two to more than twenty. These solutions evolve in intricate and complicated patterns but maintain symmetry in space under a rotation of π rads. The solution intensity exhibits a constrained modulation about a stable mean, but is energetically unstable. The energy of the system grows approximately linearly in time and is closely correlated, with a correlation coefficient of $r > .95$, to the time-averaged number of peaks present in the system. The sample correlation coefficient is a measure of the linear correlation between two variables and is defined as

$$r(\mathbf{P}, \mathbf{E}) = \frac{\text{covariance}(\mathbf{P}, \mathbf{E})}{\sqrt{\sigma_{\mathbf{P}}\sigma_{\mathbf{E}}}} = \frac{\sum_{i=1}^{n}\left(\mathbf{P_i} - \bar{\mathbf{P}}\right)\left(\mathbf{E_i} - \bar{\mathbf{E}}\right)}{\sqrt{\sum_{i=1}^{n}\left(\mathbf{P_i} - \bar{\mathbf{P}}\right)}\sqrt{\sum_{i=1}^{n}\left(\mathbf{E_i} - \bar{\mathbf{E}}\right)}}, \tag{5.6}$$

where $\sigma_{\mathbf{x}}$ is the standard deviation of $\mathbf{x}$; $\mathbf{P_i}$ and $\mathbf{E_i}$ are the number of peaks and system energy at the ith round trip. This relationship suggests every intensity peak present in the system has similar energy. Peaks undergoing symmetric interactions also demonstrate persistence in time under collisions and have linear or constant phases, both characteristics of bright solitons. Further, individual intensity peaks may also be fit to a sech^2 profile when they are spatially isolated from other peaks circulating the ring. A typical example is illustrated in Figure 5.4(a) by a spatiotemporal plot of intensity across 800 round trips, each vertical slice shows the waveform on the ring at a specific round trip. There exists a stark symmetry in dynamics with respect to a rotation by π rads. Figure 5.4(b) and (c) show the scaled norm and energy, respectively, for the same time frame. Over these

800 round trips we note the norm varies about a stable mean by $\pm 1\%$ while the system energy increases by 8%. A reconstructed time series of data presented in panel (a) is shown in Figure 5.4(d) to indicate what the behavior would look like if measured experimentally at a single observation point and discretely in time. We note that the symmetry demonstrated by the spatiotemporal intensity plot, Figure 5.4(a), is not evident in what appears to be a highly noisy time series. Whether the symmetry observed numerically persists when the iterative nature of amplification and transmission delays in an electronic feedback loop are considered remains an open question.
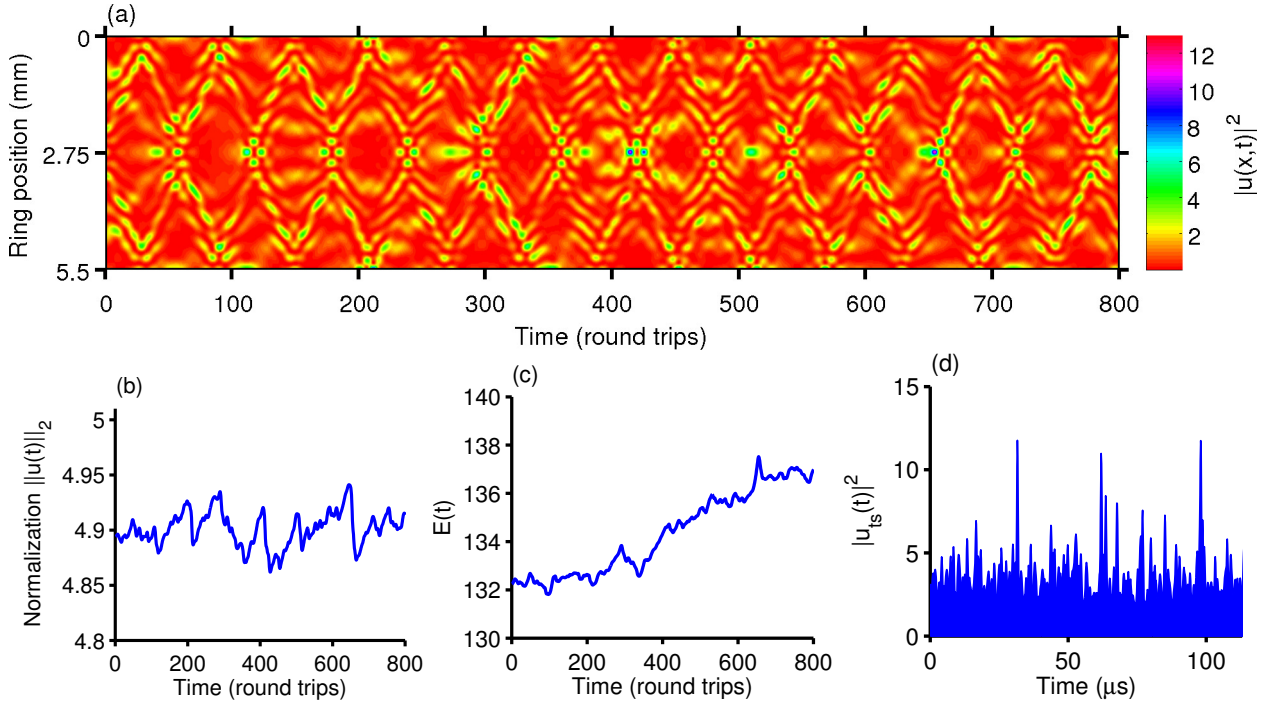
Figure 5.4: Typical example of a symmetric interaction simulation over 800 round trips of evolution. A stark spatial symmetry about the center of feedback ring, $x = 2.75$mm, is shown in a spatiotemporal plot intensity in panel (a). Symmetric interactions are energetically unstable, see panel (c). Spatial symmetry is not obvious in a reconstructed time series of numerical data, panel (d), which mimics typical experimental data collection (temporally discrete observation at a single point).

Symmetric interactions are observed to evolve in systems with linear gains between 10^{-5} and 10^{-3} and cubic losses of the same, or ± 1, orders of magnitude. This long time stable evolution requires a near-balanced system where linear gain is the dominant force and peak

growth is meaningfully restricted by the presence of nonlinear losses. No solutions had initial peak growth above 400% prior to the initial splitting event.

The dynamics within this regime demonstrate a characteristic splitting process, diagrammed in Figure 5.5(a)-(d). The initial bright soliton modulates and grows until the domination of linear gain over nonlinear loss in low-intensity regions yields a nonzero intensity floor. Energy enters the system until these low lying excitations reach intensities where attractive nonlinearity and dispersion may shape the excitation into a stable solitary wave close in form to the well-known hyperbolic secant. The new peak then begins to interact with its neighbors. This same procedure results in the generation of a second, then third, and so on, intensity peak. Thus, in contrast to more typical nonlinear partial differential equations which give rise to fixed soliton dynamics for all times, the GLNLS here displays a particular soliton dynamics on long but not infinitely long time-scales. This gives rise to the possibility of a new form of integrability which is relevant on long but not infinite times, and may require the development of new mathematical formalisms, in particular a multiscale approach in time. The timing of the initial splitting event varies from 100 μs to 1 ms where $t = 0$ is defined as the moment gain and losses are turned on. The effect of quintic loss/gain is superficial to this solution category until orders above 10^{-2} when it begins to dominate the dynamics. Quintic losses (gains) result in slower (faster) rates of initial splitting, but do not have any meaningful impact on the rate of energy gain. This splitting process is stabilized (weakened) by the addition of an attractive (repulsive) quintic nonlinearity term of the same order as the cubic present in the system. Higher orders of quintic nonlinearity destroy the stability, driving the dynamics into the intermittent regimes described later in Section 5.8. This solution type demonstrates a high sensitivity to initial conditions, which is discussed in Section 5.9. A single round trip of a symmetric interaction solution closely resembles the multi-peaked solitons previously reported by Wu *et al* . [30].
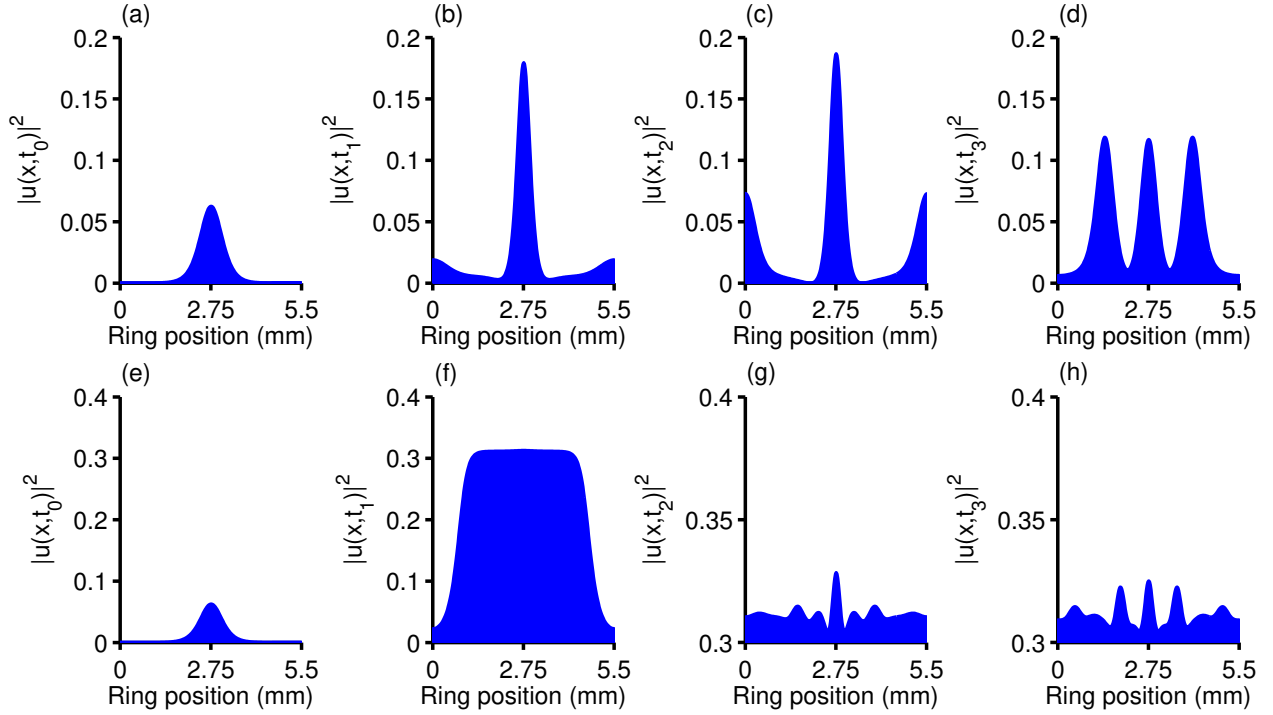
Figure 5.5: A schematic contrast of the splitting process for symmetric interactions, (a)-(d), and asymmetric interactions, (e)-(h). Each subplot shows the intensity for a single round trip at time $t_0 > t_1 > t_2 > t_3$. The series progress from left to right. (a)-(d): The symmetric case illustrates a system with linear gain and nonlinear loss near balance, resulting in a slow increase of low intensity regions while peaks are regulated by losses. Once the floor reaches intensities where nonlinearity affects dynamics, additional solitary wave peaks form, a gain driven process which often takes hundreds of microseconds. (e)-(h) In contrast the asymmetric system has high linear gains and high nonlinear losses resulting in a flattening of the peak into a plateau with $|m|^2 > 0$ upon which dynamics occur. A fast splitting process which occurs on the order of microseconds. Subplots (g) and (h) have been adjusted to the plateau height.

5.5.2 Asymmetric Interaction

Asymmetric interaction solutions are loss driven solutions which behave similarly to the symmetrical case discussed in Section 5.5.1 but do not maintain a spatial symmetry with respect to rotations around the ring. The number of interacting peaks was observed to vary from five to twenty depending on the parameters of the simulation. The total number of peaks is constant, in an average sense, after spatial symmetry about the feedback ring center breaks and is closely correlated, $r > 0.98$, to the system's energy. Here r is the sample
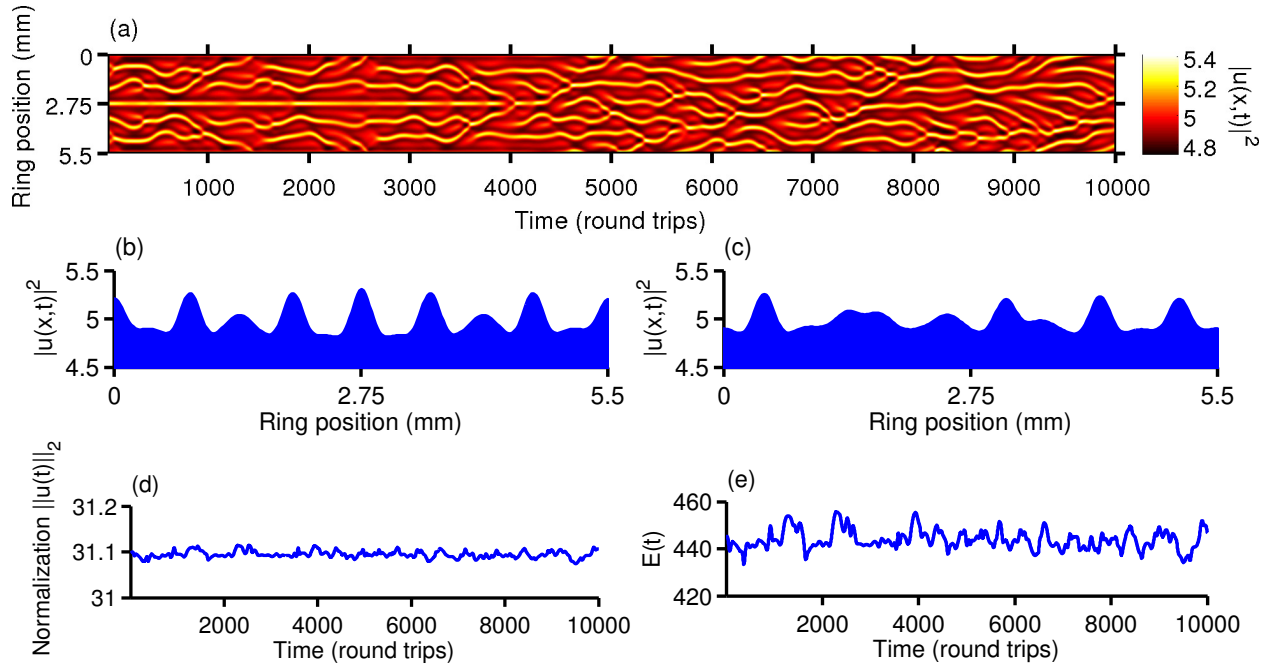
Figure 5.6: Typical example of a asymmetric interaction solution type over 10000 round trips. Spatial symmetry about the feedback ring center, $x = 2.75$mm, can be seen breaking near round trip 4300 in the spatiotemporal intensity plot, panel (a). A spatially symmetric wave form intensity, of round trip 2000, is shown in panel (b) while an asymmetric waveform, round trip 9000, is shown in panel (c).

correlation coefficient defined by Equation 5.6. An example is shown in Figure 5.6(a) by a spatiotemporal plot of intensity over 10000 round trips. Symmetry about the feedback ring center, $x = 2.75$ mm, can be seen breaking near round trip 4300. An animation of this symmetry breaking is available online. A scaled intensity plot of a single symmetric (asymmetric) round trip is shown in Figure 5.6(b) (Figure 5.6(c)). The interacting peaks are seen to be node-less, and evolve about a non-zero, $|u(x,t)|^2 > 0$, intensity floor. The stability of the asymmetric interaction solution type is demonstrated in Figure 5.6(d) and (e) showing scaled norm and energy, respectively, over the same 10000 round trips. Normalization varies about a stable mean by $\pm 0.001\%$ while energy modulates by $\pm 3\%$; this stands in contrast to the energetic instability inherent to symmetric interactions, Section 5.5.1.

Asymmetric interactions are observed in systems with linear gains, L, between 10^{-4} and 1 and cubic loss, C, of the same order of magnitude. Quintic gains and losses, Q, are

stable up to this same order of magnitude. The number of peaks and peak height increased (decreased) with the presence of attractive (repulsive) quintic nonlinearity of the same order as the cubic. Higher orders of quintic nonlinearity push the solution into intermittency, a temporally unstable class of solutions discussed in Section 5.8. The solution intensity floor varies with parameter choice, including nonlinearity, but trends towards the constant intensity which satisfies the energy balance of the GLNLS. The balance is given explicitly by the expression

$$L + C|u(x,t)|^2 + Q|u(x,t)|^4 = 0 \;\Rightarrow\; |u(x,t)|^2 = \frac{-C \pm \sqrt{C^2 - 4QL}}{2Q}, \qquad (5.7)$$

where L, C, Q and $u(x,t)$ are the same terms as in Equation 5.1 discussed in Section 5.3 and we choose the smallest positive solution. For the simulation shown in Figure 5.6 we have $L = 0.1$, $C = -0.01$, and $Q = -1$ corresponding to an average solution intensity of $|u(x,t)|^2 = 0.3113$ which closely matches the numerically observed value of $|u(x,t)|^2 = 0.3109 \pm 1.5 \times 10^{-4}$. Error bounds are given by two times the standard deviation of intensity across all available round trip data.

This regime demonstrates a characteristic splitting process, diagrammed in Figure 5.5(e)-(h). An initial bright soliton initial condition grows and flattens into a plateau under the influence of a strong linear gain and saturating nonlinear losses. Once the non-zero plateau expands to fill the feedback ring the central peak undergoes a splitting procedure similar to that observed for symmetric interactions, diagrammed in Figure 5.5(a)-(b). The domination of linear gain over nonlinear losses in low amplitude regions produces small peaks. These smaller excitations grow until the system's attractive nonlinearity and dispersion shape them into solitary wave intensity peaks. Unlike the process for symmetric interactions, Section 5.5.1, this splitting process occurs within the first 10 μs of evolution, where t = 0 is defined as the moment gains and losses are turned on, and saturates within the first 1 ms yielding an energetically stable excitation. The amplitude of intensity peaks relative to the plateau intensity varies from 1% to 10%, but the peak heights measured from the plateau

mean are of the same order as those observed in symmetric interactions.

This solution type demonstrates a high sensitivity to initial conditions, which is discussed in Section 5.9. This sensitivity and the highly complex nature of the evolution are hallmarks of chaotic dynamics. However, attempts to arrive at a converged correlation dimension using the methods discussed in Section 5.4 were inconclusive. Such sensitivity is typically characterized by a positive Lyapunov exponent [60]. While a careful determination of the largest Lyapunov exponent requires a rigorous reconstruction of phase space we may estimate the exponent numerically by evolving nearby trajectories in time. Direct measurement suggests a Lyapunov exponent between $\lambda = 2 \times 10^4 \ s^{-1}$ and $\lambda = 1 \times 10^5 \ s^{-1}$. This rate of trajectory separation is of the same order as that observed experimentally ($\lambda = 1.9 \pm 0.2 \times 10^5 s^{-1}$ [31]) for the 5.1% modulating soliton train discussed previously in Section 5.4.

5.6 Dynamical Pattern Formation

Four distinct robust dynamical patterns which demonstrate lifetimes of at least 1 ms or 7000 round trips were located during GLNLS parameter space exploration. Solutions of this group differ from previously discussed solution behaviors in that they exhibit a periodic recurrence of their characteristic dynamic. Self organization of this kind is common in open nonlinear systems [104]. These examples are discussed to demonstrate the breadth of pattern formation supported by the GLNLS under fixed choice of N and D. The regions of parameter space supporting dynamical pattern formation violates the assumptions underlying the derivation of the GLNLS in the context of magnetic spin waves, as discussed in Section 5.3, owing to the high order of quintic nonlinearity and losses which drive evolution. However, the GLNLS is a useful model in a variety of systems including laser cavities, as discussed in Section 5.2, and these dynamics may appear in such contexts.

5.6.1 Central Peak Recombination

Central peak recombinations exhibit a complex 5 peak solitary wave recombination pattern with a periodicity of 180-250 round trips, depending on parameter choices. This behavior

is driven by a strongly attractive quintic loss, $Q = -1$ and a linear gain of $L = 10^{-2\pm1}$ with cubic loss of $C = -10^{-3\pm1}$. The presence of quintic nonlinearity has a severely negative impact on the behavior lifetime. The median wave height of central peak recombination solutions satisfies the energy balance equation, Equation 5.7. For the example shown in Figure 5.7 we predict an average intensity of $|u(x,t)|^2 = 0.0995$, corresponding to the parameters have $L = 0.01$, $C = -0.001$ and $Q = -1$, which closely matches the observed numerical average intensity, $|u(x,t)|^2 = 0.0934 \pm 6 \times 10^{-3}$. The error estimate is defined as in Section 5.5.2.
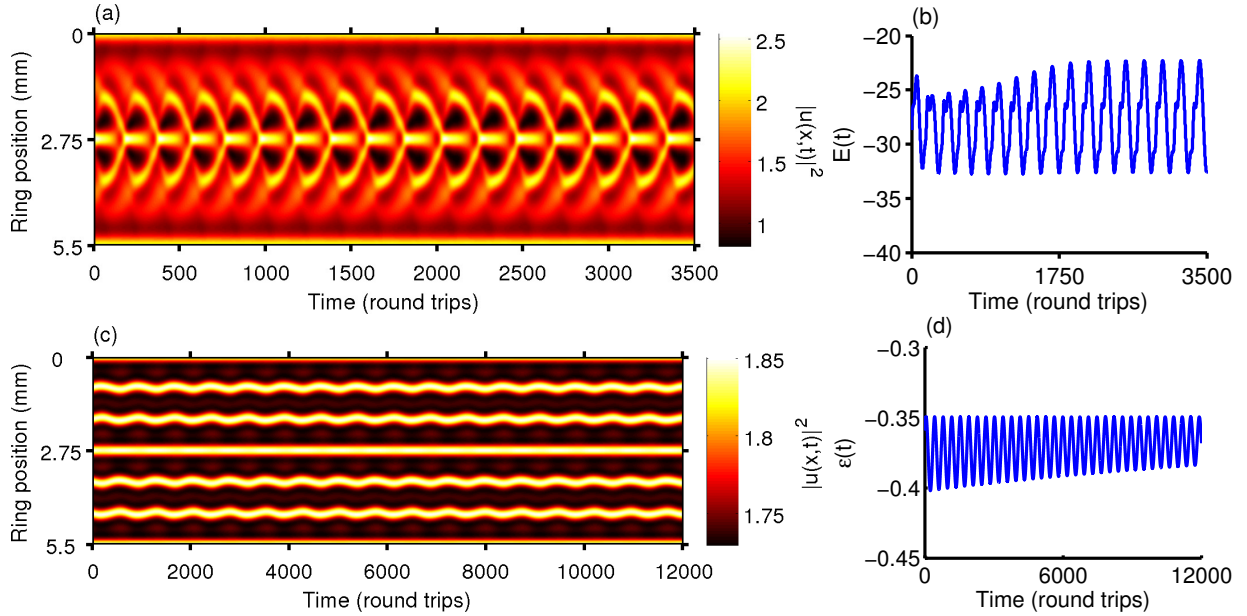
Figure 5.7: Examples of dynamical pattern formation with experimentally observable lifetimes. (a)-(b) Central peak recombination. (c)-(d) Complexly co-propagating solitary waves. In panel (d) energy has been offset for clarity, $\epsilon(t) \equiv (E(t) + 142)$.

An example of central peak recombination is shown in Figure 5.7. Panel (a) shows a spatiotemporal plot of scaled intensity over 3500 round trips and (b) shows the scaled energy over the same round trips. The periodicity of the recombination is evident in the spatiotemporal plot, which contains 16 periods. The dynamics are most readily described starting when the central peak collapses. Immediately following the collapse, the peaks on either side of the ring center propagate towards the middle of the ring and recombine into a new central peak matching the original peak's amplitude. At the same time the outlying

peaks split into two. The innermost of these new peaks grows until one finds three central peaks of equal amplitude. At this point the central peak undergoes collapse and the process repeats. A single bright solitary wave propagates unperturbed along the edge of the ring. This process is animated in an attached movie, available online.

5.6.2 Complex Co-propagation

The complex co-propagation solution was so named as it resembles the steady state co-propagation solution (see Section 5.7.2 below) and is likewise energetically stable. It differs primarily in that the waveform undergoes complex, but periodic, modulation. The dynamics also occur on a non-zero density floor satisfying the GLNLS energy balance equation, Equation 5.7. The example shown in Figure 5.7(c)-(d) was simulated with the parameters $L = 0.0987$, $C = -0.0505$, $Q = -7.6261$, resulting in an anticipated average intensity of $|u(x,t)|^2 = 0.1105$. This prediction closely matches the numerically observed intensity $|u(x,t)|^2 = 0.1104 \pm 4 \times 10^{-7}$, where the error is defined as in Section 5.5.2. Like central peak recombination the complex co-propagation behavior is driven by a large quintic loss. The dynamical patterns demonstrated by these solutions also require a large attractive quintic nonlinearity. The parameter space region which supports these behaviors is characterized primarily by large, negative quintic terms: $S = Q \geq -1$. The smallest linear gain which compensates these driving nonlinear losses is $L = 0.01$. These solutions are in general insensitive to the choice of cubic loss, with any value smaller than $C = -0.1$ supporting the observed dynamical pattern.

Figure 5.7(c)-(d) illustrates this behavior. Panel (c) shows a spatiotemporal plot of scaled intensity over 12000 round trips and (d) shows the scaled energy over the same round trips. In panel (d) the energy has been offset for clarity, $\epsilon(t) \equiv (E(t) + 142)$. The behavior is characterized by the spatiotemporal plot which shows two spatially stable bright solitary waves occupying the center and edges of the ring. The central solitary wave is flanked on each side by a set of two periodically oscillating solitary waves for a total of six large peaks being equispaced around the ring. Six additional small amplitude peaks occupy the space

between each larger wave. The entire waveform breathes between two distinct energy states with a period of 750 round trip times. The frequency of oscillation matches that predicted by a simple two-level quantum system where $\omega = \Delta E/\hbar$. For the GLNLS we have $\hbar = 1$ amd $t = 25$ ns, as defined in Section 5.3. Taking the average energy difference between states, see Figure 5.7, one predicts an angular frequency of $\omega = 7900s^{-1}$ compared to the observed oscillation frequency of $\omega = 8100s^{-1}$. An animation of the breathing is available online.
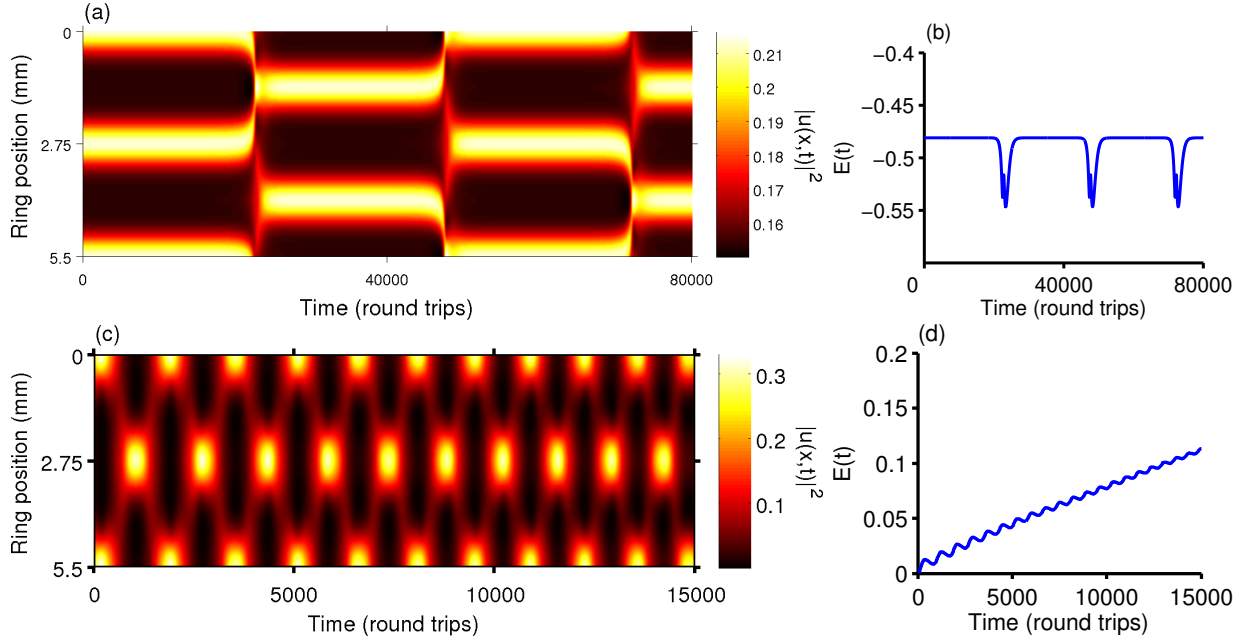
Figure 5.8: Examples of dynamical pattern formation. (a)-(b) Spatially shifting solutions. (c)-(d) Egg carton solutions.

5.6.3 Spatial Shifting

Spatial shifting solutions are simulations which exhibit energetically stable evolution with a well-defined and periodic shifting of the spatial location of the dynamical behaviors. In all observed cases the underlying energetically stable dynamics are evenly distributed bright solitary waves co-propagating on an intensity floor which satisfies the GLNLS energy balance given by equation Equation 5.7. For the example shown in Figure 5.8(a)-(b) we have $L = 0.02899$, $C = -0.06219$ and $Q = 0.000648$ corresponding to $|u(x,t)|^2 = 0.0438$ which

closely matches the numerically observed average intensity of $|u(x,t)|^2 = 0.0432 \pm 2 \times 10^{-4}$. The solitary waves spontaneously split at a constant periodicity and reform into an identical set of co-propagating peaks with a spatial shift defined as $\frac{L}{2N_s}$ where L is the feedback ring length and N_s is the number of peaks present in the simulation. All peak properties as well as the splitting dynamics remain consistent through multiple periods. A strong attractive quintic nonlinearity is required to support this dynamical behavior, as seen previously with central peak recombinations and complex co-propagation in sections 5.6.2 and 5.6.1. Spatial shifting is seen in simulations with quintic nonlinearities of $S \simeq -0.8$ and moderate linear gains of $L = 10^{-2\pm1}$. Cubic losses near $C = 10^{-1}$ support this behavior, while quintic losses were found to be unimportant until above values of $Q = \pm 10^{-1}$ where they dominated the dynamics.

An example of temporal shifting is illustrated in Figure 5.8(a)-(b). Panel (a) shows two bright solitary waves co-propagating while undergoing a spatial shift of $\frac{5.5}{4}$ mm every 22000 round trips. The shifting event occurs over 1500 round trips. Panel (b) shows the solution's scaled energy over these same round trips; the energetic stability of the co-propagation regimes is demonstrated. The energy profile of each shifting event was found to be identical.

5.6.4 Breathers

Solitary wave breathers on a ring are characterized by a single solitary wave which undergoes a periodic disappearance of the peak and reappearance at the other side of the ring. The frequency of breathing increases with system energy. The solution is not energetically stable and breathing frequency increases until the system reaches a new dynamical behavior. Numerically observed lifetimes were never less than 20000 round trips, or 3 milliseconds. The wave breathing is driven by a strong quintic loss, $Q = 10^{-1}$, with comparatively weak linear gain, $L = 10^{-5\pm1}$, and cubic loss, $C = 10^{-4\pm1}$, terms. The solution type is sensitive to the presence of quintic nonlinearity with any magnitude above 10^{-2}, whether attractive or repulsive, pushing the dynamics into the intermittent regime, discussed later in Section 5.8. Linear gain dominates during low intensity periods of the breathing behavior, resulting in a

non-zero intensity floor which ultimately drives the collapse of stable breathing.

Figure 5.8(c)-(d) contains a typical example of solitary wave breathing. The periodic spatial shifting of the bright solitary wave is seen as a relocation from the center of the ring to the other side in panel (c). An average breathing period of 1200 round trips is observed in this example. A positive linear trend in energy, see panel (d), is the result of linear gain causing growth in low-intensity regions. A periodic high rate of energy growth matches the low intensity period following the collapse of bright solitary waves. An animation of the breathing behavior is available online.

5.7 Steady State Solutions

Simulations which evolved into energetically stable static wave forms were named steady state solutions. Two distinct steady state solutions were isolated from the parameter space exploration: multi-peaked solitary waves and co-propagating solitons.
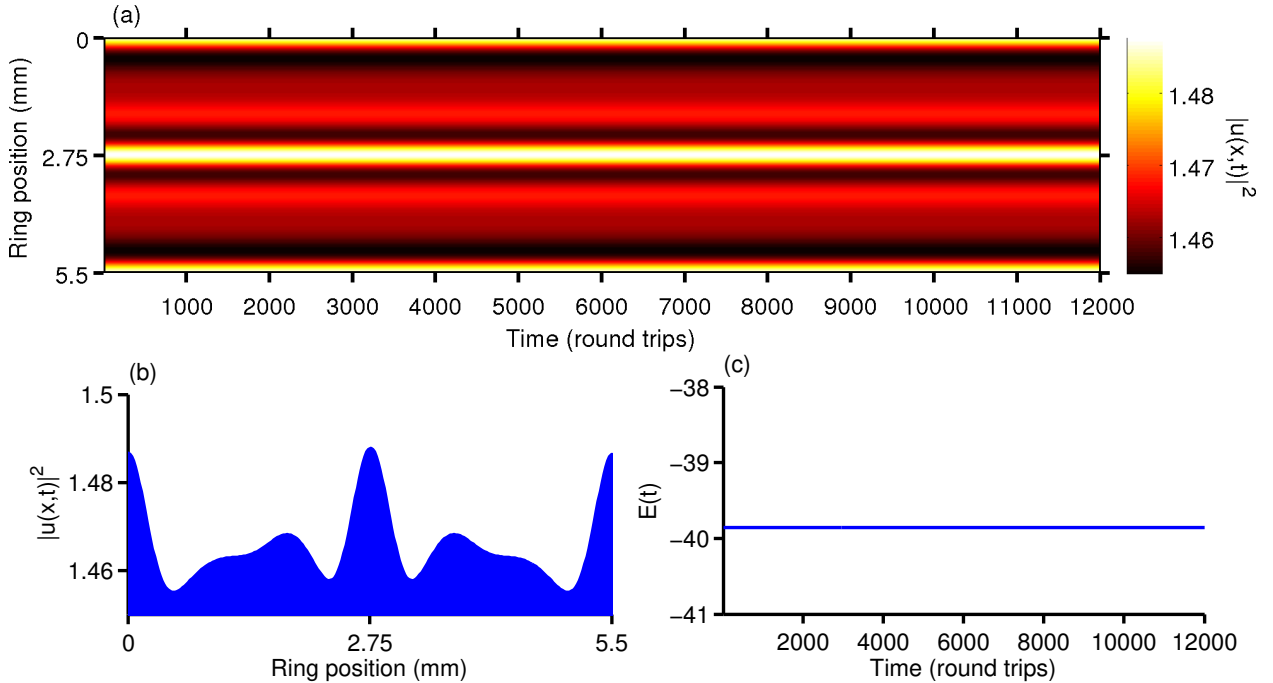

Figure 5.9: Example of a multi-peaked soliton solution type with $N_s = 2$ principle solitary wave peaks.

5.7.1 Multi-peaked Solitary Waves

Multi-peaked solitary waves were characterized by energetically stable, to machine precision, nodeless complex waveforms that evolve without exhibiting any time dependence in their intensity. The shape of the wave and the number of principle peaks varies from two to eight in studied cases, depending on parameter choice. Symmetric and asymmetric waveforms were observed. Multi-peaked solitary waves were observed for any linear gain, L, below 1 and cubic losses, C, of ± 3 orders of magnitude. The impact of quintic losses and gains principally affected the median wave height according to the GLNLS energy balance equation, Equation 5.7. For the multi-peaked solitary wave shown in Figure 5.9 we have $L = 0.1$, $C = -1$ and $Q = -1$ corresponding to an estimated average intensity of $|u(x,t)|^2 = 0.0916$ which closely matches the observed value, $|u(x,t)|^2 = 0.0916 \pm 7 \times 10^{-7}$. The error was previously defined in Section 5.5.2. As with previous examples, high values of Q relative to L lead to the term dominating dynamics and the solution leaving the steady state solution class. Positive, or saturating, values of quintic nonlinearity lead to reductions in secondary peak heights while attractive values leads to the presence of additional principal peaks via further shaping of secondary peaks. The overall shape of the multi-peaked solitary wave, including the number of principal and secondary peaks, is dependent on the choice of parameters.

A typical example is shown in Figure 5.9 of a symmetric multi-peaked solitary wave with two principle and two secondary peaks. Figure 5.9(a) shows a spatiotemporal plot of scaled intensity over 12000 round trips with each vertical slice showing the intensity across a single round trip. Panel (b) is the scaled intensity plot of the final round trip and panel (c) shows the static solution energy over the same evolution period. Not all multi-peaked solitary waves travel at the group velocity as the example in Figure 5.9. This solution type is the most commonly observed long time behavior in studied simulations and was one of the behaviors present in a majority of the intermittent cases, discussed further in Section 5.8.
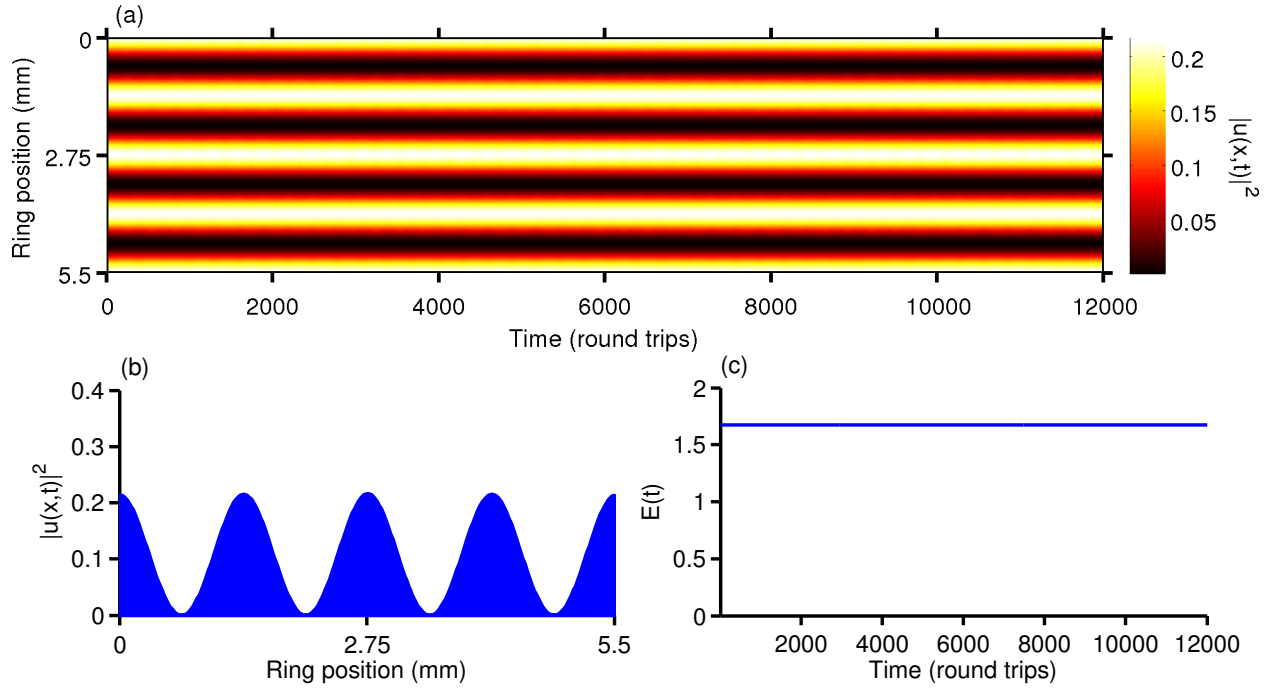
Figure 5.10: An example of a co-propagation solution type with $N_s = 4$ bright solitary waves.

5.7.2 Co-propagating Solitary Waves

Co-propagating solitary waves are the second steady state isolated during parameter space exploration. Co-propagating solitary waves are time independent solutions where N_s identical bright solitary waves propagate alongside one another without interacting. Similar N_s soliton solutions of the simple cubic NLS are well studied and the number of solitons is found to be proportional to the power of the initial condition relative to the value of N/D [1, 18]. Periodic boundary conditions require solutions have an even number of nodes. Within studied solutions N_s was observed to vary from two to eight. Figure 5.10 shows the same physical quantities as plotted in Figure 5.9, with panel (c) again demonstrating the energetic stability of the solution type. The peak shape, shown in panel (b), is not consistent with either bright or dark solitons. The example plotted in panel (a) exhibits a modulation in peak heights with a variance of $10^{-3}\%$ about the mean. While the variation is not visible in panel (a) it can be observed in an animation of the evolution, available online.

Stable co-propagation was observed only in an isolated region of parameter solutions with $L = 10^{-4\pm1}$ and $C = 10^{-2}$. Quintic gains, Q, of orders higher than the cubic present or quintic nonlinearities, S, with magnitude higher than 0.01 (the lowest order studied) drove the solution out of the steady state and in general pushed solutions into the intermittent class, discussed in Section 5.8. Lower orders of quintic gain did not have any meaningful effect on stability, the number of peaks or peak height.

5.8   Intermittent Solutions

Intermittent solutions demonstrate numerous distinct dynamical behaviors as the waveform evolves in time. The lifetime of these behaviors ranges from hundreds of round trips to hundreds of thousands. This corresponds to up to 1 ms before the dynamics transitions from one behavior to another. These solutions are robust to at least 10% variation of initial conditions in the sense that they do not degrade to noise or experience blow-up. Such perturbations do have significant effects on the relative lifetime of each dynamical behavior and even the types of behaviors a simulation exhibits. Quantitative matching of the intermittent dynamics to experiment will offer a challenge due to their highly transient nature; however, qualitative behaviors should be observable experimentally. In general, intermittent solutions spend a majority of their time in aperiodic evolution between distinct dynamical behaviors. Intermittent solutions can exhibit all of the behaviors previously described as temporally stable for a finite numbers of round trips. Intermittency is the typical dynamic exhibited when stable solutions are perturbed and is therefore not observed only in isolated regions of parameter space. Stable solutions are robust to variations in initial conditions, as previously stated in Section 5.3. Intermittency is observed when perturbations exceed 10%, however it bears mention that the necessary value is ultimately highly dependent on both solution type and the parameter being perturbed. Hundreds of intermittent simulations were identified during the study.

Two illustrative examples are shown in Figure 5.11. The same physical quantities are shown as in Figure 5.8. Panel (a) shows a typical simulation with three distinct multi-peaked
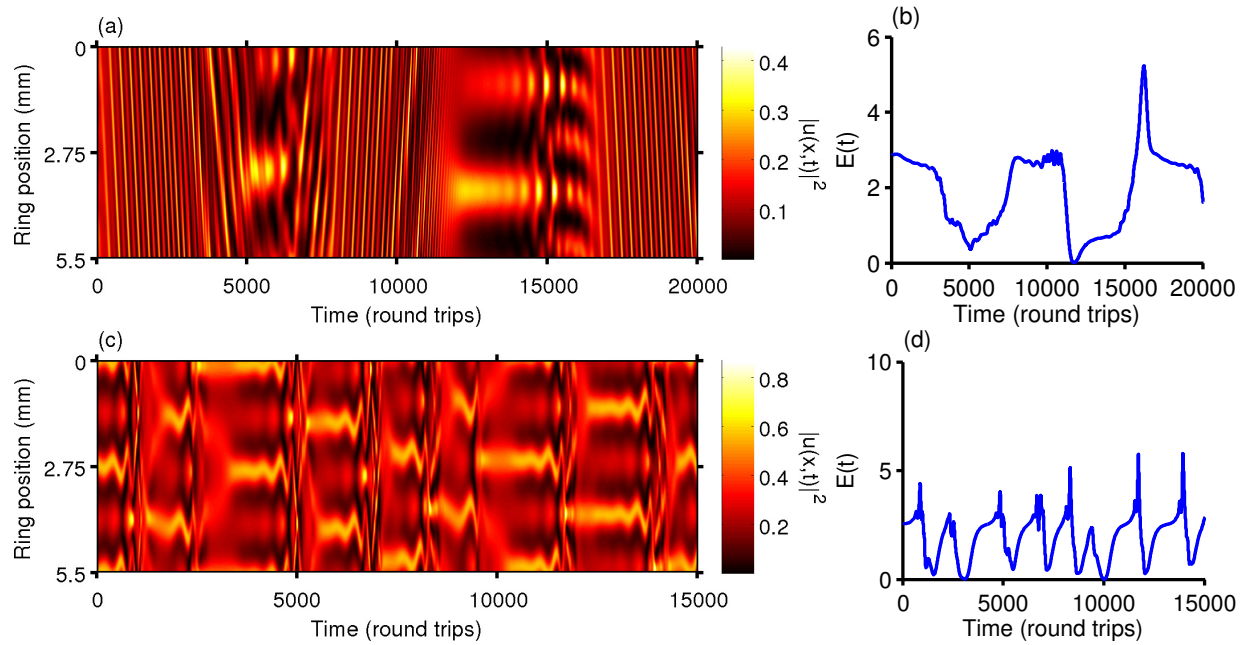
Figure 5.11: Two examples of intermittent solutions, both exhibiting characteristic aperiodic evolution between regions of well behaved dynamics. Panel (a) shows a solution with stable regions of multi-peaked solitary waves, while panel (b) has periods of 4 peak co-propagation.

solitary wave regimes separated by two aperiodic regimes exhibiting splitting, modulation and co-propagation behaviors. The energy is shown in plot (b) and was relatively constant during each of the multi-solitary wave regimes. The aperiodic regimes demonstrate significantly lower energy than the finite lifetime multi-solitary wave excitations. Panel (c) shows a simulation which exhibits periods of complex four solitary wave co-propagation interspersed with periods of aperiodic dynamics. The lengths of successive periods of dynamical behavior are highly variable and sensitive to both parameter choice and initial condition. This sensitivity makes numerical convergence difficult to demonstrate, as discussed below in Section 5.9.

5.9 Numerical Convergence and Quantitative vs. Qualitative Robustness

Simulations used well established and understood algorithms, fifth order adaptive Cash-Karp Runge-Kutta in time and pseudospectral methods in space [50, 51]. Detailed evaluation of psuedospectral methods for similar nonlinear equations may be found in reference [51].
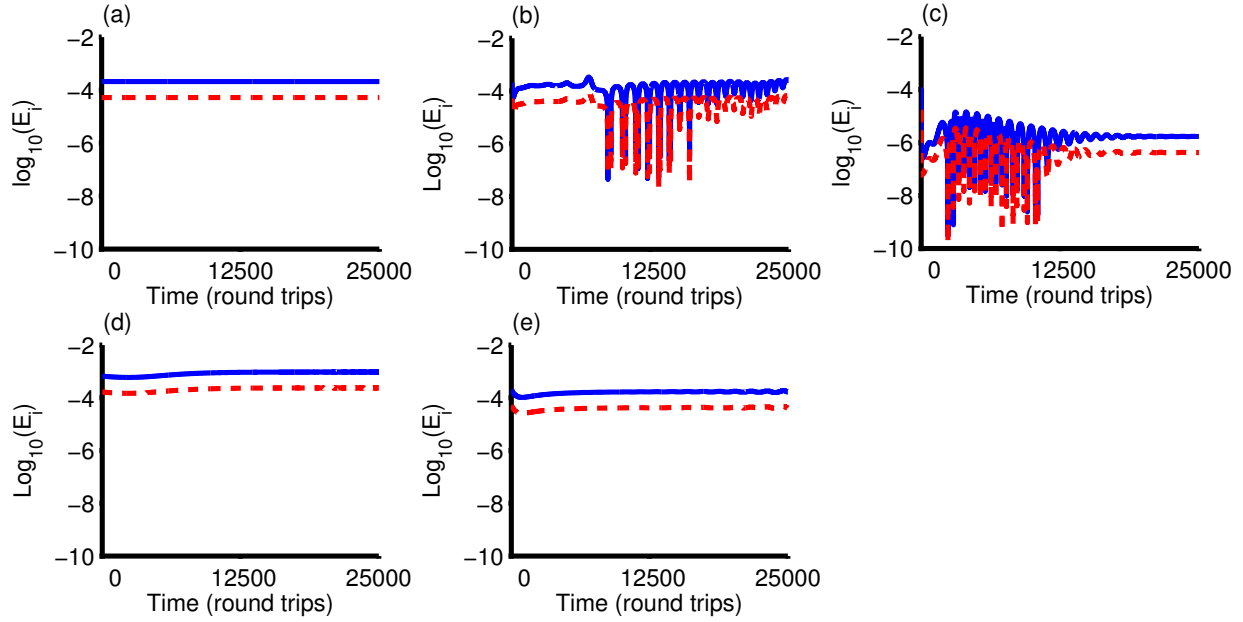
Figure 5.12: Relative differences in energy over 25000 round trips for increased spatial resolutions: 256 to 512 (512 to 1024) in solid blue (dashed red) line. (a) Bright soliton initial condition. (b) Solitary wave breathers. (c) Multi-peaked soliton. (d) Co-propagation. (e) complex co-propagation.

Simulations were run with a spatial grid of 256 and a single step truncation error of 10^{-12}. The maximum number of time steps performed in a single simulation was 10^8. Initial conditions were generated using imaginary time propagation and a single step truncation error of 10^{-18}. Stability of initial conditions was confirmed via real time propagation. To machine precision all initial states exhibit zero change in energy when propagated in real time for 10^9 steps. Initial conditions for different spatial resolutions have fixed differences in energy owning to discretization. This discretization error decreases exponentially for increasing spatial resolution: $|E_{256} - E_{512}| = 10^{-7}$, $|E_{512} - E_{1024}| = 10^{-8}$ and $|E_{1024} - E_{2046}| = 10^{-9}$. Results for each solution class were compared across grid sizes of 512 and 1024 and a single step truncation error of 10^{-18} to verify numerical convergence for algorithms used for both space and time propagation. We present convergence data for two distinct groupings of solution classes, those which exhibit extreme sensitivity to initial conditions and those which do not. The former demonstrate a qualitative robustness, while the latter are quantitatively robust.

Convergence can be demonstrated by relative difference. Given two sets, $\{x_n\}$ and $\{y_n\}$, of data consisting of N directly comparable observations then the relative difference at the ith entry is defined as

$$E_i = \left| \frac{x_i - y_i}{x_i} \right|. \tag{5.8}$$

This quantity offers a simple, unitless measure of the relative difference between two quantities.

5.9.1 Quantitative Robustness

Solution classes which did not demonstrate a marked sensitivity to initial conditions were numerically converged in a traditional manner. A distinct measurable, in this case energy, is quantitatively compared across successive time steps under different spatial and temporal resolutions. Convergence data is graphically displayed in Figure 5.12 for the initial condition used during simulations, Figure 5.12(a), as well as four categorical behaviors, panels (b)-(e). In each case the solid blue line compares spatial resolutions of 256 and 512 grid points, while the dashed red line compares the spatial resolutions of 512 and 1024 grid points. Figure 5.12(a) shows the fixed discretization error discussed previously in Section 5.9 while Figure 5.12(b)-(e) demonstrate the spatial convergence of each dynamical behavior over the entire evolution period is as good or better than that of the initial conditions. The greatest observed single time step relative spatial resolution error was $10^{-3}\%$. The greatest observed single time step relative temporal resolution difference was $10^{-8}\%$. The solution types listed here were quantitatively converged:

- Complex co-propagation

- Spatial shifting

- Breathers

- Multipeaked solitary waves

• Co-propagating solitary waves

5.9.2 Qualitative Robustness

A subset of observed dynamical behaviors, from both the temporally stable and intermittent categories discussed in sections 5.4-5.8, demonstrate an extreme sensitivity to initial conditions. These solutions were robust to variations in initial conditions and parameters of at least 10% in the sense that such perturbations did not yield a shift in their categorization. However, changes in initial energy or in loss parameters of the order 10^{-9} and lower resulted in distinct dynamics within that categorical behavior and shifts in the starting and ending times. We note shifts in spatial resolution introduce variations of this order to the relaxed initial condition. Therefore solutions exhibiting this sensitivity may not be converged numerically in the traditional sense.

An illustrative example is given by the asymmetrical interaction behavior, discussed in Section 5.5.2, after spatial symmetry about the feedback ring center has broken. Figure 5.13(a)-(c) depicts scaled intensity across the same 2500 round trips for three different choices of spatial resolution: 256, 512 and 1024 spatial grid points respectively. The behaviors across the three spatial resolutions are qualitatively similar with each exhibiting an asymmetric N_s solitary wave interaction which is characteristic of the solution type. However, the detailed dynamical behaviors of each case are quantitatively different. Further, as shown graphically in Figure 5.13(d), the three solutions have energies which vary by less than 0.32%. The behaviors listed below all demonstrated sensitivity similar to that discussed here with a relative energy difference no greater than 0.1%:

• Symmetric interaction

• Asymmetric interaction

• Chaotic Modulation

• Central Peak Recombination
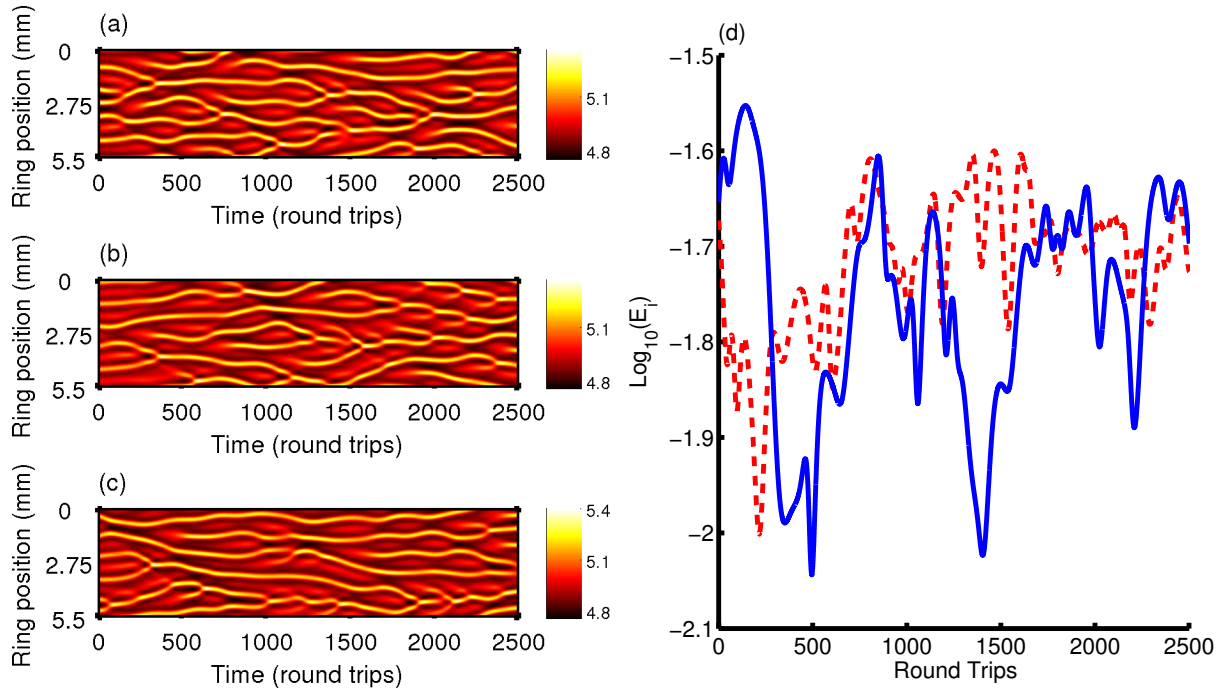
Figure 5.13: Convergence of the asymmetric interaction solution type. (a)-(c) A spatiotemporal plot of solution intensity for the same 2500 round trips for spatial resolutions of 256, 512 and 1,024 spatial grid points demonstrating stability of solution class and marked sensitivity to initial conditions. (d) Relative difference or in energy for the same round trips for 256 to 512 (512 to 1024) in solid blue (dashed red) line. Despite changes in initial conditions yielding markedly different dynamics within the solution class energies differ by less than 0.03%.

This sensitivity is a typical property of evolution towards and around a strange attractor. Major attempts were made to quantify the dimensionality of the attractor as discussed in Section 5.4 by the authors. No stable correlation dimensions were located for any of the complex dynamical behaviors which demonstrated sensitivity to initial conditions, excluding chaotic envelope modulation. A Lyapunov exponent was estimated for the asymmetric interaction case, see Section 5.5.2. Further quantification and exploration of the phase space properties of GLNLS solution types and the GLNLS itself are warranted.

5.9.3 Unstable

Any simulation which evolved into a trivial result, degraded to noise, blew up or decayed to zero is considered to be unstable. Approximately 30% of studied simulations are unstable.

90

This is not surprising as the explored parameter space includes cases when either gain (or loss) dominate the dynamics by orders of magnitude. A subset of simulations are observed to degrade into noise due to spatial resolution issues. Pseudo-spectral methods rely on discrete fast Fourier transforms (dFFT) which provide excellent convergence for well-behaved curves. However, if the spatial features of $u(x,t)$, the complex spin wave amplitude, approach the length of the numerical lattice spacing singularities may appear and the dFFT algorithms will no longer converge locally. These errors will continue to grow and propagate over time in an $L, Q > 0$ evolution. Further exploration of these cases with finer spatial resolutions is prohibited by computational resource constraints. In contrast, all results previously presented in sections 5.4-5.7 are converged in both space and time, as demonstrated in Section 5.9.1 and 5.9.2.

5.10   Chapter Conclusions

We report the numerical identification of nine distinct long lifetime complex dynamical behaviors as part of six broad solution classes of the gain-loss nonlinear Schrödinger equation (GLNLS), Equation 5.1. Behaviors were located during an extensive numerical exploration of six dimensional parameter space. A minimum of eight decades were examined for each gain term while five decades of higher order nonlinearities were considered at fixed dispersion and cubic nonlinearity. The GLNLS served as a driven damped model of long lifetime spin wave dynamics in magnetic thin film active feedback rings and analogous driven damped nonlinear physical systems. Agreement of GLNLS low dimensional chaotic modulating bright soliton trains with experimental measurements [31] was discussed in detail. We predicted additional GLNLS dynamical behaviors including two distinct steady state solutions, four unique examples of stable dynamical pattern formation and the intricate spatially symmetric/asymmetric interactions of solitary wave peaks. Finally we reported the existence of intermittent regimes within GLNLS parameter space, a phenomena typical of chaotic dynamical systems. Two unique examples of intermittency were presented which demonstrated finite periods of two distinct dynamical behaviors. The variety of presented GLNLS solution types matches the

scope of dynamical behaviors observed experimentally in YIG film spin wave systems, as well as predicting new behaviors that can be tested in present experiments. The GLNLS thus presents a simple yet viable and fundamental model for driven, damped nonlinear waves propagating in dispersive mediums.

We neglected the periodic effect of amplification within the feedback ring, so the gain and loss terms presented in this work represented averaged quantities. Highly variable solution types such as the symmetric and asymmetric interactions potentially violate the GLNLS operating regime, with gain and loss driven dynamics occurring on the scale of a single round trip. Future studies of this limit, adiabatically driven soliton trains and transient dynamics are warranted. A fine grained exploration of parameter space may also be justified to identify distinct domains of stability for each observed behavior. In the future a rigorous study of GLNLS phase space would be useful to determine the cause of intermittency and potentially locate chaotic attractors of higher dimension.

CHAPTER 6

PHYSICAL REALIZATION OF COMPLEX DYNAMICAL PATTERN FORMATION IN MAGNETIC ACTIVE FEEDBACK RINGS

This chapter contains a manuscript in its entirety which has been submitted to Physical Review X and is under revierw and contains work conceived and executed by myself with experimental help from Diego A. Alcala and P. A. Praveen Janatha. This work was conducted under the advisement of Lincoln. D. Carr and Mingzong Wu.

Associated reference [33]: Justin Q. Anderson, P. A. Praveen Janantha, Diego A. Alcala, Wu Mingzhong, and Lincoln D. Carr. Physical realization of complex dynamical pattern formation in magnetic active feedback rings. *Physical Review X [submitted]*, 2020. Preprint on arXiv: 2003.10541.

6.1 Abstract

We report the clean experimental realization of cubic-quintic complex Ginzburg-Landau physics in a single driven, damped system. Four numerically predicted categories of complex dynamical behavior and pattern formation are identified for bright and dark solitary waves propagating around an active magnetic thin film-based feedback ring: (1) periodic breathing; (2) complex recurrence; (3) spontaneous spatial shifting; and (4) intermittency. These nontransient, long lifetime behaviors are observed in microwave spin wave envelopes circulating within a dispersive, nonlinear yttrium iron garnet waveguide operating in a ring geometry where the net losses are directly compensated for via linear amplification on each round trip $\mathcal{O}(100\,\text{ns})$. The behaviors exhibit periods ranging from tens to thousands of round trip times $\mathcal{O}(\mu\text{s})$ and are stable for 1000s of periods $\mathcal{O}(\text{ms})$. We present 10 observations of these dynamical behaviors which span the experimentally accessible ranges of attractive cubic nonlinearity, dispersion, and external field strength that support the self-generation of backward volume spin waves in a four-wave-mixing dominant regime. Three-wave splitting

is not explicitly forbidden and is treated as an additional source of nonlinear losses. These long lifetime behaviors of bright solitary waves span the categories of dynamical behavior previously numerically predicted to be observable and represent a complete experimental verification of the cubic-quintic complex Ginzburg-Landau equation as a model for the study of fundamental, complex nonlinear dynamics for driven, damped waves evolving in nonlinear, dispersive systems. These observed behaviors are persistent over long times and robust over wide parameter regimes, making them very promising for technological applications. The dynamical pattern formation of self-generated dark solitary waves in attractive nonlinearity, however, is entirely novel and is reported for both the periodic breather and complex recurrence behaviors. All behaviors are identified in the group velocity co-moving frame. For (1) periodic breathing, we find that four or fewer bright or dark solitary waves may exhibit breathing with stable periods ranging from tens to hundreds of round trip times. The location of the solitary waves within the ring are seen to shift predictably while maintaining both peak solitary wave amplitudes and widths. For (2) complex recurrence, we find the periodic recurrence of interactions of three or more bright or dark solitary wave peaks is observed with stable recurrence times varying from hundreds to tens of thousands of round trips. For (3) spontaneous spatial shifting, we find spontaneous relocation of otherwise stable underlying ring dynamics is characterized by the instantaneous shift in location, in the group velocity frame, of the solitary waves while maintaining all other characteristics of the behavior. The time between shifts is unpredictable. Finally, for (4) intermittency, the dynamical behavior observed within the feedback ring shifts between two or more stable underlying behaviors unpredictably, indicating the presence of two or more overlapping attractors within the system.

6.2 Introduction and Motivation

Spin wave envelope (SWE) solitary waves in active magnetic thin film-based feedback rings (AFRs) have proven to be an effective sandbox for the exploration of fundamental nonlinear dynamics. Over the past two decades a rich variety of complex dynamical be-

94

haviors have been observed in dissipative SWE solitary waves propagating in these nonlinear, dispersive feedback rings. Examples include bright and dark solitary waves and wave trains [4, 5, 7, 20], möbius solitons [22], Fermi-Pasta-Ulam and spatial recurrences [23, 24], chaotic solitary waves [31, 32], and random solitons [26, 105].

AFRs are a notably useful system for the study of dissipative, nonlinear, dispersive wave dynamics for a few fundamental reasons. First, the active feedback allows for the compensation, on average, of the losses that the SWE solitary waves experience during propagation. Such quasi-conservative evolution allows for the observation of dynamical behaviors which can persist for tens of thousands, or more, of the fundamental round trip time $\mathcal{O}(100 \text{ ns})$. The experimental realization of such long life time, $\mathcal{O}(\text{ms})$, dynamics is in fact in line with the original goals of solitary wave research which focused on the viability of solitons as the basis for long-distance high-bandwidth optical communication [48, 49, 106]. Research efforts in this area slowed in the mid 2000s as dispersion-managed solitary waves were ultimately abandoned in favor of multiplexing schemes which provided cheaper scalability. The varied ecology of long lifetime dynamical behaviors present in these systems and the accessibility of chaotic regimes, however, continues to make solitary waves an intriguing candidate for lower bandwidth secure communication [107].

Second, the feedback ring geometry imposes a phase constraint in the form of a ring resonance. Geometries of this type are common within the optics, electromagnetic device and magnonics communities [108–111]. Active research topics include optical solitary waves produced in micro-ring resonators [112]. These solitary waves are used as a source of broadband (octave spanning) frequency combs for coherent parallel communication. The dynamics of dissipative optical solitary waves within micro-ring resonators is also being investigated [113–116]. Spin wave AFRs are additionally studied as delay lines for reservoir computing [117–119].

Third, the dispersion and nonlinearity characteristics of SWEs in AFRs are highly tunable via two easily accessible experimental parameters: external field orientation and ampli-

tude [2, 36, 41]. By adjusting these parameters one can vary the nonlinearity from three-wave mixing to four-wave (Kerr) mixing and from attractive to repulsive. The sign and amplitude of dispersion may also be manipulated this way. This allows for the study of both dark and bright solitary waves dynamics in a single system.

Fourth, SWEs in AFRs are described by the cubic-quintic complex Ginzburg-Landau equation (CQCGL), which in its nondimensionalized form, see Equation 6.2, is a generalized nonlinear Schrödinger equation [36]. Various forms of the nonlinear Schrödinger equation appear as governing models across a wide variety of physical systems. This includes the Lugiato-Lefever equation which describes lasers in nonlinear cavities [120], the Gross-Pitaevskii equation for modeling the mean field of atomic and molecular Bose-Einstein condensates [39, 40], and the Ginzburg-Landau equation which is used to describe superconductivity and the evolution of mode-locked laser envelopes [35, 95]. Driven, damped nonlinear Schrödinger equations are additionally used to model deep water waves [1] as well as magnon and exciton-polariton Bose-Einstein condensation [38]. The physics which are accessible using SWEs in AFRs are then, up to the nontrivial issues of units, scaling, complex potential and naming conventions, applicable to many physical systems which are described by this important family of isomorphic partial differential equations. AFRs in fact provide an accessible tabletop experiment from which one can study complex nonlinear wave physics across many scales for driven, damped systems.

In this article we present the clean experimental realization of nontransient, long lifetime (10,000s of round trips) complex dynamical behaviors for SWE bright and dark solitary waves propagating within in an AFR. These results are distinct from the study of dissipative solitons in the above mentioned systems where focus has generally remained on exploring transient behaviors, periodic modulations and isolating extreme events [121–124]. The behaviors described here were previously predicted to be observable by a numerical parameter space search which identified four distinct long lifetime examples of dynamical pattern formation in bright solitary waves described by the CQCGL [34]. We emphasize that

these numerical predictions involved an extraordinarily broad parameter space search which spanned a minimum of *five orders of magnitude* for four distinct parameters (S, L, C and Q in Equation 6.2). Across that parameter space only four categories of long lifetime dynamical pattern formation were predicted. We report on the observation of all four of these behaviors for bright solitary waves and the first known realization of self-generation and dynamical pattern formation for dark solitary waves evolving under attractive nonlinearity.

These behaviors are promising for potential technological applications due to their persistently long lifetimes and robustness over wide parameter regimes. One likely application is classical benchmarking for quantum simulator experiments, for example Sagnac interferometers in BECs [125]. Such devices have been explored in both attractive and repulsive nonlinearity regimes, but a lack of understanding of the attractive case [126–128] has prevented the field from moving forward technologically.

The observed dynamical behaviors are as follows. (1) We observe *periodic breathing*, where solitary waves periodically relocate their position within the ring (in the group velocity frame). We present examples of one and two waves undergoing this periodic relocation for both bright and dark solitary waves. (2) We observe *complex recurrence*, where three or more solitary waves undergo periodic spatial recurrence involving multiple frequencies. Examples of complex recurrence are shown for both bright and dark solitary waves. (3) We observe *spontaneous spatial shifting*, where a stable behavior undergoes a sudden repositioning within the ring (in the group velocity frame) and then immediately continues its stable behavior. (4) Finally, we observe *intermittency*, where the system jumps between two distinct stable behaviors.

The paper is organized as follows. Section 6.3 discusses the active magnetic thin film-based feedback ring experiment; here the experimental apparatus and accessible physics will be detailed. Sections 6.4-6.8 focus on the key four behaviors as identified above: periodic breathers, complex recurrence, spontaneous spatial shifting and intermittency. Conclusions and outlooks are then provided in Section 6.9.

6.3   Experiment and Methods

This section details the construction of the active magnetic thin film-based feedback ring used to collect the data reported in this work as well as the basic physics of the spin waves which we can access with it. We start with a description of the AFR, its components and an overview of the merits and motivations behind the design of the experiment. We then explore the relevant spin wave physics to the experiment and the subsequent analysis presented in this work. Finally we discuss the experimental methods, procedure, and philosophy used to isolate the dynamics reported here.

6.3.1   Active Magnetic thin film-based feedback Rings

An active magnetic thin film-based feedback ring is constructed of two main components: (1) a yttrium iron garnet (Y3Fe5O12,YIG) thin film waveguide and (2) an electronic feedback loop. These components are coupled via two transducers, one each for the excitation and detection of spin waves within the YIG waveguide. The electronic loop is comprised of a fixed, linear amplifier and variable attenuator pair which allows for the direct compensation of the major loss mechanisms present within the thin film. An oscilloscope and spectrum analyzer are coupled to the electronic feedback loop via a directional coupler for in-situ observation and recording of time-domain and frequency-domain ring signals. An AFR is schematically shown in Figure 6.1 detailing the construction of the electronic feedback loop and the thin film waveguide. Figure 6.1 shows an external magnetic field applied parallel to the waveguide. This orientation enables the generation of backward volume spin waves (BVSW), the type of spin wave which is the main focus of this work. BVSWs will be discussed in detail in Section 6.3.2, and any further mention of spin waves in this work will refer to BVSWs unless explicitly stated otherwise.

As mentioned in Section 6.2 the active feedback component of AFRs allows for the study of spin waves in a quasi-conservative regime, which can support behaviors with lifetimes of tens or hundreds of thousands of the fundamental round trip time, $\mathcal{O}(100 \text{ ns})$. The
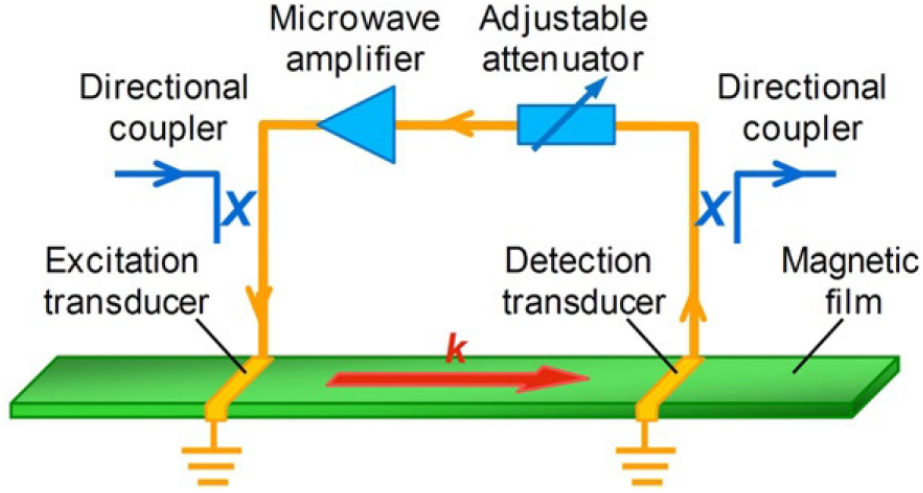
Figure 6.1: Diagram of an active magnetic thin film-based feedback ring. A spin wave feedback ring constructed of a nonlinear, dispersive waveguide (the YIG film) coupled to an electronic feedback loop via two transducers. The ring has a linear, fixed amplifier and a variable attenuator. Observation equipment is attached via a directional coupler. Reprinted with permission from Elsevier [41].

periodic amplification also enables the self-generation of SWE solitary waves. Self-generation is achieved by increasing the ring gain (through a decrease in attenuation) until the lowest loss ring eigenmode begins to circulate. The ring eigenmodes are given by the phase condition

$$k_n(\omega)L + \phi_e = 2\pi n, \quad n = 1, 2, 3..., \tag{6.1}$$

where $k_n(\omega)$ is the wavenumber of the nth eigenmode, L is the separation between the excitation and detection transducers and ϕ_e is a phase delay caused by the signal's propagation through the electronic feedback loop. Typically $\phi_e \ll k_n(\omega)L$. As the ring gain is increased additional eigenmodes begin to circulate and their amplitudes increase until these modes begin to interact nonlinearly through three and four-wave mixing processes (to be discussed in Section 6.3.2). The number of eigenmodes present during a typical experiment is less than 10, though at higher ring gains up to a few hundred may circulate. All the solitary waves presented in this work are self-generated. Adjustments to the attenuator are done manually and occur on the order of seconds. This means all changes in ring gain occur over tens or

hundreds of thousands of round trips and are adiabatic on that scale. Since no additional microwave signals are introduced into the ring from an outside source, all behaviors recorded from self-generated SWE solitary waves in AFRs have existed for at least $\mathcal{O}(10^5)$ round trips and may be regarded as being in dynamic equilibrium. Transient behaviors are therefore not studied during self-generation. We note that transient effects can be highly relevant to applications such as communication, but they are not considered in this work.

Several other design features of the AFR warrant further discussions. First, YIG thin films are used as a propagation medium owing to their extraordinarily low loss characteristics at microwave frequencies [41]. These low losses, typically 3 orders lower than alternative waveguide materials, support propagation distances on the order of centimeters and therefore enable long excitation lifetimes. Long lifetimes maximize the interactions between nonlinearity, dispersion and losses on ring dynamics. Amplitude dependent nonlinearities and losses will have maximum relative influence on wave evolution close to the excitation transducer where spin wave power is at its highest. Dispersion and lower order effects will have higher relative influences the longer the spin wave propagates through the medium.

Second, an external magnetic field is applied to magnetize the YIG thin film to saturation and thereby enable the excitation of spin waves. The direction and amplitude of this field allows for the tuning of nonlinearity and dispersion and will be further discussed in Section 6.3.2.

Third, all observation equipment is attached to the feedback ring via a directional coupler. This eliminates the interference of observation on ring dynamics. Observation may instead be treated as a fixed, linear attenuation within the AFR.

Fourth, the signal is fed into the oscilloscope through a microwave diode with quadratic behavior. Thus, all recorded voltage data are taken to be proportional to power. The diode further allows for sampling of ring voltage at lower frequencies. This is because data recorded through the diode corresponds directly to the spin wave envelope, our principle interest, rather than the underlying carrier wave. These slower sampling rates of $\mathcal{O}(1 \text{ Gsamp/s})$ as

opposed to $\mathcal{O}(10 \text{ Gsamp/s})$ support the collection of longer time series which is crucial to the identification of dynamical behaviors which occur over hundreds or thousands of round trips. We do note that the reconstruction of phase is not possible without fully resolving the underlying carrier wave. Both high and lower frequency sampling can be conducted simultaneously using a splitter, however this comes at a significant cost of signal-to-noise ratio. This would be particularly harmful during the work presented here which maximizes spin wave propagation distances and thereby minimize power at the detection transducer.

Fifth, the physical length of the YIG film is much greater than the propagation length L between the transducers. The ends of the film are additionally cut at 45 degree angles. These considerations eliminate end reflections from reaching transducers and thereby impacting ring dynamics.

Sixth, we use two-element U-shaped antennas as transducers for the excitation and detection of spin waves within the film. These two-element antennas function as spectral filters by reducing the passband in the AFR. The upper edge of the passband is not effected, however the lower bound now corresponds to the destructive interference condition where the frequency in each of the elements is out of phase by π. The use of two-element antennas generally results in a smoother, more linear passband and can limit the spectral distances between ring eigenmodes at higher AFR gains [9, 129]. Long lifetime dynamics of SWE solitary waves can more readily be isolated and identified when the range over which the ring gain can be manipulated without introducing spin wave dynamics from vastly differing eigenmode frequencies (and therefore group velocities) into the ring is maximized. This type of filtering is a choice of convenience and experimental expediency, and is not necessary for the generation of dynamics reported in this work. The transducers used in this experiment are 50 μm wide and 2 mm long with a separation distance between the elements of 60 μm. The maximum wavenumber excited by this transducer is given by $k_{\mathrm{max}} = 2\pi/\mathrm{d}$ and here d is the separation between the elements giving $k_{\mathrm{max}} = \mathcal{O}(10^3 \text{ rad/cm})$. Note the wavenumber of the lowest loss eigenmode is typically near 100 rad/cm.

Finally, the variable attenuator and fixed amplifier pair have a linear response in the frequency and power ranges used in the experiment.

6.3.2   Spin Waves in Magnetic Thin Films

As discussed above, an AFR with these components and design considerations supports the self-generation of backward volume spin wave envelope solitary waves [41]. This is the AFR configuration which has generated a majority of the previously observed dynamics discussed above. BVSWs may be self-generated in an AFR where the propagation medium has been placed in an external magnetic field that is applied parallel to the film, as shown in Figure 6.1. BVSWs are so called due to their negative group velocity. They have positive dispersion, D, and negative nonlinearity, N, coefficients. The opposite signs of dispersion and nonlinearity indicate the effects of one may compensate the effects of the other. This type of nonlinearity is called attractive, or self-focusing, and supports the generation of bright solitary waves, see Equation 6.4 below.

The signs and amplitudes of the nonlinearity and dispersion are easily tunable for spin waves propagating in magnetic thin films. This tunability is achieved primarily by rotating the external field relative to the film. For example, forward volume spin waves may be excited by applying the external magnetic field normal to the thin film. This type of excitation also exhibits attractive nonlinearity, but contrary to BVSWs these waves have a positive group velocity, a negative dispersion, and a positive nonlinearity. Surface spin waves may be excited by placing the external field normal to the vector of propagation (or normal and in-plane with the external field shown in Figure 6.1). Surface spin waves have repulsive nonlinearity, with both the dispersion and nonlinearity coefficients being negative. This type of nonlinearity supports the propagation of dark solitary waves, see Equation 6.5 below. The sign and magnitude of dispersion may also be adjusted by choosing operating points on either side of dispersion gaps for pinned surface waves [20]. Again, only the BVSW regime is considered in this work, but interested readers are directed to these references for further information [2, 13, 18, 41, 130]. We note there is also ongoing research into exciting multiple

spin wave regimes at once [131].

Nonlinearity and dispersion coefficients for spin waves in nonlinear thin films are defined in terms of the dispersion relation, $\omega(k)$ as

$$D = \frac{\partial^2 \omega(k)}{\partial k^2},$$

$$N = \frac{\partial \omega(k)}{\partial |u|^2},$$

where u is a dimensionless spin wave amplitude. These expressions for nonlinearity and dispersion are results of deriving the governing equation of spin waves in thin films via a slowly varying envelope approximation on the nonlinear dispersion relation, $f(\omega, k, |u|)$ [2]. The resulting equation is,

$$i\frac{\partial u}{\partial t} = \left[-\frac{D}{2}\frac{\partial^2}{\partial x^2} + N|u|^2 + V(x, t, u) \right] u \tag{6.2}$$

and when the potential V is set to zero we have a dimensionless form of the nonlinear Schrödinger equation.

Higher order nonlinearity may be naturally included by keeping more terms of the expansion of the dispersion relation. Losses are introduced phenomenologically. If cubic and quintic terms are kept then one arrives at the CQCGL equation where the potential is of the form

$$V(x, t, u) = iL + iC|u|^2 + (S + iQ)|u|^4, \tag{6.3}$$

here L, C and Q are linear, cubic and quintic loss coefficients and S is a quintic nonlinearity coefficient. All parameters are taken to be real with i's explicitly stated, except the spin wave amplitude u which is a complex scalar field. The inclusion of at least quintic terms is necessary to model saturable losses that are experimentally observed in self-generated spin waves which evolve under either three or four-wave mixing [28, 103]. Saturable losses are also studied in dissipative optical solitons [89, 95]. Nonlinear Schrödinger governing equations for spin waves in nonlinear thin films may also be rigorously derived through a Hamiltonian formalism [3].

When four-wave mixing, discussed below, is the dominant source of nonlinearity and losses are negligible (or $V=0$) the ground state solitary solution to the nonlinear Schrödinger equation may be reached via an inverse scattering transform [132]. For the case of attractive nonlinearity ($ND < 0$) the ground state solution is the standard bright soliton given by

$$u(z,t) = \mu_0 \operatorname{sech}\left[\mu_0\sqrt{\frac{-N}{D}}\,(z - v_s t)\right],\tag{6.4}$$

where the phase is given by

$$\begin{aligned}
\phi(z,t) &= \exp i[k_s z - \omega_s t]\\
v_s &= v_g + k_s D\\
\omega_s &= v_g k_s + \frac{1}{2}D k_s^2 + \frac{1}{2}N\mu_0^2
\end{aligned}$$

with $u(z,t) = |u(z,t)| \exp(i\phi(z,t))$. We highlight that for the bright soliton the phase is constant over the soliton peak and there is no phase difference at $(z - v_s) \to \pm\infty$. The hyperbolic secant shape and the phase characteristics across the peak are common identifiers of bright solitary waves.

Dark solitary waves are the ground state solution for repulsive nonlinearity ($ND > 0$) and are given by

$$|u(z,t)| = \mu_0\left[1 - \operatorname{sech}^2\left(\mu_0\sqrt{\frac{N}{D}}\,[z - v_s t]\right)\right],\tag{6.5}$$

and the phase across the soliton peak is

$$\phi(z,t) = \arctan\left[\tanh\left(\mu_0\sqrt{\frac{N}{D}}\,[z - v_g t]\right)\right]\tag{6.6}$$

Dark solitons are notches in the amplitude of a continuous wave background and possess a π shift across their dips. If the final depth of the notch does not reach zero then the soliton is called grey and the phase shift is less than π, somewhat modifying [133] the form given in equations 6.5 and 6.6. As with bright solitary waves the hyperbolic secant dip and the phase characteristics across the dip are common identifying features of dark and grey solitary waves. Note that there is a phase difference at $(z - v_s) \to \pm\infty$ for dark and grey

solitary waves. This means that if these waves are traveling within a ring there must always be a minimum of two to satisfy phase continuity conditions unless there is a background flow of $-\pi$ to cancel the phase jump [134]. Typically bright (dark) solitary waves do not exist outside of the attractive (repulsive) nonlinearity which supports them as a solution to the nonlinear Schrödinger equation. Any exceptions to this suggest the influence of higher order or other external effects [5]. As mentioned earlier, the sign of dispersion can also be control by exciting spin waves on either side of a a dipole gap in a film with pinned surface waves, thus modifying of the effective nonlinearity, ND, and enabling the excitation of dark solitary waves [20]. Similarly an external periodic potential can also be applied to generate negative mass and thus flip the sign of dispersion. It has also been demonstrated that dark solitary waves may be observed in spin wave systems with attractive nonlinearity if one injects carefully tuned carrier wave signals [5]. However, implementing a periodic potential is impractical in many contexts including fiber optics, and the long lifetime dynamics presented here are not observable when carrier wave signals are fed into a short film with no active feedback.

There are two types of nonlinearity which affect spin waves in YIG waveguides: the nonconservative three-wave splitting or confluence processes, and the conservative four-wave mixing process [2, 41, 130] (known as three and four-magnon scattering in quantum mechanics). The bright and dark solitary wave solutions above and the solitary wave dynamical behaviors presented below are principally products of four-wave mixing. During the self-generation of spin waves in an AFR if two or more eigenmodes are circulating the ring with sufficient amplitude they interact via four-wave mixing to generate a third mode (ω_3) with the following frequency and wavenumber

$$
\begin{aligned}
2\omega_1 &= \omega_2 + \omega_3\,, \\
2k_1 &= k_2 + k_3\,.
\end{aligned}
$$
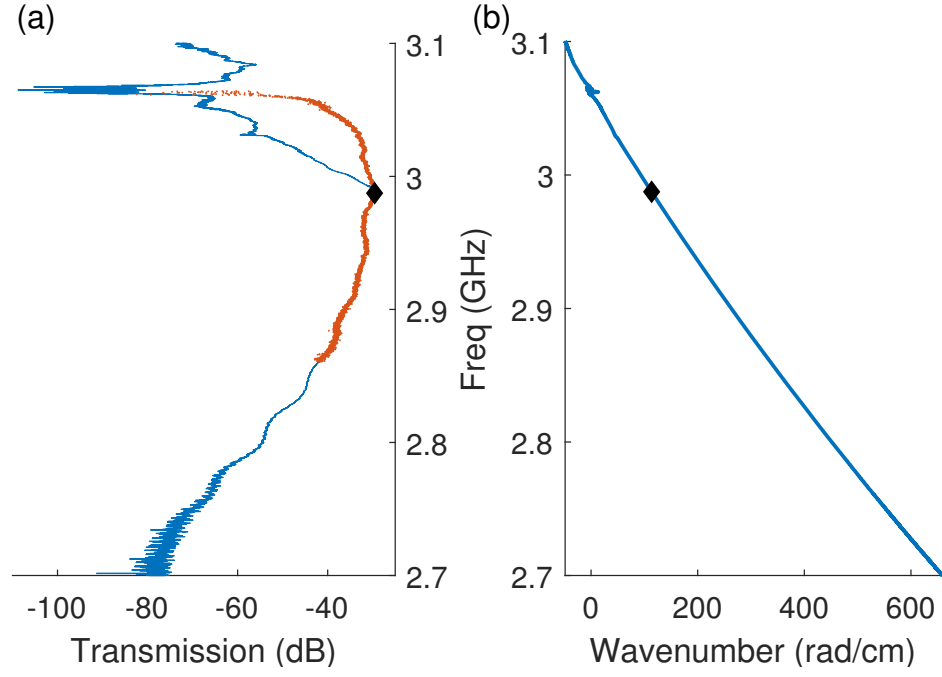
Figure 6.2: Yttrium iron garnet transmission profiles (a) Transmission loss and (b) wavenumber vs frequency profiles for a transducer-YIG thin film-transducer structure with parallel external magnetization. The red and blue curves in (a) were measured at input powers P_{in}=-24 dBm and 4 dBm, respectively. Additional transmission losses at high power indicate three-wave mixing. The lowest loss ring eigenmode is shown as a black diamond at 2.987 GHz and corresponds to a wavenumber of $k \approx 114$ rad/cm.

As power is further increased additional modes will be generated through this four-wave process, ultimately resulting in a uniform frequency comb with spacing $f_{\rm s} = |\omega_1 - \omega_2|$. These equispaced frequency combs are a spectral signature of bright and dark solitary waves and importantly cannot be generated simply through exciting additional ring modes owing to the spin wave nonlinear dispersion relation. An experimentally measured dispersion curve can be seen in Figure 6.2(b), where the $k = 0$ point corresponds to the uniform mode or the ferromagnetic resonance in the YIG thin film. The lowest loss eigenmode at 2.987 GHz is shown as a black diamond and corresponds to a wavenumber of $k \approx 114$ cm/ns. This data was recorded at an external field strength of 496 Oe.

The three-wave splitting and confluence processes involve the splitting of one mode (ω_0) into two new half-frequency modes, or the combination of two half-frequency modes into a new mode (ω_3) and is inherently nonconservative. The splitting and confluence processes are given by

$$
\begin{aligned}
\omega_0 &= \omega_1 + \omega_2, \\
k_0 &= k_1 + k_2,
\end{aligned}
$$

and

$$
\begin{aligned}
\omega_1 + \omega_2 &= \omega_3, \\
k_1 + k_2 &= k_3,
\end{aligned}
$$

respectfully. For BVSWs the three-wave process can be viewed as a source of nonlinear loss where energy leaves the ring system by the splitting of self-generated ring eigenmodes, with wavenumbers of $\mathcal{O}(10$ rad/cm$)$, into two half frequency modes with wavenumbers of $\mathcal{O}(10^5$ rad/cm$)$ [28, 41]. These half frequency modes posses wavenumbers well beyond the maximum wavenumber capable of being excited or detected by the transducers used in this experiment, as explained above. Therefore the half modes do not circulate within the ring. Without the active feedback these modes decay into heat and there is no associated

confluence process to introduce power back into the higher frequency modes. Note, the major linear losses in YIG thin films result from magnon-phonon scattering, an intrinsic relaxation process, and from two-magnon scattering, an extrinsic relaxation process associated with film defects [2].

An experimental example of transmission loss through the transducer-YIG thin film-transducer structure (not including the feedback ring) is shown in Figure 6.2(a) with a high power (4 dBm) transmission loss curve shown in blue and a low power (-24 dBm) transmission loss shown in red. The loss caused by three-wave mixing is evident in the high power data above 2.99 GHz. This closely matches with theory that predicts the lower edge of the passband for BVSWs at 1.50 Ghz. Below 3 Ghz the three-wave splitting process is forbidden by conservation law. Note that at sufficiently high external field strengths, no half modes remain within the BVSW passband and the three-wave processes are entirely forbidden. For BVSWs this occurs when $\omega(0) = 3.27$ GHz or at an external field strength of about 600 Oe [13]. The general shape of the low power transmission loss plot in Figure 6.2(a) is typical. The transducers are generally less efficient for high-k modes, but this is directly counteracted by the increase in group velocity of BVSWs at higher frequencies. An increase in the group velocity decreases the round trip time, and thereby the overall losses. The result is a fairly flat transmission loss curve spanning approximately 400 wavenumbers with a minimum in the middle.

At lower external fields the loss from three-wave splitting will span more of the experimental passband. By 350 Oe the full passband will experience additional losses from three-wave splitting. In practice this results in a saturation in the power-out vs power-in response, or the addition of higher order loss. Note that it is well documented that BVSWs in AFRs experience a saturation in power-out vs power-in even when three-wave processes are forbidden, so three-wave mixing can be viewed as an additional, and stronger, source of nonlinear losses [28, 103].

The data presented here were gathered at four distinct operating frequencies across different choices of transducer separation. Spin waves were self-generated at 2.5 GHz, where the entire passband is subjected to additional nonlinear losses, at 3.0 GHz, where part of the passband experiences three-wave splitting such as in Figure 6.2(a), and at 3.5 GHz and 4.5 GHz where three-wave splitting is explicitly forbidden. In practice, actual operating points vary from these targets as external field strength and the location of the film on the transducers is varied to isolate clean dynamics. Higher frequency excitations were not explored in order to maximize the impact of ring losses on ring dynamics. We highlight that this work presents the first observations of self-generationed dark solitary waves under attractive nonlinearity, and the first example of long life time complex dynamical behaviors in dark solitary waves.

6.4   Periodic Breathers

Periodic breathing is a stable dynamical pattern characterized by the smooth, periodic amplitude modulation of SWE solitary waves matched with a simultaneous relocation of the wave positions within the feedback ring. Three features define this behavior. (1) The amplitude and direction of the location shift are constant. This amount is always proportional the number of solitary waves in the ring. For N solitary waves a full period is defined by $(N + 1)$ breaths with positional shifts of $2\pi/(N + 1)$ rad. (2) A minimum of one solitary wave must have its amplitude drop to the background during a full breathing period. This is necessary to draw a qualitative distinction between breathers and modulating solitary wave trains where higher order solitons exhibit periodic or chaotic amplitude modulation but without relocation [31, 41]. (3) The shift is not spontaneous but rather a smooth function of round trips which remains consistent across all observed breathing periods. To summarize, in scaled units, a periodic breathing SWE solitary wave oscillates between a magnitude of zero and one while relocating predictably within the ring.

Periodic breathing for both bright and dark solitary waves are presented for two typical examples of the behavior. (1) In periodic breathing solitary waves relocate at a single

fixed period. (2) In multi-periodic breathing the solitary waves breathe at two or more frequencies. We highlight, as mentioned in Section 6.3, that all data presented here were recorded on an AFR with a parallel external magnetic field. This film geometry enables the excitation of BVSWs with an attractive nonlinearity. The dark solitary wave dynamics reported here occur in a geometry which traditionally supports the generation of bright solitary waves via the compensation of dispersion with attractive nonlinearity and loss. The only experimental parameters changed between observations are external field strength, AFR gain and transducer separation. None of these parameters explicitly alter the sign of cubic nonlinearity operating within the film.

6.4.1 Bright Solitary Wave Periodic Breathing

Periodic breathing is epitomized by a single, bright solitary wave modulating at one, fixed frequency. In this representative case the behavior is easily observable and the consistency of the wave's predictable relocation within the ring is apparent. A typical example, recorded through a diode at an external field strength of 311 Oe with a 2.39 GHz carrier wave, is shown in Figure 6.3. The bright solitary wave breather is readily identifiable through its reconstructed spatiotemporal amplitude plot, given in Figure 6.3(a), where each vertical slice is a single round trip and we move through time (in the group velocity frame) from left to right. Scaled spin wave power is shown as shading. Here we see a bright solitary wave (with a scaled amplitude of one) centered in the ring which smoothly decreases in amplitude to zero prior to undergoing a π shift to the edge of the ring. The wave then breathes back to the center, completing a single period. The breathing process then repeats. The bright solitary wave profiles for a single round trip at the maximum peak amplitude of a center (dotted-blue) and edge (crossed-red) breath are plotted in Figure 6.3(b). Actual data is binned for clarity and lines are a guide for the eye. We highlight that the plots in Figure 6.3 correspond to solitary waves circulating within the AFR but have been shifted into a frame co-moving with the waves at their group velocity. This type of reconstructed spatiotemporal plot will be used extensively throughout this work to highlight long lifetime solitary wave
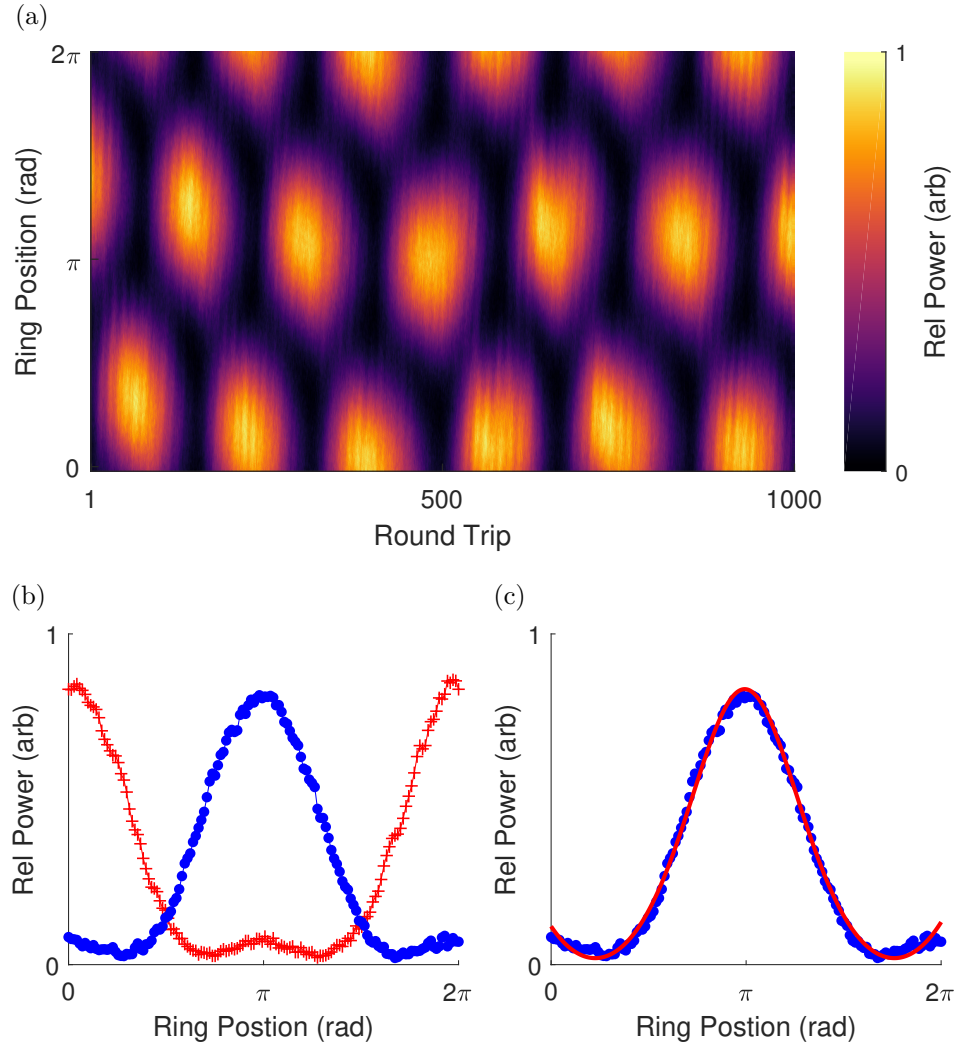
Figure 6.3: Spatiotemporal and single round trip plots of bright solitary wave periodic breathing The stable periodic breathing of one bright solitary wave from the center to the edge of the ring (π shift) is shown in the spatiotemporal plot (a) The bright solitary wave nature of the dynamic is shown in the scaled power vs. ring position plots (b) and (c). Plot (b) shows round trips with the peak in the center and edge of the ring as blue dots and red crosses, respectively. A fit to a Jacobi elliptic CN, a periodic generalization of the sech function [135], is shown in plot (c) with the peak centered in the ring as blue dots and the fit as a red line. Actual data is binned for clarity, and lines in (b) are a guide for the eye.

dynamics. Similarly through this work, unless stated otherwise, actual data is plotted and lines are a guide for the eye.
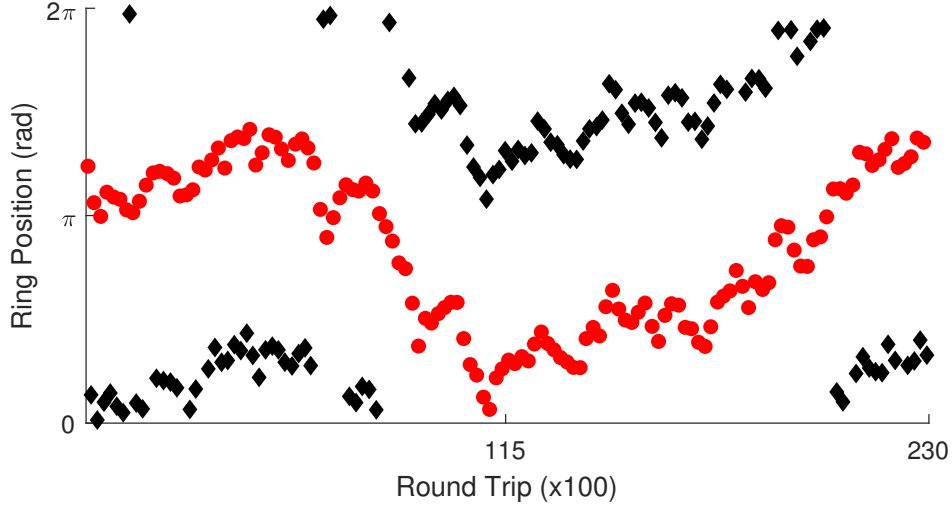
Figure 6.4: Peak locations of bright solitary wave breathing.*Bright solitary wave breathing.* Peak locations for central (red dots) and edge (black diamonds) breaths for a bright solitary wave undergoing stable periodic breathing.

A round trip time of 353.625 ns was identified visually by minimizing the change in the central breathing location over all observed breathing periods. A total of 8.2 ms of data was collected at 4 Gsamples/s yielding over 23,000 round trips of data. 1000 round trips are shown in Figure 6.3(a). This data was collected through a diode so, as discussed in Section 6.3, only the spin wave envelope was accurately captured. A peak finding algorithm was used to isolate 261 individual peak locations, or 130 full breathing periods. These peak locations are visualized in Figure 6.4 with the central peaks as red dots and the edge peaks as black diamonds. These locations were then used to generate profiles across round trips (temporal) and across ring position (spatial) for each of the peaks. A breathing period of 175.98 $\pm$ 17.68 round trips was identified from these statistics, suggesting 132 breathing periods were recorded. This is consistent with our peak finding algorithm where we ignored the first and last two breathing periods to ensure full temporal and spatial profiles could be isolated.

Some jitter in the group velocity is observed across the 23,000 round trips. The peaks can be seen drifting around the ring relative to their original positions. Using all 261 isolated

peaks the change in group velocity is found to be -7.95x10^{-7} ± 3.75x × 10^{-4} cm/ns per breathing period, or -1.28x10^{-13}±6.03×10^{-9} cm/ns^2. The group velocity jitter is determined to be normally distributed about this near-zero mean with an Anderson-Darling statistic of 0.270 (normality would be rejected at 0.750). Given a measured transducer separation of 1.233 ± 0.040 cm and a round trip time of 353.625 ns we can estimate the the group velocity as $-3.487 \times 10^{-3} \pm 1.1 \times 10^{-4}$ cm/ns. The jitter, then, amounts to at most an order 10% change in group velocity about the mean, or a total shift in ring location of less than 10%, over a single breathing period.
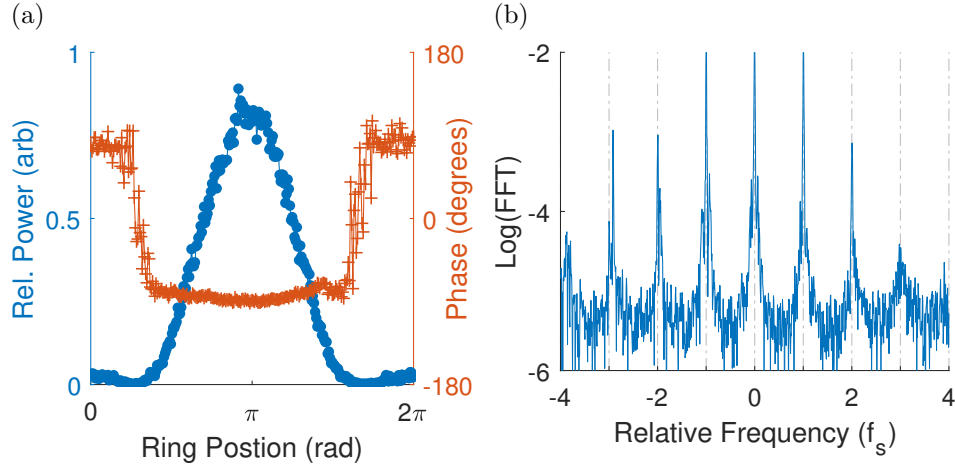
Figure 6.5: Reconstruced phase for bright solitary wave breathing. Reconstructed phase data which demonstrates the solitonic nature of the stable periodic breathing wave. (a) Ring power and reconstructed phase data in blue dots and red crosses, respectively. A flat phase across the peak profile is a defining characteristic of bright solitary waves. (b) Power spectrum around the principal carrier frequency and scaled by the comb spacing, f_s. An equi-spaced frequency comb generated via four-wave mixing is another defining feature of solitary waves.

The solitonic nature of the underlying wave is readily verified by the fit shown in Figure 6.3(c) for a single of the 262 identified peaks (chosen at random). Here actual data is plotted and the red line is a fit to the generalized bright soliton solution to the NLS given in 6.4. Each of the 261 identified peaks was fit using nonlinear least squares in order to generate goodness-of-fit statistics. The fits yielded a mean reduced χ^2 of 2.65±2.22, a mean adjusted r^2 of 0.994±0.008 and with a Jacobi-elliptic parameter [135], m, of 0.6862±0.18. A

value of m this close to 1 indicates the solitary wave is more hyperbolic than sinusoidal and may be qualitatively described as a hyperbolic peak profile with tails which do not quite go all the way to zero. Fits were made to purely solitonic and hyperbolic profiles with reduced χ^2 4 and 7 times larger than the Jacobi-elliptic fit, respectively.

Phase data, reconstructed from data collected at 40 Gsamples/s without a diode, also confirms the solitonic features of the data. A single round trip is shown in Figure 6.5(a) where the spin wave envelope is plotted as blue dots and a reconstructed phase is plotted as red crosses. The flat phase across the peak profile is a defining characteristic of bright soliton solutions to the NLS, including the general solution given previously in Equation 6.4. The dynamics are additionally verified as being dominated by four-wave mixing by the power spectrum given in Figure 6.5(b). A comb-like, evenly spaced spectrum with 3 identifiable side peaks around the central carrier frequency is observed with a fixed separation of $f_s = 0.28292$ MHz. This equispaced frequency comb is the defining characteristic of four-wave mixing, generated by the conservative equations given in Section 6.3. This frequency difference also corresponds to a round trip time of 353.456 ns, which agrees with the round trip time identified visually from Figure 6.4. The dispersion and nonlinearity coefficients were estimated from fitting recorded dispersion curves and found to be $1.49\text{x}10^{-6}$ cm^{2}rad/ns and -6.27 rad/ns, respectively.

It is important to note that an external field of 311 Oe is not large enough to drive the AFR to a power which forbids the nonconservative three-wave splitting process from occurring within the YIG film. As discussed in Section 6.3 for our AFR geometry, which supports the self-generation of BVSWs, the three-wave mixing process generates half modes which are not observable with the transducers used in this experiment. However, while a stable solitary wave is circulating within the ring, four-wave mixing must remain the dominant dynamical process. Three-wave mixing is therefore considered an additional nonlinear loss. A fully defined bright soliton typically propagates in rings with powers high enough to generate 6 or more four-wave mixing side peaks. The absence of these additional frequency modes

(a) $P_\text{RMS} = 1.0$ (arb)

(b) $P_\text{RMS} = 1.02$ (arb)

(c) $P_\text{RMS} = 1.12$ (arb)
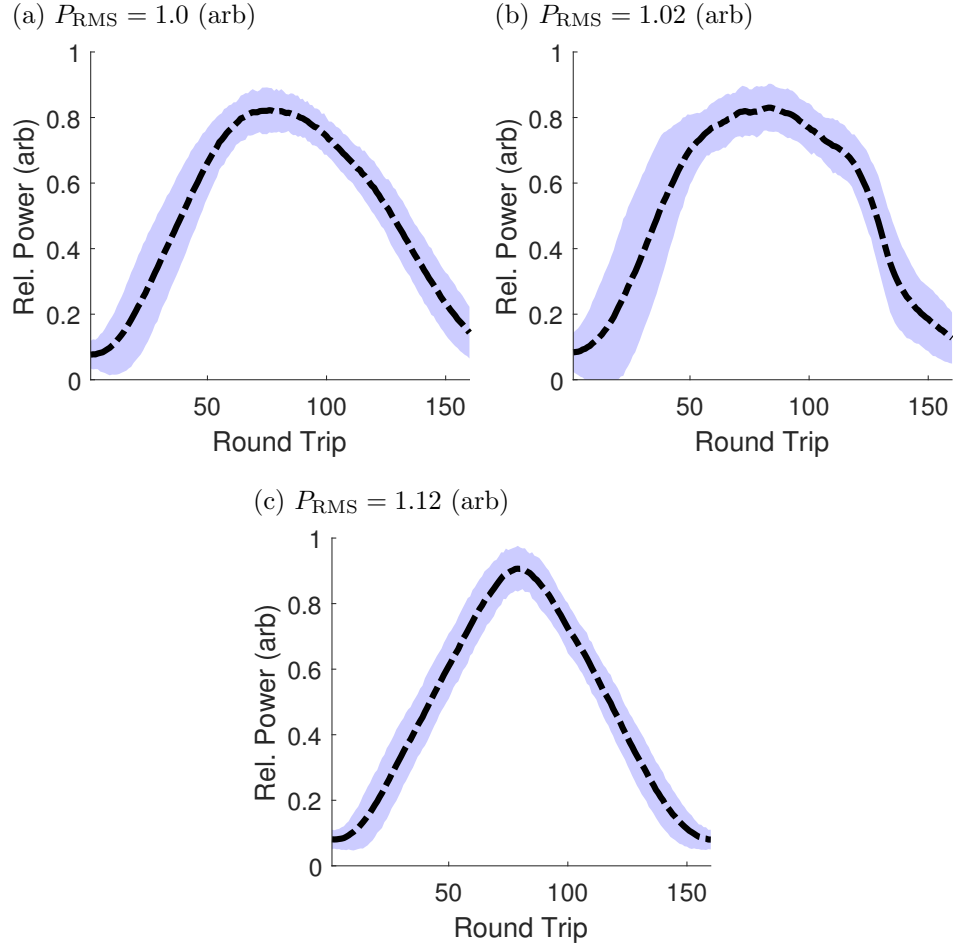
Figure 6.6: Bright solitary wave periodic breathing for increasing ring gain. The breathing profile of a single peak across round trips. Mean of all 262 observed breaths shown as a dotted black line, with a confidence interval constructed from 2 times the standard deviation shown as light blue. Active feedback ring gain is increased from (a) to (c) with the mean RMS power of the observed peaks normalized to low power, (a), given as individual labels. As ring gain is increased the breathing transition becomes sharper, with less time spent at high amplitude.

here, as well as the lower than unity Jacobi-elliptic parameter, indicate that this solitary wave breathing dynamic occurs at lower ring gains than those which support bright soliton wave trains and where higher order losses impact dynamics. This matches the numerical predictions for regimes which support solitary wave periodic breathing where cubic losses were the highest relative loss [34].

A total of three distinct bright single periodic breathers were observed experimentally at increasing ring gain. All were observed at an external saturation field magnitude of 311 Oe. Each breather shared their core characteristics including the following. (1) Their spatial peak profiles fit to a Jacobi-elliptic with a parameter, m, within two standard deviations of 0.69. (2) Half-way through relocation, when both peaks are of equal amplitude, their spatial profile is purely sinusoidal. (3) Parameters such as round trip time, breathing period and group velocity jitter are all within 1% of one another.

As ring gain is increased the temporal profiles of the breathers evolve from purely sinusoidal to being best described by a sharper peak, given by the generic NLS Jacobi-elliptic solution with a parameter of $m = 0.22 \pm 0.11$. The temporal profiles are shown in Figure 6.6 with scaled ring RMS round trip power at maximum peak height increasing from 1.00 ± 0.04 in Figure 6.6(b) to 1.12 ± 0.05 in Figure 6.6(c). Here the mean peak is given by a dotted line and a confidence interval is shown as light blue shading. The interval is constructed by $\pm 2\sigma$ where σ is the standard deviation from all isolated peaks. This sharpening of the temporal profile at higher ring gains is consistent with our hypothesis that three-wave mixing acts as an additional nonlinear loss, impacting the evolution of peak amplitude over long times.

6.4.2 Dark Solitary Wave Periodic Breathing

A periodically breathing dark solitary wave was observed at an external field strength of 446 Oe with a carrier frequency of 2.94 GHz. We again highlight that this dynamic was observed on the same film, on the same day, using the same procedure and experimental setup as was used to generate the bright solitary wave breathers presented in the previous section, Section 6.4.1. The sole adjustment made between the observation of bright solitary

waves and the observation of dark solitary waves was external field strength.

We reiterate that these waves are were not created by injecting carrier waves or from exploiting surface pinning and are the first reported self-generation of dark solitary waves in attractive nonlineary [5, 20].
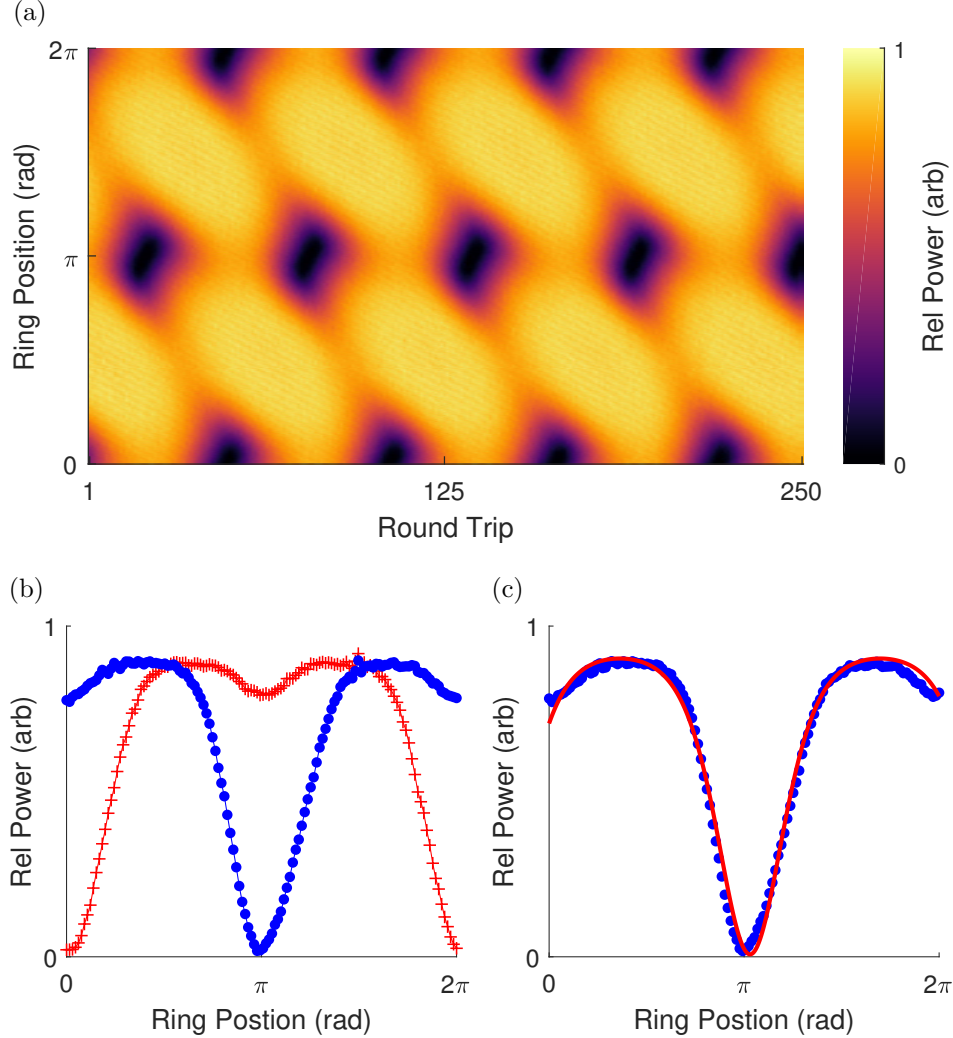
Figure 6.7: Spatiotemporal and round trip plots of Dark solitary wave periodic breathing. A single dark solitary wave breathing at a fixed frequency from the center of the feedback ring to the edge. (a) A spatiotemporal plot of the spin wave power. (b) A single round trip of the dark solitary wave in the center of the ring (dotted blue) and at the edge of the ring a half breath later (crossed red). (c) A fit of a single central round trip to the generalized dark solitary Jacobi-elliptic solution to the NLS.

A dark solitary wave periodic breather is shown in Figure 6.7 where the breathing notches are evident in the reconstructed spatiotemporal Figure 6.7(a) (low amplitude in black). The

dark solitary wave smoothly modulates between a maximum (relative to the background) amplitude of one to zero while undergoing a π positional shift within the ring. This meets the qualitative requirements of a periodic breather discussed early in section 6.4.

A round trip time of 329.34 ns is identified by minimizing the variation in center peak position across all observed 24,000 round trips, or 8.2 ms of data. A peak-fitting algorithm was used to isolate 870 individual peaks and build statistics. A breathing period of 57.18 $\pm$5.01 round trips was determined from these data. A group velocity of $-3.74 \times 10^{-3} \pm 3.07 \times 10^{-5}$ cm/ns was calculated using this round trip and the measured transducer separation of 1.233 ± 0.040 cm. No notable jitter of the group velocity was observed. A dispersion coefficient of 1.73×10^{-6} cm^{2}rad/ns and a nonlinearity coefficient of -7.23 rad/ns were measured by fitting to observed dispersion curves.
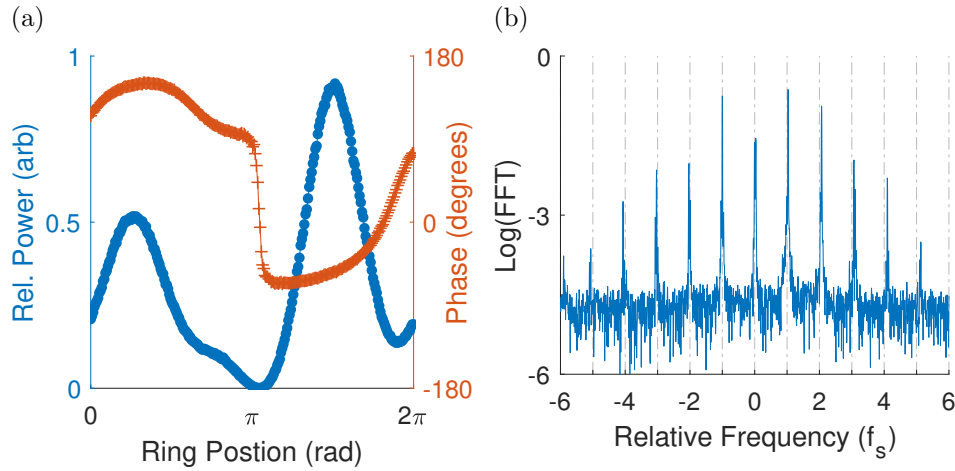
Figure 6.8: Reconstructed phase of dark solitary wave periodic breathing. Reconstructed phase data demonstrating the solitary wave nature of a single dark solitary periodic breather. (a) Phase vs power for a single round trip with the characteristic sharp phase jump at the dark solitary wave peak. (b) Power spectrum about the carrier frequency and scaled by the comb spacing. A well developed four-wave mixing driven frequency combs with two equi-powered eigenmodes, a characteristic of dark solitary waves in a feedback ring, is evident.

A maximum amplitude round trip for a center and edge breath are shown in Figure 6.7(b) as dotted-blue and crossed-red curves, respectively. The solitonic nature of the notch is confirmed by the fit shown in Figure 6.7(c) the solid red line is now a fit to the generic

dark soliton NLS solution, given early in Equation 6.5. A random example of a maximum amplitude round trip is shown here, but fits were made to all 870 identified peaks. A reduced χ^2 of 1.09 ± 0.42 with a reduced $\hat{R}^2$ of 0.98 ± 0.01 and Jacobi-elliptic parameter, m of 0.95 ± 0.01 were measured for the fits to the generic dark soliton solution. A Jacobi-elliptic parameter that close to unity indicates that the peaks are nearly identical to the ideal hyberbolic solution, with only minor edge effects. We note the presence of a small secondary notch located at the edge (center) of the ring for center (edge) breaths. This peak is expected as there must always be a minimum of two notches within the feedback ring to maintain phase continuity without an additional background linear phase increase of π, as discussed previously in Section 6.3.

The dark solitary wave nature of the underlying signal was further confirmed by the spectral and reconstructed phase data collected at 40 Gsamples/s that is shown in Figure 6.8. The data presented here was gathered at the same external field as the data shown in Figure 6.7, but at a slightly higher ring gain. This was to enhance the amplitude of the secondary peak and illustrate the ring phase continuity across multiple dark solitary wave phase shifts. Figure 6.8(a) shows the reconstructed phase as red dots and the carrier wave envelope as solid blue. Here we see the characteristic near π jump for a dark solitary wave with a zero minimum, and lower jumps for smaller notches. The small (order 10 degree) difference in phase across the entire round trip is accounted for by the time delay in the electronic feedback loop, as discussed in Section 6.3. Also note that the phase across the peaks is not linear, indicating that the alternative description of several bright solitary waves propagating around the ring is not sufficient. The spectral data given in Figure 6.8(b) likewise shows the characteristic feature of dark solitary waves propagating within AFSs: two principal eigenmodes of equal amplitude generating a frequency comb via four-wave mixing [5].

The formation of dark solitons in an AFR geometry which supports attractive nonlinearity has previously been shown to be possible via sufficient nonlinear losses [5]. The field studied here, 446 Oe, does not forbid the three-wave splitting process, as discussed early

in Section 6.3. And as in the previous case for bright solitary periodic breathers (see Section 6.4.1), three-wave mixing can be considered an additional source of nonlinear loss. We also remind the reader that these experiments were designed to maximize the time waves spend propagating within the ring by maximizing transducer separation. This design choice explicitly requires higher ring excitation powers to compensate for the major linear loss mechanisms present in the ring. This maximizes the influence of any nonlinear effects, including damping, on the evolution of the wave. As we approach the ring power which forbids three-wave mixing, from below, we expect to maximize the effect of that additional nonlinear-loss mechanism on the solitary wave evolution.

These considerations, taken with the previous observation that peridic breathing occurs at AFR powers below that which support full spectral comb development, account for dark solitary wave periodic breathers at field strengths above those of bright solitary wave breathers.

6.5 Multi-periodic Breathing

Multi-periodic breathing is defined by bright or dark solitary waves which breath at two or more commensurate frequencies. As with periodic breathers, discussed throughout Section 6.4, the breathing behavior is characterized by the oscillation of scaled SWE solitary wave amplitude between zero and one accompanied by a predictable and smooth relocation within the active feedback ring. In this case it will only be necessary that these two events occur once over the longest breathing period, as opposed to during each breath. All data presented in this section was recorded on the same YIG thin film, and on the same day, as the periodic breathers discussed in sections 6.4.2 and 6.4.1. Transducer separation was likewise the same, fixed at 1.233 ± 0.040 cm. Envelope data was collected at 4 Gsamples/s through a diode with a quadratic voltage response.

An example of five bright solitary waves breathing at four frequencies is shown in Figure 6.9. A total of 8.2 ms of data was collected at a saturating external field strength of 383 Oe. A round trip of 1372.82 samples was identified graphically, corresponding to a round
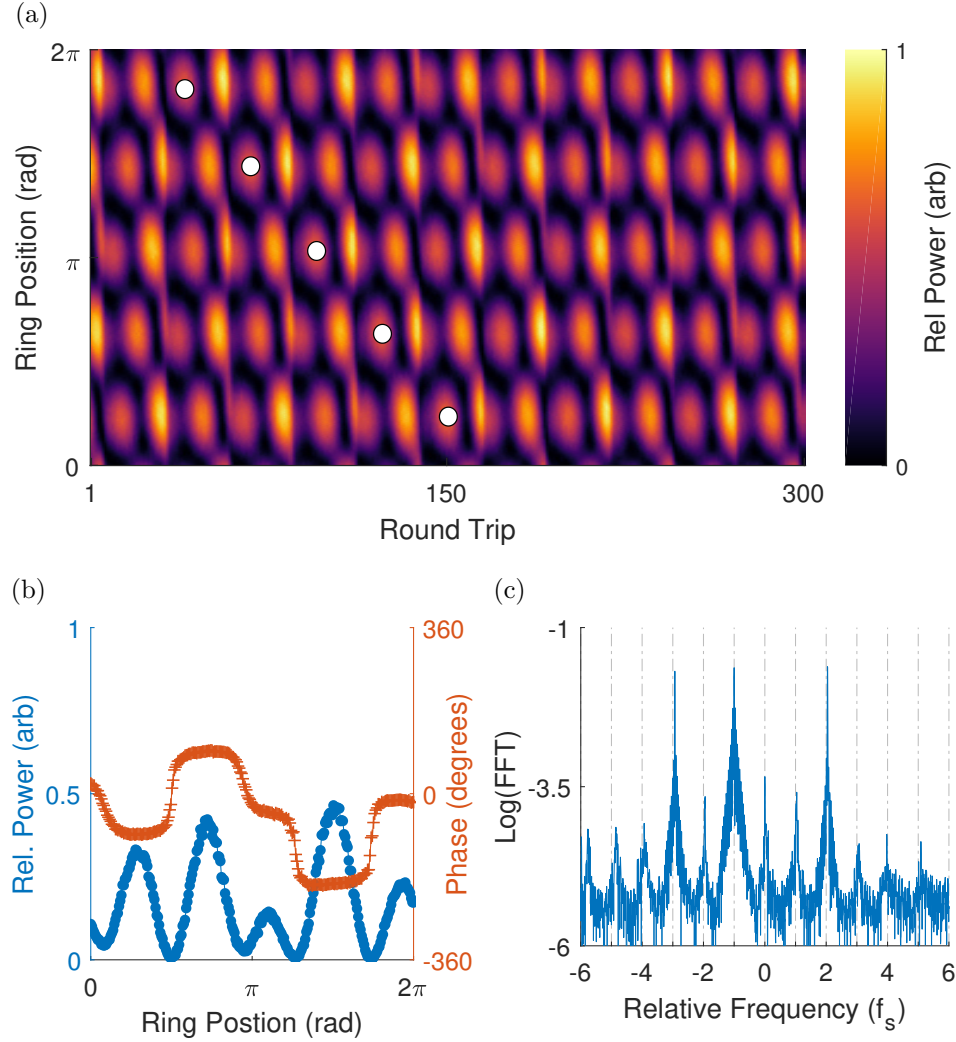
Figure 6.9: Reconstructed phase and round trip data for muliperiodic bright solitary wave breathers. (a) Reconstructed spatiotemporal plot of multi-periodic breathing for five bright solitary waves. Five periods of the principle breathing are shown with white circles. (b) shows the amplitude and phase of a single round trip in dotted blue and crossed red, respectively. Flat phase across the wave peaks is an indication of their solitary wave nature. (c) Power spectrum relative to the carrier frequency and scaled by the comb frequency spacing. The three main peaks peaks associated with eigenmodes which have broadened due to three-wave mixing. The development of a frequency comb from four-wave mixing is also evident, and the fixed frequency spacing of these peaks is shown by the dotted grey lines.

trip time of 342.2 ns. A total of 23,892 round trips were recorded. Group velocity amplitude may be easily estimated using the round trip time and fixed transducer separation, yielding $-3.59 \times 10^{-3} \pm 1.02 \times 10^{-4}$ cm/ns. Finally, coefficients for dispersion and nonlinearity were determined by fitting to observed dispersion curves, giving values of $D = 1.73 \times 10^{-6}$ cm^{2}rad/ns and $N = -7.23$ rad/ns, respectively.

Four distinct frequencies of breathing with a common period of 238.7 round trips were identified via the spectral analysis of the envelope data. The associated breathing periods are found to be 17.04, 26.52, 47.69 and 59.98 round trip times, meaning a total of 14, 9, 5 and 4 cycles are required, respectively, to complete a common breath of 238.7 round trips. White circles in the reconstructed spatiotemporal chart, shown in Figure 6.9(a), illustrate five iterations of the highest power breathing frequency, given by a $2\pi/5$ relocation of the solitary wave train every 26.52 round trip times. The fastest breathing period, occuring every 17.04 round trips, corresponds to the peak modulation time at any fixed ring position. The remaining two periods correspond to the variability in peak profiles across round trips at a fixed ring position and are difficult to isolate visually. It is worth highlighting the non commensurate nature of the breathing frequencies. While each breathing behavior will complete the number of cycles listed above over the duration of single common breath, that does not suggest a total recurrence of the initial state. The common breath is the minimum number of round trips required to complete an integer number of each of the four breathing periods. For example, the $2\pi/5$ relocation event completes a trip around the ring every 5 of its periods, but will complete 9 such relocations during a common breath resulting in a $2\pi/5$ shift relative to the initial condition.

A single round trip of the bright multi-periodic breather is shown in Figure 6.9(b) where crossed-red is phase in degrees, and dotted-blue is scaled amplitude. Binned data is marked and solid curves are provided as a guide for the eye. Five distinct bright solitary waves may be identified as present within the AFR. Flat phase across the bright SWE strongly suggests that the waves are solitonic in nature.

Individual peaks were not isolated. However, individual round trips were best fit by sums of the general bright solitary wave solution to the NLS with Jacobi-elliptic parameters, m, ranging from 0.20 to 0.9. These fits had reduced χ^2 on the order of 10, but were significantly better than fits of sums of hyberbolic and sinusoidal functions where reduced χ^2 was routinely above 50. All three options have mean reduced r^2 above 0.95. Each individual peak maintains its qualitative spatial and temporal profiles while breathing.

While the external field strength studied here, 383 Oe, yields a spin wave power which is is too low to forbid the three-wave mixing process, we can be certain that the dynamics present within the AFR are dominated by the four-wave mixing process. The frequency spectrum relative to the carrier frequency, 2.644 GHz, reconstructed via data collected at 40 Gsamples/s, is given in Figure 6.9(c). Here the frequency axis has been scaled by a characteristic frequency comb spacing, which is generated via the conservative four-wave mixing of ring eigenmodes, $f_s = 2.92 \times 10^{-3}$ GHz. The dashed grey lines indicate the position of integer multiples of f_{comb} from the carrier frequency, and match the locations of the spectral peaks. We highlight, as discussed in Section 6.3, that the spectral distance between ring eigenmodes is not constant, so the presence of an equi-spaced frequency comb is characteristic of four-wave mixing dominating the dynamics. The frequency comb present in this case has much broader peaks than that of a single period bright soliton breather, see Figure 6.5(b), which is indicative of the presence of a third ring eigenmode (higher ring power) and in general with increased dynamical complexity. This type of peak broadening is most likely attributable to three-wave processes acting at higher ring powers, as this behavior has 220% increased average round trip rms power than the single frequency case. Also note that this comb spacing corresponds to a round trip time of 341.67 ns which is within 1% of our previously estimated value.

Multi-periodic breathing was also observed in dark solitary waves on the same film and on the same day as the rest of the data in Section 6.4. These dark soliton wave multi-periodic breathers were recorded with an external field strength of 460 Oe with an observed carrier
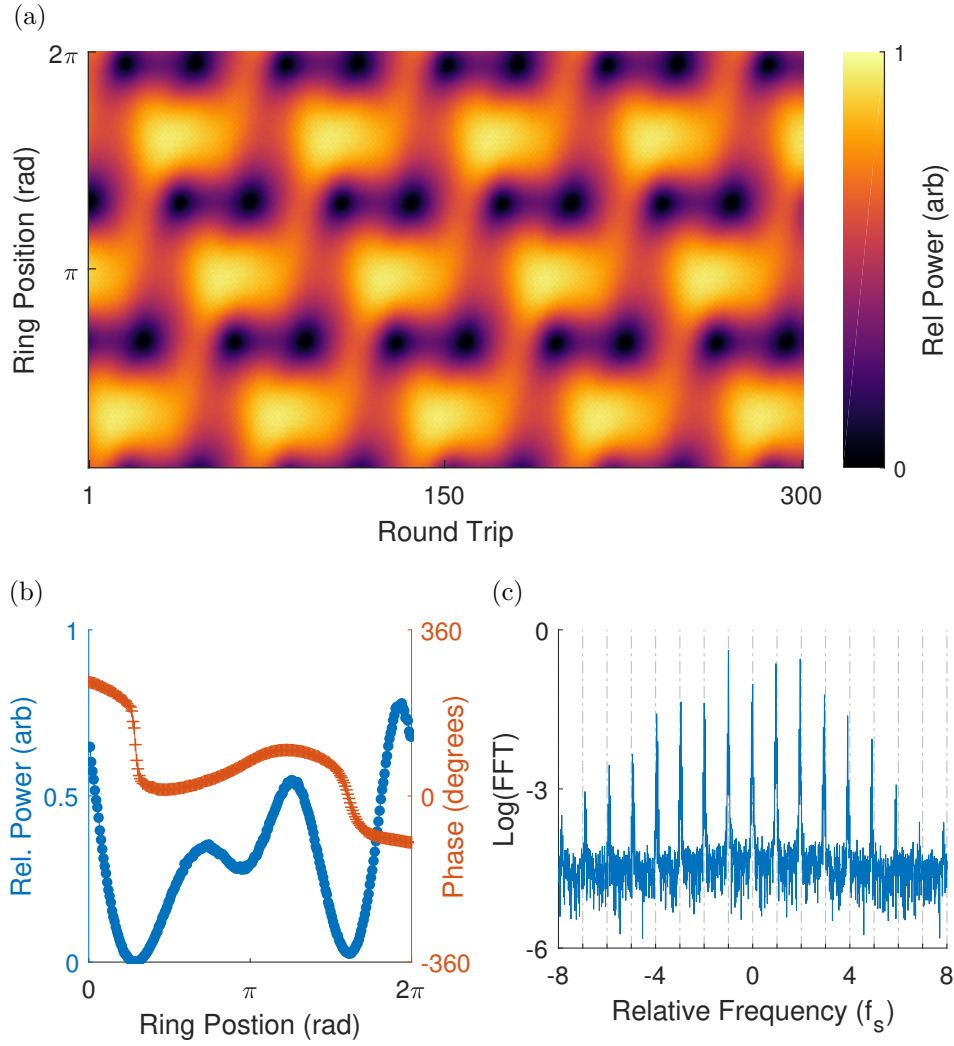
Figure 6.10: Spatiotemporal and round trip plots for multiperiodic dark solitary wave breathers. Reconstructed spatiotemporal plot of multi-periodic breathing for three dark solitary waves. (b) Amplitude and phase of a single round trip in dotted blue and crossed red, respectively. Data is binned for clarity. Near π phase jumps across the the wave peaks is an indication of their solitary wave nature. (c) Power spectrum showing two peaks associated with eigenmodes which have developed a frequency comb from four-wave mixing. The fixed frequency spacing of these peaks is shown by the dotted grey lines. Data shown here is about the carrier frequency and scaled by the comb frequency spacing.

frequency of 2.941 GHz. The round trip time was graphically identified to be 1316.484 samples by minimizing variance in group velocity across all 24,915 observed round trips. These values correspond to a round trip time of 329.12 ns and an estimated group velocity of $-3.74 \times 10^{-3} \pm 1.03 \times 10^{-4}$ cm/ns. Dispersion and nonlinearity coefficients were also estimated via fitting to observed dispersion curves, giving values of of $D = 1.76 \times 10^{-6}$ cm^{2}rad/ns and $N = -7.31$ rad/ns, respectively. We highlight, as discussed in Section 6.4.2, that this combination of attractive nonlinearity with dispersion does not predict the generation of dark solitary waves without the presence of higher order effects. The carrier frequency and external field strength here likewise does not forbid the three-wave processes which are anticipated to contribute higher order losses to the peak evolution.

A reconstructed spatiotemporal plot is given in Figure 6.10(a) where three dark solitary waves can been seen undergoing multi-periodic breathing involving a $2\pi/3$ relocation as the waves evolve through time. The dark solitary wave nature of the signal can be confirmed by examining the relative phase of a single round trip, reconstructed via sampling at 40 Gsamples/s without a diode, plotted in Figure 6.10(b). Dotted-blue is the wave amplitude and crossed-red is phase. A signature characteristic of dark solitary waves is seen in the near π phase jump at minimums.

An equi-spaced spectral comb located around the carrier frequency is shown in the power spectrum plotted in Figure 6.10(c). Here the frequency has been scaled by the characteristic comb width given by $f_\text{s} = 3.08 \times 10^{-3}$ GHz, and integer multipliers of f_s relative to the carrier frequency are indicated with dotted-grey lines. A more robust comb structure is evident in this example than was for the single period dark solitary wave breather (see Figure 6.8(b)), driven by a 125% increase in average round trip rms power. We note that four-wave mixing remains the principal driver of dynamical behavior with all additional spectral peaks falling on integer multipliers of f_s.

Three noncommensurate breathing frequencies were identified via spectral analysis of the envelope. The associated breathing periods are given by 13.46, 16.82, 22.42 round trips.

The minimum number of round trips necessary for all three periods to complete an integer number of periods is 67.3 and requires 5, 4 and 3 completed cycles, respectively, from the identified breathing periods. This common period corresponds to three $2\pi/3$ relocations of the maximum amplitude dark solitary wave. The remaining shorter periods correspond to shifts in the relative depth of individual dark solitary waves prior to the relocation events.

6.6 Complex Recurrence

Recurrence is a common phenomenon in nonlinear systems and is defined by a long-period pattern or replication of a key feature. The period for recurrence is longer than any characteristic period in the problem, which distinguishes the behavior from the breathing dynamics described in sections 6.4-6.5. The Fourier spectrum of a recurrence solution is broadband around the recurrence frequency, whereas breathers are clean. This kind of recurrence is not due to two or a few noncommensurate frequencies, but involves many conspiring factors in pattern formation – this is why we call it complex. For example, consider two solitary waves circulating the ring with different velocities so that they overtake each other at a fixed frequency. This is not considered complex recurrence, nor are the multi-periodic breathing dynamics of Section 6.5. Here we look at two examples of recurrence observed in the system, one of bright solitary waves and one of dark solitary waves. We observe varying degrees of complexity in the recurrence pattern, as well as frequency.

We note explicitly that our working definition for recurrence here excludes other types of recurrence that have been previously reported within AFR such as Fermi-Pasta-Ulam recurrence where two clean solitary waves undergo periodic recombination. This is a choice we make consciously, as we are describing a family of increasingly complicated dynamical behaviors that begin at a complexity stage above that of co-propagating solitary waves. Moreover, these dynamics appear to occur at ring gains, fields, and powers which do not support stable bright solitons. Rather they occur at a crossover point at lower ring powers where novel dynamics are enabled by the peak broadening effects of three-wave mixing but dynamics are still principally driven by four-wave mixing.

(a)

(b)
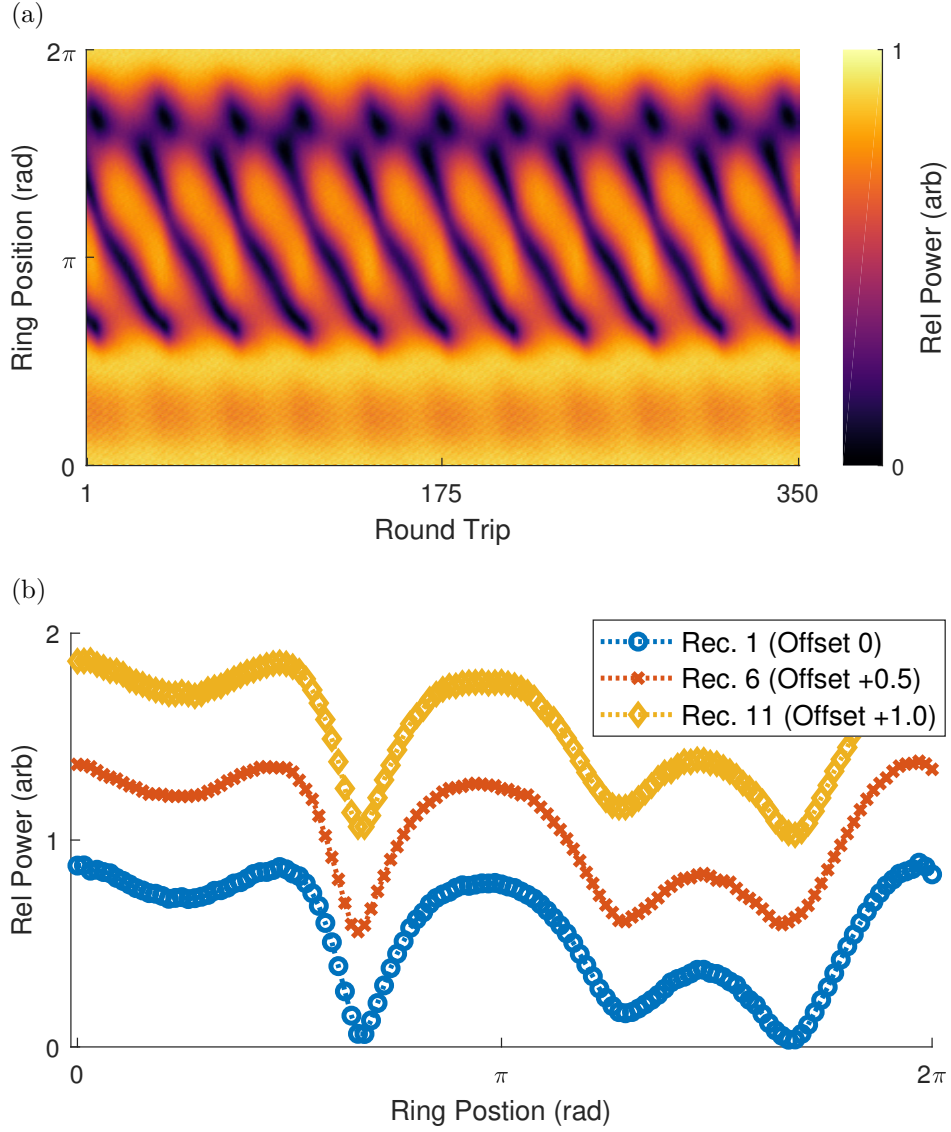
Figure 6.11: Spatiotemporal and round trip data for dark solitary wave recurrence. (a) A reconstructed spatiotemporal plot of three dark solitary waves undergoing a complex recurrence. The nontrivial repeating shape can be identified easily, as can its periodicity. (b) The single round trips of recurrence 1, 11 and 16. These plots have been shifted by 0, 0.5 and 1 in power, respectively, to aid with direct comparison. Actual relative errors between these events is on the order of 10% which is expected since our resolution is by the round trip, and we may not capture the exact recurrence trip.

The recurrence of a dark solitary wave is shown in Figure 6.11(a) in a reconstructed spatiotemporal plot. This particular data set has a recurrence time of 34 round trips. The first, sixth, and eleventh recurrence event are shown in Figure 6.11(b) with a vertical offset for later recurrence events to allow for a direct visual comparison. The relative error between these recurrence round trips is on the order of 5%, which is not unexpected since our resolution is limited to a round trip and its unlikely we'll fully observe the entire recurrence event.

A round trip time of 1317.374 samples was identified graphically, or 329.34 ns, slightly slower than that reported in the multi-periodic solution — but well within our margins of error. 8.2ms of data was collected, or 24897 round trips and 730 distinct recurrence events.

This behavior was observed under the same conditions as the multi-periodic dark solitary wave breather, above, only at a higher total ring gain resulting in an average RMS round trip power 13% greater than in the previous example. The field strength and carrier frequency remain the same.

A shift from multi-periodic breathing into a more complex dynamic such as recurrence as ring gain is increased is not surprising. Higher ring gains result in additional eigenmodes circulating the thin film, and further, since this data was collected in a regime where three-wave mixing was not forbidden, we do expect higher powers to result in spectral peak broadening. This example was included here not because of its particularly complex nature, but rather as an illustrative example of how ring dynamics increase in complexity as the spin wave power increases. The progression from a single solitary wave periodic breather, to multi-periodic multi-peak breathers ultimately into the broadband reccurence shown here is natural.

At higher ring gains and fields even more complex recurrence events are common. An example of this with five bright solitary waves circulating the ring is shown in Figure 6.12(a) where a reconstructed spatiotemporal plot shows three periods of a highly intricate recurrence event. This behavior exhibits a recurrence every 316.6 round trips. The individual round trips for recurrences 1, 6 and 11 are plotted in Figure 6.12(b) with power offsets to allow for

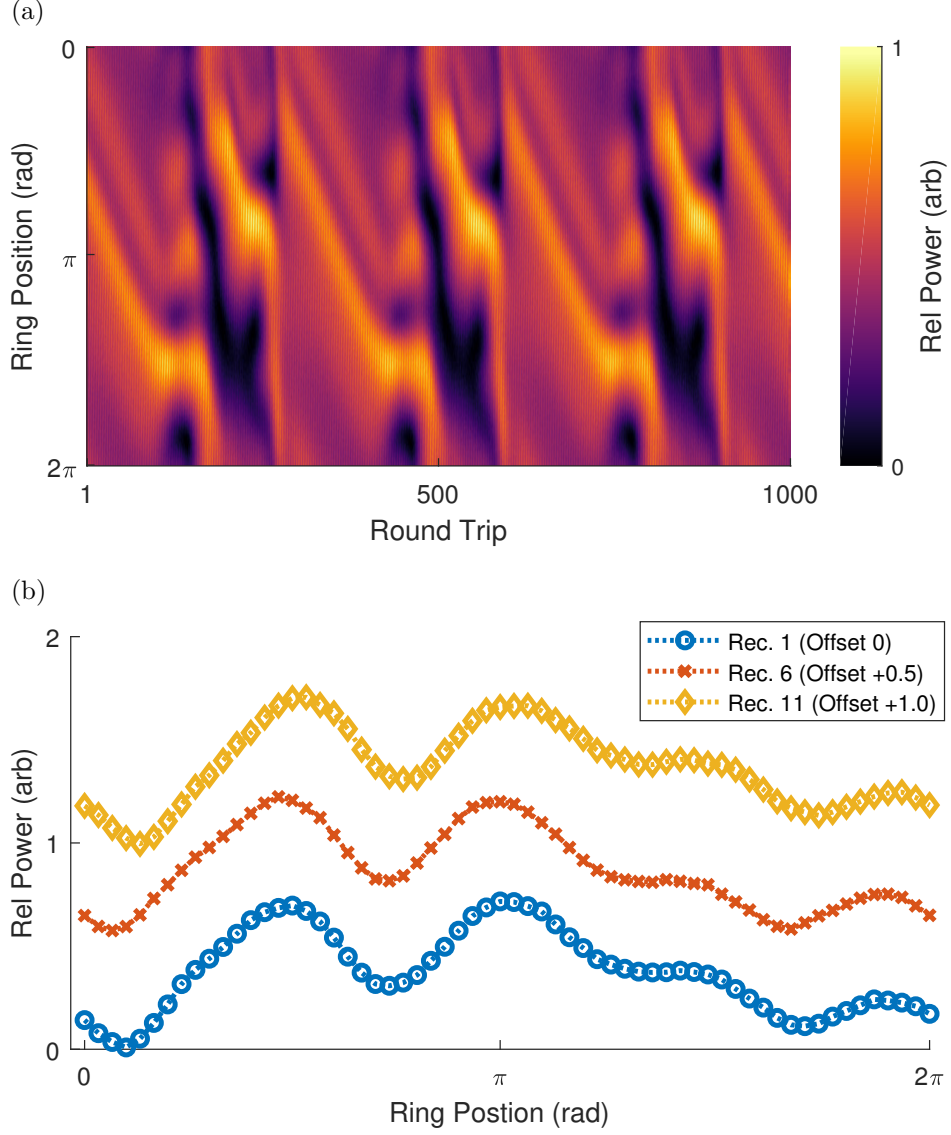Figure 6.12: Spatiotemporal and round trip plots for bright solitary wave recurrence. (a) Four bright solitary waves undergoing a complex recurrence. Format is the same as Figure 6.11. The nontrivial repeating shape can be identified easily, as can its periodicity. (b) The single round trips of recurrence 1, 11 and 16. These plots have been shifted by 0, 0.5 and 1 in power, respectively, to aid with direct comparison.

the visual comparison. The percent error between the first recursion and the 6th and 11th recursions is on the order of 5% at each point. This is not unexpected since our resolution is limited to individual round trips and the actual recursion time is not an integer.

This data was collected at a field strength of 773 Oe and a sampling rate of 1 Gsample/s through a diode with a quadratic response to voltage. A round trip time of 245.485 ns was identified graphically by minimizing the variation of the group velocity over the recorded 66,806 round trips covering 16.4 ms. The transducer separation was measured to be 1.147 cm with a photo microscope. An estimate of group velocity may obtained from the round trip time and the transducer separation, giving -4.68×10^{-3} cm/ns which closely matches the group velocity obtained from recorded dispersion data of $4.77 \pm 0.32 \times 10^{-3}$ cm/ns. Dispersion and nonlinearity coefficients were also obtained via fitting to recorded dispersion data, giving $D = 2.9 \times 10^{-6} \pm 1.8 \times 10^{-7}$ cm^{2}rad/ns and $N = -8.72$ rad/ns both in close agreement with other experiments of this kind.

6.7 Spontaneous Spatial Shifts

The most dramatic dynamical behavior observed is the spontaneous spatial shift. This behavior is characterized by quick, unpredictable movement of an otherwise underlying behavior from one place in the ring to another (in the group velocity frame). Unique from the previous two examples of periodic breathing and complex recurrence, spatial shifting does not occur at a fixed frequency and involves an abrupt, unpredictable transition rather than smooth, periodic relocation or recombination.

An example of spontaneous spatial shifts is shown in Figure 6.13 where two spatial shifting events are observed over 12,000 round trips. The otherwise stable underlying dynamic which undergoes the spontaneous spatial shifting is two co-propagating bright solitary waves undergoing periodic modulation. A high amplitude main peak modulates alongside a smaller side peak. The periods of the modulation are the same for each peak, 61.19 round trip times, but are out of phase. The smaller peak modulates from a scaled power of 0 to 0.7, while the larger peak modulates from a scaled power of 0.7 to 1. Note that the smaller peak is

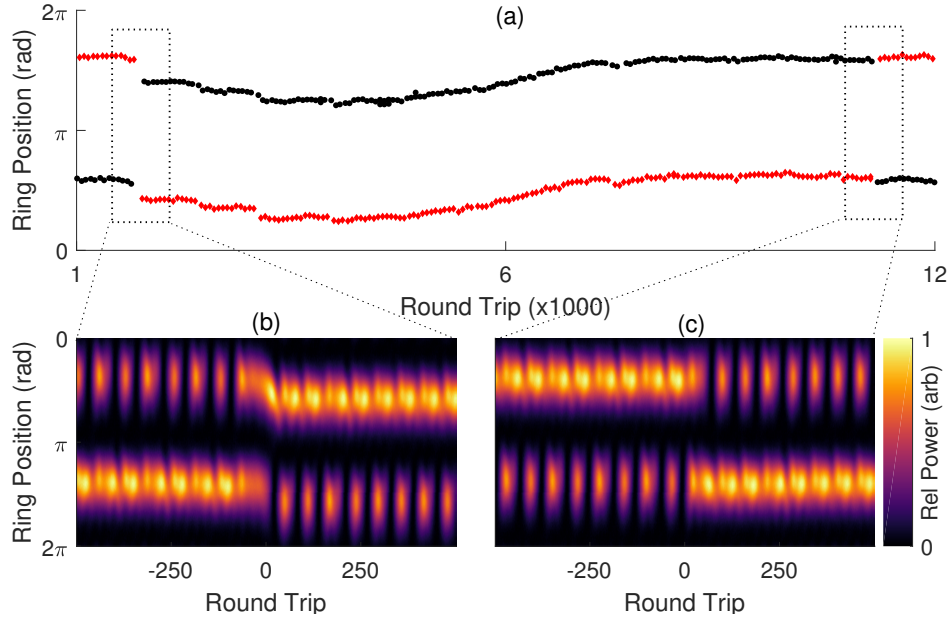Figure 6.13: Detected peaks for spontaneous spatial shifting (a) All peaks detected for a spontaneous spatial shifting behavior. Red dots indicate the short peaks which oscillate between a normalized magnitude of 0.7 and 0, while black dots show the high peaks which oscillate between 0.7 and 1. (b) Two shifting events when the relative location of the two stable modulating solitons abruptly shifts within the ring.

not undergoing the periodic breathing dynamic discussed earlier in Section 6.4, as it does not undergo any predictable relocation within the ring. This behavior was also predicted by our previous numerical phase space exploration [34] where we refer to it as "complex co-propagation." We found it occurred when all losses present within the AFR were roughly of the same order. This means we expect this dynamical behavior to exist when additional losses from three-wave splitting are forbidden, as is the case here where the external field strength was 565 Oe resulting in a operating frequency of 3.37 GHz. This is above the minimum frequency required to forbid three-wave splitting as discussed in 6.3.2. Figure 6.13a shows the isolated peak locations of the high amplitude modulating solitary wave as black dots and of the low amplitude solitary wave as red diamonds. The two spontaneous spatial shifts are isolated into reconstructed spatiotemporal plots b and c. Both relocation events occur over less than 100 total round trips, with the first event being the less clean of the two. The stability of the underlying complex co-propagation before and after the spontaneous spatial shifts is evident.

This data were collected at a sampling rate of 4 Gsample/s and a round trip time of 324.917 ns was identified graphically by minimizing the variation of the group velocity over the recorded 25,236 round trips covering 8.2 ms. The transducer separation was measured to be 1.232 cm. An estimate of group velocity can be obtained from the round trip time and the transducer separation, giving -3.9×10^{-3} cm/ns which closely matches the group velocity obtained from recorded dispersion data of $-3.79 \pm 0.21 \times 10^{-3}$ cm/ns. Dispersion and nonlinearity were $D = 1.9 \times 10^{-6}$ cm^{2}rad/ns and $N = -7.85$ rad/ns. The peaks for both the main and side peaks were isolated and used to determine the jitter in group velocity showing of change of $0.96 \pm 2.6 \times 10^-4$cm/ns per round trip. This amounts to a less than 1% change in group velocity per round trip, and the jitter is roughly normally distributed with an Anderson-Darling statistic of 2.5 where normality is formally rejected at a level of 0.75. 402 major and minor peaks at maximum amplitude were best fit to a Jacobi-elliptic cn with a $\chi^2 = 0.29 \pm 1$ with a parameter $m = 0.97 \pm 0.11$ and a mean adjusted r$^2 = .99 \pm 0.01$

confirming the bright solitary wave nature of the underlying dynamic.

6.8 Intermittency

Intermittency is common in complex dynamical systems and occurs when two or more nearby attractors in phase space overlap. This results in the seemingly random oscillation between two or more distinct dynamical behaviors as the systems moves between attractors. It is important to note that these attractors need not "physically" overlap in phase space, but that drift in experimental parameters such as heating or noise can result in shifts of the nearby basins of attraction that result in dynamical changes.

A typical example of intermittency is shown in Figure 6.14, where Figure 6.14(a) is a reconstructed spatiotemporal plot showing 1500 round trips spanning 3 regions for each of the two underlying dynamical behaviors. The first behavior, shown in crossed-red points in Figure 6.14(b), is a principal peaks periodically modulating with 3 smaller peaks on a floor of relative power 0.4. This type of evolution was also numerically predicted to be observable in this system in previous numerical work [34], where it was called "asymmetrical interactions" on an energy 'plateau' whose amplitude satisfied the energy balance of the CQCGL equation $L + C|u|^2 + Q|u|^4 = 0$. Figure 6.14(a) is reconstructed in the group velocity frame of this dynamic, corresponding to a round trip time of 243.94 ns. Of the 66,000 recorded round trips the ring evolved in the crossed-red behavior for 81% of them. The average occupation duration for this dynamic was 1053 round trips, but varied from 200 up to 3000. It is shown propagating within the ring from round trips 1-357, 682-961 and 1096-1401 in Figure 6.14(a). Figure 6.14(d) is the spatiotemporal plot of the same 1500 round trips as in Figure 6.14(a) but in the group velocity frame of the second dynamic shown as the dotted-blue line in Figure 6.14(b). The second behavior has a round trip time of 245.2 ns and propagates the ring for an average of 260 round trips. The maximum observed continuous lifetime of this behavior was 350 round trips, the ring existed in this regime for 19% of the recorded round trips. The second dynamic propagates within the ring from round trips 357-682, 961-1096 and 1401-1500. This second behavior is four solitary waves
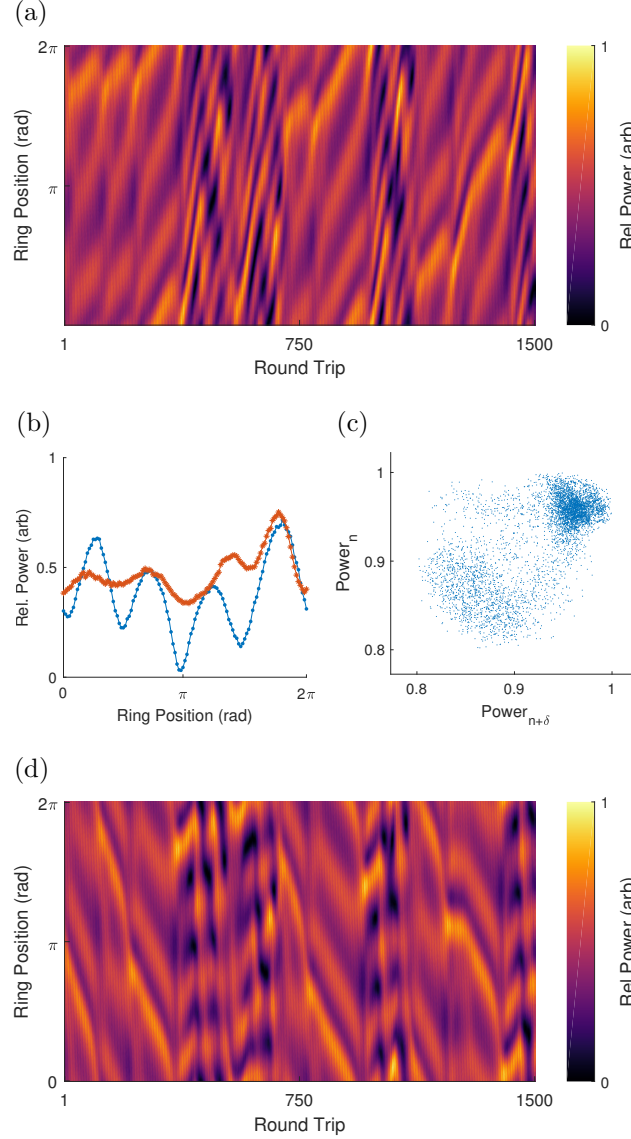
Figure 6.14: Reconstructed attractor and spatiotemporal plots for intermittency (a) Reconstructed spatiotemporal plot showing the unpredictable shifting between two stable dynamical behaviors. The two distinct dynamics are shown in (b) with four interacting solitary waves (dotted-blue points) and 4 waves propagating on a floor of scaled power 0.4 (crossed-red points). (c) Attractor reconstruction with round trip rms power, $E(n)$. The delay, δ, is chosen as the first minimum of the autocorrelation function and $E(n)$ vs $E(n + \delta)$ is shown. Data from 66833 recorded round trips shows the qualitative presence of two overlapping attractors, with a majority of the time spent in the higher rms power state shown as the crossed-red behavior in plot (b). (d) Spatiotemporal plot in the group velocity frame of the *second* dynamic.

interacting. No clear, stable breathing behavior is observed but the waves do modulate and

move about the ring. A total of 102 transitions were observed in the 66,000 recorded round

134

trips of data, corresponding to roughly over 50 distinct propagation periods for each of the two dynamical behaviors.

Figure 6.14(c) shows an attractor reconstructed from the RMS nth round trip power, $E_{\text{rms}}(n)$, via phase space time-delay embedding. Time-delay embedding process involves creating "independent" vectors from a single recorded time series using a delay which minimizes the correlation between success vectors defined as $[E_{\text{rms}}(n), E_{\text{rms}}(n + \delta), E_{\text{rms}}(n + 2\delta), ..., E_{\text{rms}}(n + m\delta)]$ where δ is the delay constant and m is the maximum number of vectors which can be constructed for a finite length time series. The appropriate choice of the delay constant is an active area of debate, but for our qualitative purposes the first zero crossing of the autocorrelation function of $E_{\text{rms}}(n)$ will minimize the linear correlation between successive vectors. Additional discussion of nonlinear time series analysis is well beyond the scope of this paper, and curious readers are directed to these fine reviews as introductions to the field [60, 62, 136]. Figure 6.14(c) shows, qualitatively, the existence of two distinct attractors, where the density of points equates to their relative occupation frequency. The most common ring behavior (crossed-red points in Figure 6.14(b)) has an average scaled RMS round trip power near 1. The second behavior (dotted-blue points) has an average scaled RMS round trip power near 0.9. These numbers are in complete agreement with RMS round trip powers determined by isolating each individual behavior's time within the ring. The relative number of points in the upper right attractor, corresponding to the first behavior, is 77%, while the fraction of points in the lower attractor is 17%. This agrees closely with our relative frequencies above and also suggests roughly 6% of propagation time is spent transitioning from one attractor to another.

This data were collected at the same field strength as the bright soliton complex recurrence above. That is given by 773 Oe and a sampling rate of 1 Gsample/s. Round trip times for each behavior were identified graphically by minimizing the variation of the group velocity over the recorded 66,000 round trips totaling 16.4 ms. The transducer separation was fixed at 1.147 cm. Group velocity estimates are obtained from the round trip time and the transducer

separation, giving -4.52×10^{-3} cm/ns and -4.49×10^{-3} cm/ns for the first and second behaviors listed above, respectively. These are again in close agreement with the group velocity determined from the experimentally measured dispersion curve, $4.77 \pm 0.32 \times 10^{-3}$ cm/ns. Dispersion and nonlinearity coefficients were $D = 2.9 \times 10^{-6} \pm 1.8 \times 10^{-7}$ cm^{2}rad/ns and $N = -8.72$ rad/ns.

6.9   Conclusions and Outlook

We report the clean experimental realization of 10 complex behaviors across 4 distinct categories of dynamical pattern formation that were previously numerically predicted [34] to be observable for backward-volume spin waves (BVSWs) propagating within active magnetic thin film-based feedback rings (AFRs). These four regimes span (1) periodic and multi-periodic breathing, (2) complex recurrence, (3) spontaneous spatial shifting, and (4) intermittency. We provided experimental examples of all these behaviors and performed quantitative analysis including reconstruction of the strange attractor underlying (4). Besides these predicted behaviors, we also discovered dynamical pattern formation for dark solitary waves which evolve under attractive instead of repulsive nonlinearity. Dark solitary waves were observed in the regimes of periodic and multi-periodic breathing and complex recurrence organically via self-generation and without any external potentials, sources or other effects.

Our results confirm that the cubic-quintic complex Ginzburg-Landau equation (CQCGL) is a simple yet viable model for the study of fundamental nonlinear dynamics for driven, damped waves which propagate in nonlinear, dispersive media. We have demonstrated that spin wave envelope (SWE) solitary waves in AFRs provide an approachable and flexible table top experiment to study the emergence of many complex regimes in nonlinear dynamics. Additionally, our experimental verification of these dynamical regimes show that such ideas are not simply theoretical but in fact occur in the real physical world and are observable in an approachable, tunable spin wave system which matches the conditions of many other real-world physical systems and are therefore promising for technological applications. This

provides for potential benchmarking and insight not only into fiber optics, hydrodynamics, and the many other fields of nonlinear dynamics with classical waves, but can provide for a classical benchmark on gain/loss open quantum systems such as attractive BEC Sagnac interferometers.

Previous studies of dark and bright solitary wave train dynamics of SWE solitary waves in AFRs explicitly occurred in regimes which forbade three-wave splitting. Our work demonstrates that four-wave mixing can remain the dominant dynamical force even when three-wave splitting is allowed for some or all of the spin wave passband. This opens up additional spin wave regimes for studying solitary wave train dynamics and additional exploration of this phase space. Similar explorations for forward volume and surface spin waves and mixed excitation should yield intriguing and important dynamical behaviors. Transient dynamics in these regimes also should be investigated. Further exploration of additional spin wave regimes and numerical study of dark solitary wave dynamics are also warranted and verification of the existence of similar dynamical behaviors in analogous physical systems would be exceedingly valuable.

CHAPTER 7

OTHER SPIN WAVE CONTRIBUTIONS AND CALCULATIONS

This chapter contains additional work done which has not yet been published or was published or associated with co-author papers not explicitly included as chapters. Detail of the context of each work is provided below.

7.1 Chaotic Modulation of Envelope Solitons in Active Feedback Rings

This section details the collaborative effort of analyzing and modeling chaotic solitary wave data from Wu's system which ultimately resulted in the publication of a PRL [31]. That work contained numerical simulations of the GLNLS for chaotic solitons with high and low envelope modulations. Details of those simulations were later included as part of the NJP detailed in Section 5, and have also been published in Wu's book chapter and Wang's PhD Thesis [34, 41, 43]. This chapter contains thorough analysis of the experimental data, including for ring gains higher than were included in the PRL.

Associated reference [31]: Zihui Wang, Aaron Hagerstrom, Justin Q. Anderson, Wei Tong, Mingzhong Wu, Lincoln D. Carr, Richard Eykholt, and Boris A. Kalinikos. Chaotic spin-wave solitons in magnetic film feedback rings. *Physical Review Letters*, 107(11), 2011. ISSN 00319007. doi: 10.1103/PhysRevLett.107.114102.

The data analyzed in this section was generated by Mingzhing Wu's group at CSU in the manner described in the preceding section. Following the phenomenology of CSU's gain labeling, where $G = 0.0$ dB corresponds to single self-generated eigenmode, we focus on results from five distinct ring gains: 2.00 dB, 2.25 dB, 2.50 dB, 2.75 dB, and 3.0 dB. We note these gain values are recorded by eye from an analog attenuator and are principally useful as a means of comparison within this single experiment. All of the data presented here were generated from a single active feedback ring experiment in which gain was incrementally

increased and all other parameters were fixed. Only gains 2.00 dB, 2.25 dB and 2.50 dB were presented in the paper [31].

An overview of the data for all gains is shown in Figure 7.1. Here observed ring signal is shown at increasingly fine time scales from left to to right across a row, and for increasing ring gain from top to bottom along a column. The top row, (i), corresponds to a ring gain of 2.0 dB, the bottom row, (v), to 3.0 dB. Ring gain increases in steps of 0.25 dB down a column. The leftmost column, (a), demonstrates modulation on the scale of the train's envelope or hundreds of round trips. The middle column, (b), demonstrates the solitonic train nature of low gain signals and modulations on the scale of 10 round trip times for high gains. The right most column, (c), shows the observed signal for a single round trip with actual data presented as points. Magnitude has been normalized to one.

Several important trends are evident from the time series. First, in the longest time scales, column (a), the complexity of modulation is seen to increase dramatically with ring gain. Second, the solitonic nature of the signal is seen to degrade with increasing ring gain in columns (b) and (c). While the bright soliton train is robust at gains 2.25 dB and below, it begins to degrade at 2.5 dB is completely lost by 2.75 dB. At 3.0 dB multiple peaks are circulating the ring. This suggests three distinct evolution regimes within the system. At ring gains lower than 2.5 dB modulations are not severe enough to distort the underlying bright soliton state. While at gains lower than 3.0 dB and higher than 2.25 dB modulations are severe enough introduce significant asymmetries into the bright soliton evolution. In these two regimes we note that increasing ring gain principally manifests itself as an increase in the magnitude of modulations at long time scales, as in column (a). Finally at high gains, above 2.75 dB, the underlying solitonic nature of the evolution is destroyed and multiple solitary waves evolve within the ring.

The degradation of underlying bright solitary wave train is of principle concern for the study of chaotic solitons and has serious implications on any attempts to numerically simulate the behavior. Fundamentally if the timescale of the dynamics approach the timescale of a
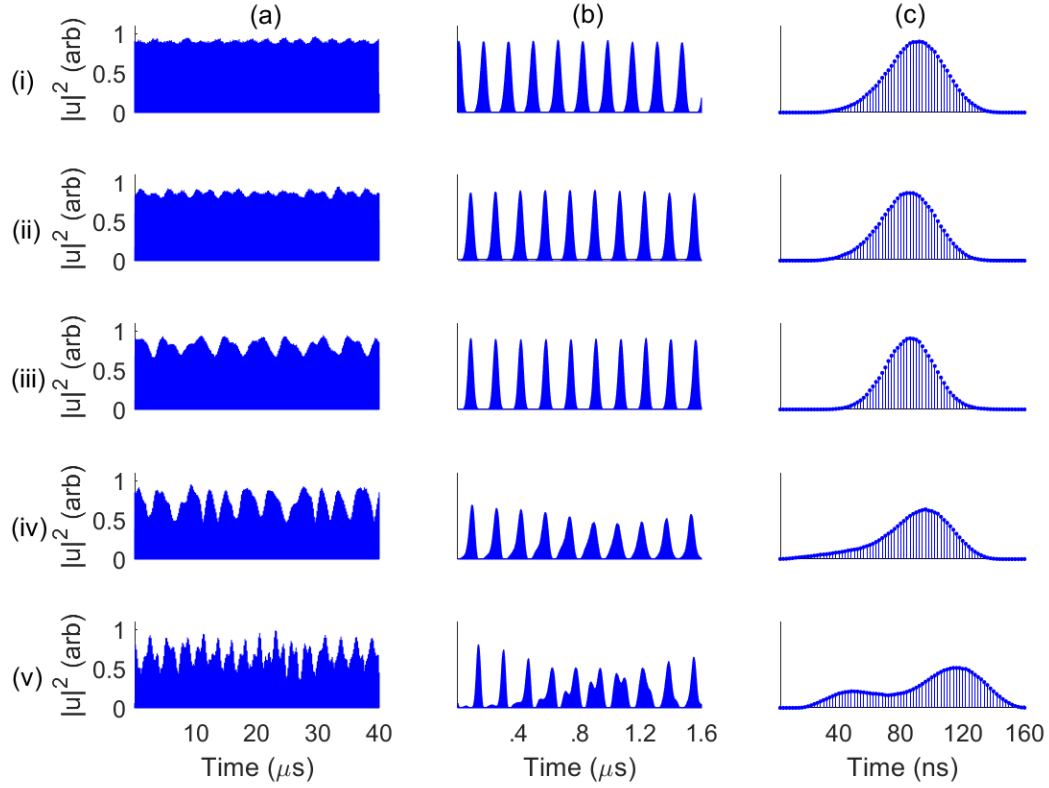
Figure 7.1: Overview of observed ring signals for increasing ring gain.Overview of observed ring signal for increasing gain. Left, (a), to right, (c), is the same experimental time series at decreasing time scales. Gains increase in steps of 0.25 dB from top to bottom: (i) 2.0 dB, (ii) 2.25 dB, (iii) 2.5 dB, (iv) 2.75 dB and (v) 3.0 dB. The (a) series shows the long time envelope modulation behavior, (b) shows medium scale train behavior and (c) shows a single round trip. From (ii)(a) to (iii)(a) we note a jump in modulation amplitude, and from (iv)(a) to (v)(a) we note a reduction in modulation period. In the (b) series we note the soliton train degrades until two peaks circulate the ring in (v)(b). Likewise we see the degradation of the bright soliton envelope in the (c) series until the twin peak waveform in (v)(c). All columns share temporal axes, and all rows share scaled power axes. Plots along a row are generated from the same time series.

single round trip, as in the 3.0 dB case, then any any attempts to model that behavior must be able to account for dynamics on the same time scale. Previous attempts at simulating dynamics within the ring, see Chapter 7 and Chapter 5, while fruitful did not examine behaviors on the timescale of the a single round trip. The results in this section suggest an iterative model, conceptually introduced in Chapter 3, may ne necessary to full explain chaotic solitons.

We have identified that by 2.75 dB the soliton evolution has degraded to point where examining single peaks is no longer meaningful. Figure 7.2 examines the soliton nature of single round trips, again with increasing down a column beginning with 2.0 dB and increasing in steps of 0.25 dB. Column (a) shows the peaks with the highest, dashed red line, and lowest, dotted red line, heights observed at a given ring gain. Included in solid blue is a soliton generated by averaging all those observed for a given ring gain, termed the mean soliton. The right column, (b), contains similar information. However in this case the top, dashed red, and bottom, dotted red, five percent of observed solitons, by height, are averaged to demonstrate the extreme cases plotted in column (a) are indicative of a trend rather than exceptions. For gains 2.0 dB and 2.25 dB the secant shape of the underlying dynamics are well preserved. At 2.5 dB sharp asymmetries are evident in the shape of the train. Despite these distortions the average peak is still secant shaped. This suggests a regime change at gains above 2.25 dB.

Hallmarks of chaotic evolution and regime changes are also apparent from further analysis of the full time series. Figure 7.3 shows power spectrum data where ring gain increases in steps of 0.25 dB moving down a column, and all figures within a row are different frequency scales. Reported frequencies are about the carrier wave frequency. A development of a broadband power spectrum with increasing ring gain is evident in Figure 7.3. A wide frequency scale is shown in column (a) while the principal peak is plotted in column (b).

The above analysis of the observed time series at increasing ring gains point strongly towards either a deterministic chaotic or random evolution of the spin wave envelope. We
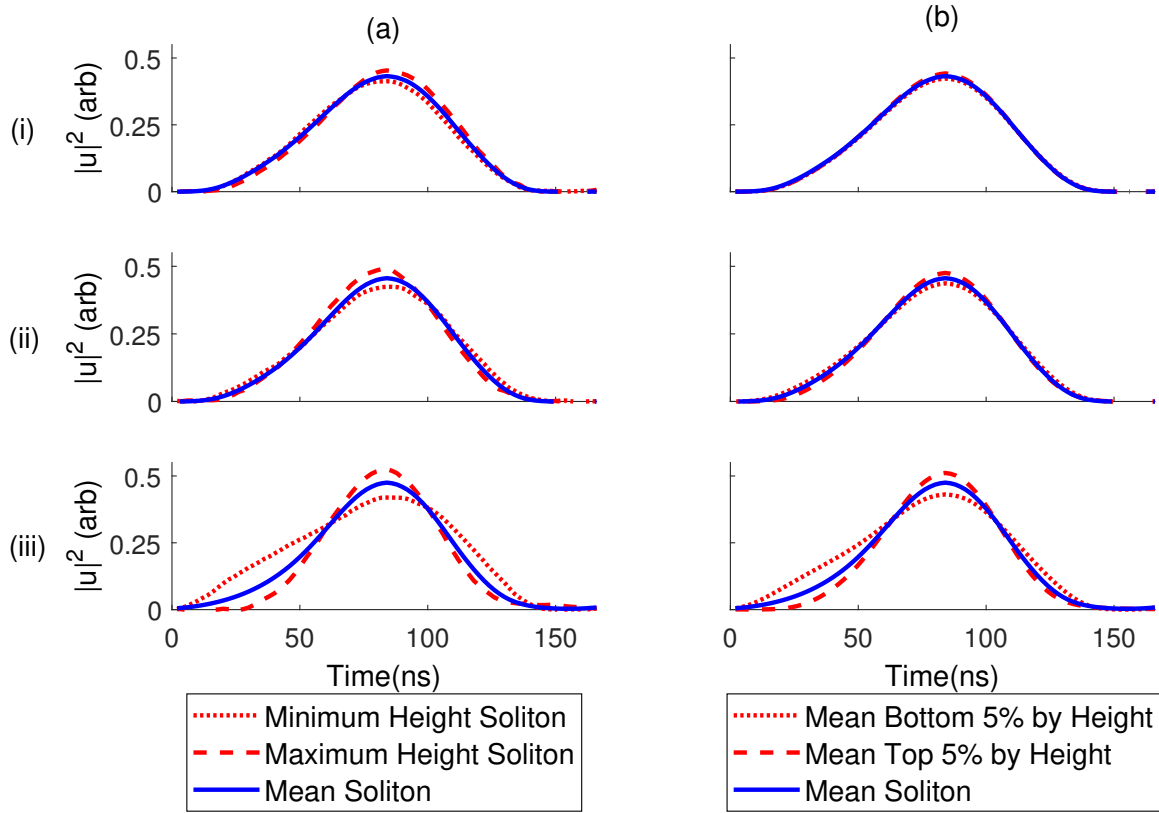
Figure 7.2: Solitary wave train variance with increasing ring gain. Examination of the soliton nature of ring evolution at ring gains below 2.75 dB. Gains increase in steps of 0.25 dB from top to bottom: (i) 2.0 dB, (ii) 2.25 dB and (iii) 2.5 dB. Column (a) shows the highest, dashed red, and lowest, dotted red, observed soliton, by height, for a given time series. Column (b) shows the mean of the tallest five percent of observed peaks, dashed red, and the shortest, dotted red. Both columns share the same mean soltion, solid blue, for a given ring gain which is generated by averaging all observed peaks. All columns share temporal axes, and all rows share scaled power axes. Plots along a row are generated from the same time series. Power has been normalized to one.
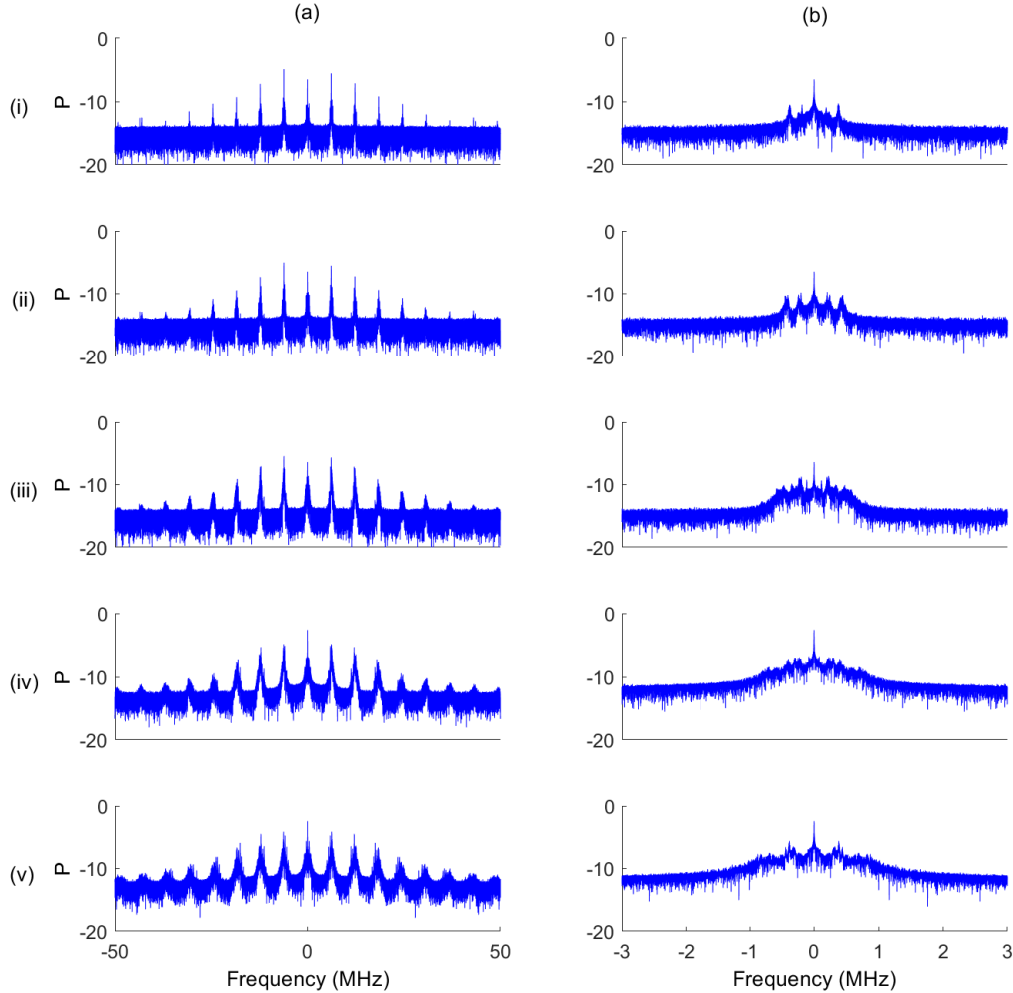
Figure 7.3: Solitary wave train envelope power spectra for increasing ring gain.Overview of observed ring signal power spectrum for increasing gain. Gains increase in steps of 0.25 dB from top to bottom along a column: (i) 2.0 dB, (ii) 2.25 dB, (iii) 2.5 dB, (iv) 2.75 dB and (v) 3.0 dB. Across a single row columns (a) and (b) show the same signal at different frequency scales. As gain increases, down column (a), we note a severe widening of spectral peaks and increasing complexity. Column (b) highlights these effects about the principal peak. These behaviors are indicative of chaotic evolution. All plots in a column share common frequency scales All plots share amplitude scales. Plots along a row are generated from the same time series and frequencies are reported relative to the carrier wave frequency.

now seek to quantify the chaotic nature of the time series following the methodology laid out in Chapter 4. We begin by reiterating that the results of nonlinear time series analysis are only useful for comparison purposes if produced from the same underlying method and assumptions. All analysis presented in this section will use the full observed timeseries and not the reconstructed envelope. As discussed above, distortions in the underlying bright soliton train at gains above 2.25 dB indicate that significant information on evolution is present at the resolution of single round trips, including deformation of the underlying bright solitary train, and should not be ignored. Further, at gains above 2.5 dB reconstructing an envelope is entirely nontrivial and would ignore the presence of multiple solitary waves. The time delay parameter will be chosen as the first minimum of the mutual information, and verified with the C-C method and visual inspection. The time delay window will not be used during calculations of the correlation sum. This procedure stands in contrast to the methodology used in the PRL [31] where chaos was quantified solely within the envelope and estimated using a time delay window correlation sum. This choice reflects the inclusion of higher gains in the analysis and the authors belief that the presented methodology includes fewer assumptions and is less prone to mis-characterization. A detailed work through of the quantification of the correlation dimension for a ring gain of 3.0 dB is shown in Chapter 4. Table Table 7.1 shows estimations of the correlation dimension for all ring gains, including error bars and the R^2 values from each individual fit. The number of dimensions and time delay used as well as the length of the linear fitting region (out of a possible 500 ϵ bins) are likewise included.

Table 7.1: A summary of correlation results for all measured ring gains.

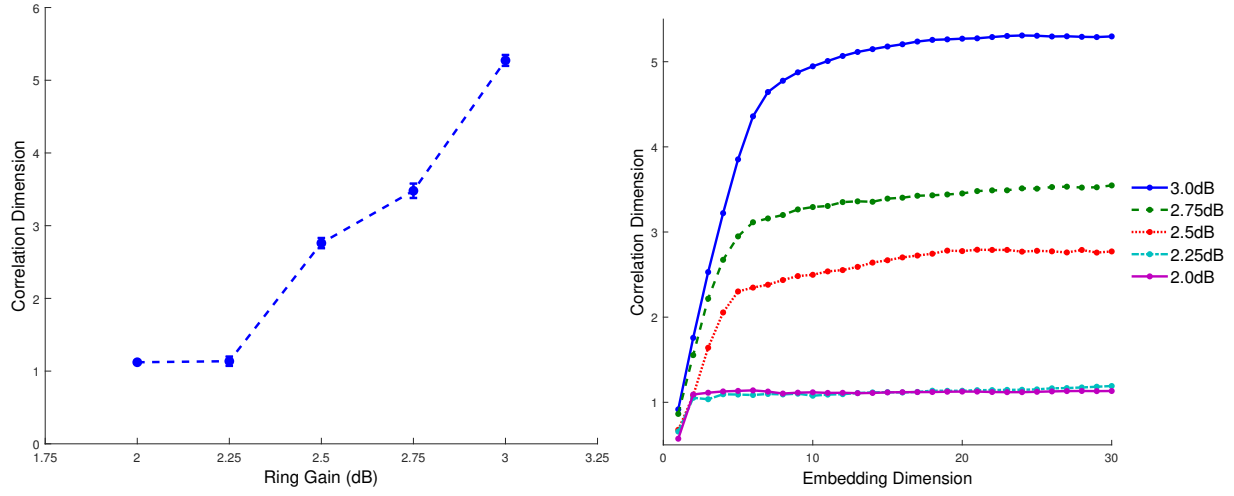| Gain(dB)	τ	$D_2 \pm 2\sigma_{D_2}$	$R^2 \pm 2\sigma_{R^2}$	M_{range}	ϵ_{max}
2.00	22	1.122±0.018	0.999±4e^{-4}	5 to 30	60
2.25	24	1.136±0.064	0.999±5e^{-5}	10 to 30	50
2.50	16	2.761±0.070	0.999±4e^{-4}	15 to 30	40
2.75	13	3.480±0.099	0.999±5e^{-4}	15 to 30	40
3.00	13	5.273±0.075	0.999±1e^{-4}	15 to 30	70

Figure 7.4: Chaotic Soliton Correlation Dimension. (a) Estmates of correlation dimension with increasing ring gain showing saturation as a function of embedding dimension. (b) Correlation dimension vs ring gain including error estimates. Evidence of regime chance at 2.5 dB is evident with the shift in correlation dimension.

7.2   Simulating the Iterative Model

Motivated by the results above we seek to develop and evaluate an iterative numerical model of spin wave envelope solitons in magnetic thin film-based feedback rings. We numerically investigate the cubic-quintic complex Ginzburg-Landau equation, a model which has previously demonstrated predicted and descriptive power when evaluated in a continuum approximation. The model, given originally in Equation 3.15, is restated here for clarity.

$$i\frac{\partial u}{\partial t} = \left[-\frac{D}{2}\frac{\partial^2}{\partial x^2} + iL + (N + iC)|u|^2 + (S + iQ)|u|^4 \right] u \tag{7.1}$$

where $u = u(x, t)$ is a dimensionless complex magnetization amplitude defined as $|u(x,t)|^2 = \mathbf{m}(x,t)^2/2\mathbf{M_s}^2$; here $\mathbf{m}(x,t)$ is the dynamic magnetization while $\mathbf{M_s}^2$ is the saturation magnetization; D is the dispersion coefficient; N and S are the cubic and quintic nonlinearity coefficients, respectively; t is the 'temporal' evolution coordinate; x is the 'spatial' coordinate of propagation boosted to the group velocity of the solitary wave envelope; and L, C, and Q are the linear, cubic, and quintic gains (losses) if positive (negative). All parameters are taken to be real as the complex nature of the coefficients is explicitly accounted for in Equa-

tion 7.1. The local intensity of the magnetization amplitude is given by $|u(x,t)|^2$. The norm and energy at a given time, t, are defined as

$$\|u(t)\|_2 = \int_0^L \mathrm{d}x \; |u(x,t)|^2,$$ (7.2)

and

$$E(t) = \int_0^L \mathrm{d}x \; \left[\frac{D}{2} \left| \frac{\partial u(x,t)}{\partial x} \right|^2 + (N + S|u(x,t)|^2)|u(x,t)|^2 \right],$$ (7.3)

respectively, where the integrals are taken over the length or circumference, $2\pi R$, of the feedback ring. All norms, intensities and energies given within figures are scaled by $\|u(0)\|_2$, $\max[|u(x,0)|^2]$ and $\mathrm{abs}[E(0)]$ respectively where $t = 0$ corresponds to the initial condition used during numerical simulation. Numerical values given within the text are not scaled. The specific choice of initial condition will be discussed later in this section. A thorough discussion of the GLNLS and its application to spin wave dynamics in active magnetic feedback rings may be found in a previous exploratory and experimental chapters [33, 34].

Earlier numerical investigations of the GLNLS ignored the periodic nature of amplification and losses present within active magnetic feedback rings in favor of investigating dynamical patterns on scales much longer than a single round trip. The numerical work presented here, as previously discussed, will explicitly account for both the instantaneous periodic linear amplification present within the electronic feedback loop and the sustained losses experienced by spin waves propagating through a nonlinear, dispersive YIG waveguide. This is accomplished numerically via a renormalization of the wavefunction, $u(x,t)$, every M timesteps such that $|u(T_{n(M+1)})|^2 = \alpha e^{2LM}|u(T_n M_n)|^2$ where α is a renormalization constant and M_n corresponds to the nth round trip around the feedback ring. The renormalization constant is defined such that $\alpha = 1$ corresponds to a direct compensation of the linear loss experienced by a bright solitary over a single round trip, given explicitly as e^{-2LM}. We note that choice of $\alpha > 1$ ($\alpha < 1$) will be numerically unstable without the presence of non-zero nonlinear loss (gain) terms in the GLNLS. We further define a special case of $\alpha = 0$ such that $|u(nM)|^2 = |u(0)|^2$ for any n, corresponding to an enforced conservation of the norm

146

regardless of which loss/gain terms are active within the GLNLS. In the absence of nonlinear terms $\alpha = 1$ and $\alpha = 0$ represent the same periodic renormalization scheme.

We identify four potential numerical schemes, listed in order of increasing computational complexity, which mimic the experimental increasing of ring gain:

1. In a forced conservation regime, $\alpha = 0$, losses, L, C and Q, are increased.

2. Using forced conservation dispersion, D, is increased at fixed losses.

3. Under forced conservation and fixed GLNLS parameters the initial condition amplitude, $|u(T_0)|^2$, is increased.

4. With fixed losses the renormalization constant, α is increased incrementally.

The work presented here will explore the simplest numerical scheme (1) with only linear loss, L, active. We considered increasing linear losses, under forced conservation, from zero to the value corresponding to a five order of magnitude decrease in the norm of the magnetization wavefunction per round trip. The latter value was chosen explicitly as an excessively high limit. As linear loss is increased the effective relative magnitudes of dispersion and nonlinearity within the GLNLS, see Equation 7.1, will change dramatically over a single round trip. This may drives dynamical behaviors not observable in the continuum approximation.

Numerical scheme (2) could be viable as dispersion has been previously posited to increase with ring gain in active feedback rings [25]. Dispersion jumps and ramps are a well studied driver of dynamical wave behaviors including fractal development. Scheme (3) mimics increasing ring gain via an increased initial condition amplitude in the simpler numerical environment of forced conservation. The most directly physically analogous scheme, (4), involves eight free parameters $(L,C,Q,D,N,\alpha,|u(T_0)|^2,M)$ and may only be considered in extremely limited contexts where the parameter space is reduced via direct fitting to experimental results. A general evaluation of scheme (4) is not realistic owing to finite time and computational resources.

All simulations of the CQCGL were performed using adaptive time step Cash-Karp Runge-Kutta for temporal evolution and pseudospectral techniques for spatial propagation as discussed in Chapter 4. Periodic boundary conditions were used to numerically mimic propagation around a ring. Note, a complete discussion on numerical convergence for complex dynamics may be found in chapters 4 and 5. Each simulation began as a bright soliton initial condition obtained via imaginary time relaxation [102], the ground state solution to the GLNLS with S, L, C, and Q set as zero, with $|u(x,t)|^2 < 1$. This IC corresponds experimentally with a stable bright soliton circling within a YIG strip-based active feedback ring. This solution is analogous to a soliton train. Dynamical results were generated by driving this bright soliton initial condition out of equilibrium via numerical propagation under the influences of non-zero gain or loss terms and periodic renormalization under scheme (1) above. This is a process analogous to active feedback ring experiments where gains are increased beyond those which support stable bright soliton trains [14, 23, 25, 31, 103].

Experimentally a time series is recorded at the detection transducer with the full waveform being captured once a round trip after the signal has propagated a length d between the transducers and passed through the electronics loop. The length of the ring therefore, ℓ, is taken to be the transducer separation, d, as the propagation delay is orders of magnitude smaller than the round trip time, $T_e < T$. Simulations explicitly model the entire feedback loop at the group velocity of the waveform. A time series may be reconstructed from numerical data by concatenating the simulated waveform after a temporal evolution of T or a spatial evolution of $d = \ell$. In this work we adopt the former convention to ease the direct comparison of simulations to the power vs. time data often observed experimentally for spin waves in magnetic thin films. Such a reconstructed time series is labeled $u_{ts}(t)$ throughout the chapter. A time series of solitary wave peak intensity at successive round trips is also useful in studying modulating single solitary wave trains and is defined by

$$|u_{peak}(t)|^2 = |\max[u(x, nT)]|^2, \; n = 0, 1, ..., N_{RT}, \tag{7.4}$$

where T is the round trip time and N_{RT} is the total number of round trips.

Physical GLNLS parameter values are obtained by fitting this initial condition to experimentally observed bright soliton train conditions. This choice of units also fixes the ratio of N/D used in generating initial conditions, while the amplitude of N and D dictate the simulation timescale. We assumed that the dimensionless spin wave intensity is directly proportional to the spin wave power, $|u(x,t)|^2 \propto P_{\text{out}}$, as experimental measurements of voltage are taken across a diode with quadratic behavior and are generally taken to be proportional to power. Values typical for a soliton fractal experiment are $T = 165$ ns, the round trip time; $d = 0.55$ cm, the transducer separation; $T_{\text{e}} = 10$ ns, the electronic loop propagation time; $V_{\text{g}} = d/(T - T_{\text{e}}) = 3.5 \times 10^6$ cm/s, the group velocity; $N = -9.24 \times 10^9$ rad/s, the cubic nonlinearity; and $D = 510$ cm^2/s, the dispersion. Using these parameters one finds $[t] \approx 25$ ns where t is the scaled temporal unit used in simulations. This relation may be used to immediately transform code values for L, C, Q and S, which share units of inverse time, to physical values. For example the largest studied linear loss is $L = t^{-1} \approx 0.1 \, \text{ns}^{-1}$ which matches the order of experimentally approximated linear losses for magnetostatic backward volume spin waves in YIG thin films [103]. Active feedback ring experiments indicate that nonlinearity and dispersion are the dominant sources of envelope shaping for chaotic spin wave solitons and that the losses present in the ring are fully compensated for by the amplifier. This imposed an important constraint on modeling: the coefficients N and D should be orders of magnitude larger than losses, L, C, and Q.

Over 111k node hours were used to execute over 6000 unique numerical simulations and convergence studies generating 2.5 TB of data. The analysis of this data is presented in the following sections where we examine two mechanisms for generating increasing solitary wave complexity and ultimately identify soliton fractals.

7.2.1 Complex Wave Dynamics

Four distinct dynamical regimes were identified for bright solitary waves evolved under enforced conservation at fixed dispersion (linear loss) as spin wave power was increased:

1. Periodic Beating: The domination of a single principle eigenmode such that the solitonic train nature of the signal is either not fully developed, or drowned out.

2. Multi-Periodic Modulation: The modulation of the soliton train envelope by one or more non-commensurate frequencies of equal power.

3. Periodic Modulation: The modulation of the soliton train envelope by one or more commensurate frequencies.

4. Higher Order Solitons: 2nd order and higher order solitons are reached at sufficient spin wave power.
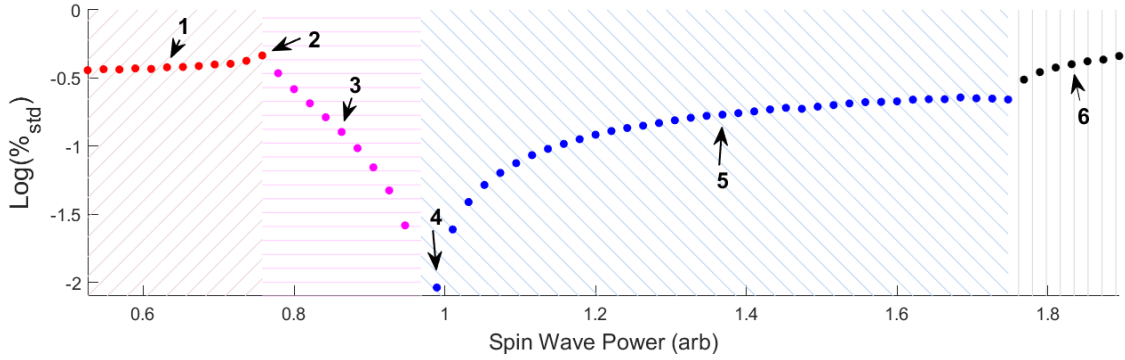
Figure 7.5: Regions of distinct solitary wave dynamics with increasing ring gan. Percent envelope modulation, defined in Equation 7.5, shows four distinct dynamical regions as spin wave power is increased within the ring. The regions are identified from left to right as breathing (red, forward hatch), multiperiodic modulation (magenta, flat hatch), period modulation (blue, back hatch) and 2nd order dynamics (black, vertical hatch).

These regions are shown in Figure 7.5, which shows the percent modulation, in log scale, of the solitary wave envelope (defined as the maximum spin wave power within the ring for each round trip). If E_n is the spin wave envelope at round trip n then the percent modulation is defined as

$$\%_{std} = \text{Log}\left(\frac{\text{stdev}\left(\{E_i\}\right)}{\text{mean}\left(\{E_i\}\right)}\right). \tag{7.5}$$

The percent modulation does not provide for the unique identification of solitary wave dynamics, but its trends strongly identify regions of dynamical behavior. The transitions

between dynamical regions is indicated by discontinuities in the curve. In the language of dynamical systems Figure 7.5 is often referred to as a bifurcation diagram, a figure which shows the qualitative changes in dynamical behaviors as one smoothly adjusts a system parameter (a bifurcation). The parameter being adjusted here, linear loss, impacts not only the amplitude of the periodic renormalization but also introduces a time dependence to the effective strength of the local nonlinearity. Adjustments to spin wave power may also directly impact the effects or presence of three and wave mixing on dynamics, which can result in effective modifications to multiple parameters in the GLNLS. The global and systemic effects of this parameter as well as our fundamental lack of knowledge on the underlying phase space of the system prevents any serious attempts at classifying the nature of these bifurcations. Our choice of language for these dynamical regimes is intentional, as we wish to focus on the distinct dynamical behaviors identifiable in these regions, rather than imply any formal application of bifurcation theory.

The results presented here will explore the simplest numerical schemes (1) with only linear loss, L, active. We considered increasing linear losses, under forced conservation, from zero to the value corresponding to a five order of magnitude decrease in the norm of the magnetization wavefunction over a single round trip. The latter value was chosen explicitly as an excessively high limit.

A strong correlation exists between the effects of dispersion and linear loss under enforced conservation. The same progression of dynamical behaviors may be observed by either increasing linear loss or linear gain. Figure 7.5 shows a semilog % standard deviation curve as linear loss is increased at a fixed dispersion. The plot illustrates the sharp transitions at the dynamical behavior boundaries. Examples of each dynamical behavior are shown in Figure 7.6, with their relative positions on the loss vs % standard deviation plot being indicated by their subplot number.

This relationship was further established by a study of 1315 simulations which explored 40 distinct dispersion values. By isolating the location of the false plateau as a function of
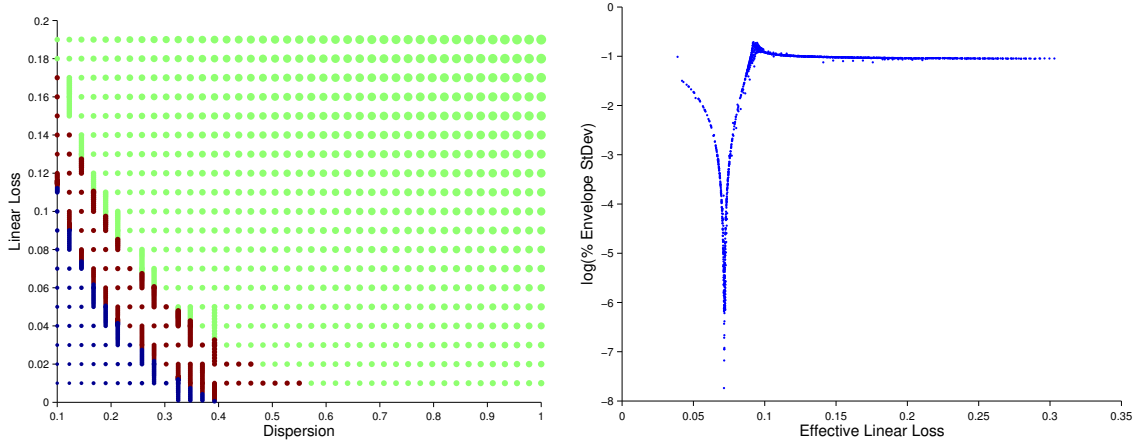
151

Figure 7.6: Examples of numerically identified behaviors in the iterative model Each of the dynamical regions shown in Figure 7.5. In each case the top plot is the spin wave envelope, and the bottom plot is a spatiotemporal plot of spin wave power over the same round trips. Of particular interest is example (4), which demonstrates a stable soliton train under periodic amplification and loss.

L and D a direction relationship was found for an effective loss:

$$L_{ef} = (-L + 0.11303)\sqrt{D}, \tag{7.6}$$

where L and D are the linear loss and dispersion as given in the GLNLS, 7.1, and L_{ef} is the new effective loss. The false plateau transition was found to occur at $L_{ef} = 0.0714$ and the transition from multi-periodic modulation to beating occurs at $L_{ef} = 0.0917$. The family of curves created at fixed L_{ef} and varied D, L are expected to be statistically identical outside of a rescaling of $|u_0|^2$ and M.

The dynamical regions identified are shown in Figure 7.6 and are, from left to right, (1) breathing, (3) multiperiodic modulation, (5) periodic modulation, (6) 2nd modulation. The dynamics identified in Figure 7.6 as (2) and (4) are the transition from breathing to multiperiodic modulation and a no-modulation solution, respectively. Each dynamic is shown in Figure 7.6 according to their label in Figure 7.5 and contain two plots. The top plot is the spin wave envelope, E_n, and the bottom plot is a spatiotemporal plot of the same round trips. One can easily observe the multiperiodic and periodic modulation in the spin wave envelope plots of (3) and (5). Also of note is the characteristic 2nd order soliton modulations

in the spin wave envelope plots of (6), with peak modulations of over 50%.

Of particular interest is dynamic (4), which is a stable soliton train existing in an environment of sustained loss and periodic amplification. Further investigation has shown that for any given choice of D, N and L there exists a bright soliton solution given by,

$$u(x,t) = \frac{1}{2}\sqrt{\frac{-N}{D_0}}\text{Sech}\left(\frac{1}{2}\frac{-N}{D_0}x\right)\exp^{it\omega}, \tag{7.7}$$

so long as $D_0 > D$, or equivalently that $N_0 < N$. We note this is the ground state solution to the CCQGL equation with no loss terms, and a normalization of 1. We may further generalize this solution to

$$u(x,t) = u_0\frac{1}{2}\sqrt{\frac{-N}{D_0}}\text{Sech}\left(w_0\frac{1}{2}\frac{-N}{D_0}x\right)\exp^{it\omega}, \tag{7.8}$$

and identify a family of solutions as long as we do not impose a normalization constraint of 1. This generalization allows us to systematically increase soliton width while holding soliton height constant in a way which may be rescaled from the CCQGL.

We note that the solution given by Equation 7.7 is a bright soliton solution which is wider and shorter than the one we would expect to propagate through our lossy system with parameters D, N, and L. We find that the presence of linear loss and a periodic amplification acts to compensate the system's lack of dispersion directly. Indeed for fixed D_0 we can identify a linear loss, L, which produces the no-modulation solution for any $0 < D < D_0$. A general solution for any D_0 and N is being sought. We also suspect a family of no-modulation curves exists if one varies u_0 and w_0 within Equation 7.8. The solution given by Equation 7.7 is unique as long as one imposes a normalization condition.

7.2.2 Spectral Fractals

The identification of the false plateau, discussed in section Section 7.2.1, enables the study of spin wave dynamics on active feedback rings using a novel initial condition in which the periodic nature of the amplification and the sustained film losses are explicitly accounted for. Previous numerical works which examine perturbing bright soliton trains out

of equilibrium, which has been done experimentally in the observation of chaotic solitons and soltion fractals, used the ground state bright soliton solution of the NLS as a starting point. The false plateau provides a bright soliton train initial condition which is explicitly grounded in the underlying dynamics of active feedback rings. Presented here are the first numerical results using the false plateau initial condition, which enabled the characterization of a perturbation scheme to generate soliton fractals.

Experimentally a stable soliton train is established by tuning ring gain until a single bright soliton circulates the ring. This initial stage is shown experimentally and numerically in Figure 7.7 in the left and right figures, respectively. Dynamics at the envelope, train and single round trip scales are shown as one moves down a column. The ring gain is then increased until the power level reaches a critical threshold, given by $2 \times |U_0|^2$ and a 2nd order soliton is generated within the feedback ring. This dynamic is characterized by a periodic modulation of the envelope intensity with an amplitude of 0.5 of the normalized power. The ring gain needed to produce this behavior is significantly higher than that used to generate the false plateau. Finally the ring gain is increased slightly, yielding a second order modulation on the original periodic modulation. These stages are evident in the central and right columns of both subplots in Figure 7.7.

Numerically we may immediately identify the false plateau by solving for the appropriate L_{eq}, and the second order soliton may be generated by using a sufficiently amplified initial condition. To generate the second order modulations we find two requirements: (1) dispersion must be increased and (2) the magnetization amplitude must be increased. We note that a instantaneous jump in dispersion is not sufficient to generate fractal structure in the spectra, but that linear ramps occurring over $5,000$ to $10,000$ round trips (on the order of ms) produces the desired structure. We find that dispersion ramps on the order of 5% to 10% are sufficient to introduce additional structure. A similar jump in amplitude was also found to be sufficient. Larger jumps in either amplitude or dispersion were too destructive to the underlying dynamic and drove the system out of modulating soliton regimes. The
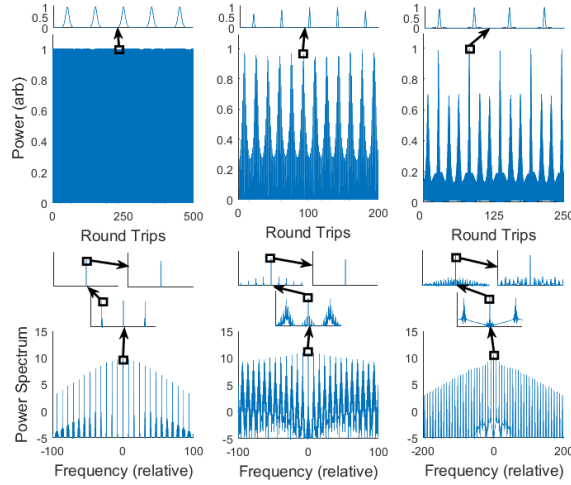
154

Figure 7.7: Numerical generation of soliton fractals. A proposed explanation for the generation of soliton fractals. From left to right we have (1) the no-modulation bright soliton train, (2) the 2nd order soliton, and (3) the grand-daughter fractal. The top figure is a time series for that solution with a inset showing the solitonic nature of the solution. The bottom figure is the powerspectrum with an inlet showing three 10x amplifications of the principle peak. As one moves from left to right the development of soliton fractals is evident.

appropriate ramp values and initial condition is the subject of ongoing work, as the second order modulations so far produced numerically do not quantitatively match the temporal modulations observed experimentally in real space.

Using the no-modulation initial condition defined in Equation 7.7 and Equation 7.8 we were able to quantitatively reproduce soliton fractal breathing using the CCQGL equation under a forced conservation regime, as described earlier. This initial condition is the fractal generator, and is shown in Figure 7.7 (numerical). The daughter is identified as a 2nd order soliton, which can be generated by increasing the amplitude of the initial condition by 200%. The daughter is shown again in Figure 7.7 as the middle column, and may be identified by the periodic modulation of the soliton train with a modulation amplitude of at least 50%. The granddaughter is observed as an additional spatial modulation of the 2nd order soliton. We generate the granddaughter numerically by increasing the initial condition amplitude beyond 200% by an additional $5 - 10\%$ or by increasing the soliton width by a similar amount. The granddaughters are shown again in Figure 7.7 in the right most column.

We note the strong qualitative agreement in the magnitude and period of the additional modulation which shows a 20% modulation from peak power and a period of two 2nd order soliton modulations. This scheme produces prefractal structure in frequency space identical to that observed experimentally.

We note that the presence of periodic amplification was necessary to produce second order prefractal structure in frequency space. Perturbing a 2nd order bright soliton within a conservative NLS did not replicate these results. We also note that increasing the amplitude of the initial condition is equivalent to a rescaling to a lower dispersion within a conservative NLS. The increase of dispersion with increasing ring gain is posited to counteract this effect, allowing the formation of 2nd order solitons at amplitudes lower than 200% of that observed at the false plateau. Experimentally we observed an increase of 154% between false plateau and the periodic modulation, whereas an amplitude increase of only 115% was observed between first and second order modulation [25].

CHAPTER 8

CONCLUSIONS

We reported on the development, implementation and experimental verification of a model for studying the complex dynamical behaviors exhibited by spin wave envelope solitary waves in active magnetic thin film-based feedback rings. This model was numerically evaluated under two distinct schemes corresponding to: (1) continuum approximation where forces acting on the SWEs was taken to be averaged over many round trips; and (2) an iterative approach where each round trip was explicitly modeled.

Initial numerical work under the continuum approximation identified nine dynamical behaviors including four distinct examples of dynamical pattern formation. Until that work no one had predicted long time dynamical behaviors at all, or explained previously observed long time complex soliton wave train modulations.

The clean experimental realization of these four numerically predicted classes of dynamical pattern formations was then demonstrated for bright solitary waves. We highlight that the above numerical exploration involved an extraordinarily broad parameter space search which spanned a minimum of *seven orders of magnitude* for linear, cubic and quintic gain/loss terms and *five orders of magnitude* for an additional quintic nonlinearity. It is indeed remarkable that we experimentally realized each of those predicted classes of dynamical pattern formation.

We further reported on the first experimental observation of the self-generation of dark solitary waves under attractive nonlinearity, and the first known observation of long lifetime dynamical pattern formation for the same. Dark solitary waves are traditionally believed to occur only for defocusing, or repulsive nonlinearity. We note that it is also possible to observe dark solitary waves in spin wave systems with attractive nonlinearity if one injects carefully tuned carrier wave signals. Our work has shown that a wide variety of dark soliton

behaviors appear organically via self-generation for purely attractive nonlinearity without any external potential and without any external sources.

Finally, motivated by the destruction of the underlying stable bright solitary wave train for chaotically modulating solitons at high gain we developed and evaluated a numerical scheme for the CQCGL equation which explicitly modeled each round trip. Analysis of this model yielded a robust solution for the location of a stable bright solitary wave train for any given level of ring dispersion and linear loss. This solution class was used to propose a mechanism for the development of bright soliton fractals.

We highlight that most common and widely used model in the literature for these sorts of phenomena, the nonlinear Schrödinger equation, failed to describe fractals, dynamical pattern formation, multi-periodic solitons, and many other emergent behaviors in spin waves with gain and loss. Further, the vast literature on nonlinear optics and nonlinear hydrodynamics have not produced a viable model for the behaviors we have observed and predicted in the gain-loss context. Most literature in these fields was previously focused on conservative systems, in particular the nonlinear Schrodinger equation, Korteweg-de Vries equation, and sine-Gordon equation. Here we have shown that stable and long-term dynamical pattern formation ranging from multi-periodic solitons to intermittency to chaos and strange attractors after transients die away, are well-described by the relatively simple cubic-quintic complex Ginzburg-Landau equation.

Thus we have established a new nonlinear paradigm and demonstrated that experiments spanning numerous physical system may be well served to make use make use of this simple model, including e.g. Bose-Einstein condensates with attractive interactions, where a host of models in the literature have proven unable to match experiments. Additionally, our experimental verification of these dynamical regimes show that such ideas are not simply theoretical but in fact occur in the real physical world and are observable in an approachable, tunable spin wave system which matches the conditions of many other real-world physical systems.

Our research argues for the use of the CQCGL and AFRs as approachable toy systems for the study of fundamental nonlinear dynamics with broad applications across numerous distinct fields of physics. This includes important open questions such as the possible extension of Kolmogorov-Arnold-Moser theory into open systems. The CQCGL has been totally vindicated as a model for complex dynamical behaviors in such systems, and therefore provides a suitable model for examining the effects of perturbing away from integrability for several distinct forms of gain and loss. The CQCGL and AFRs also provide a means to study these fundamental questions in quasi-conservative regimes where perhaps integrability, in average sense, is preserved.

More approachable areas for additional research include: (1) Numerical explorations of the CQCGL under repulsive nonlinearity, and more generally, the explanation and simulation of dark solitary dynamics under both repulsive and attractive nonlinearities. There is no reason not to expect cross-over effects such as dark solitary wave fractals and chaotic dark solitons. (2) Analaytical (or numerical) work to see if the robust location of stable bright soliton trains under arbitrary dispersion and linear loss for the iterative model can be expressed in terms only fundamental and scaling units. (3) Further exploration of the iterative model to see if higher-order chaotically modulating soliton can be identified numerically and tuned via ring gain. (4) Further experimental explorations of solitary wave dynamics in regimes where three-wave mixing is not forbidden. (5) Numerical and experimental identification of complex dynamical behaviors for forward volume spin waves where the signs of dispersion and nonlinearity are reversed. The interactions of those forces with gains and losses may provide novel examples. (6) Evalutions of the iterative model under forced conservation with nonlinear losses. (7) Collaborations with groups studying analog systems to experimentally identify predicted dynamical behaviors.

REFERENCES CITED

[1] C Sulem and P L Sulem, editors. *The Nonlinear Schrödinger Equation: Self-Focusing and Wave Collapse*. Springer New York, 2004. doi: 10.1007/b98958.

[2] D. D. Stancil and A. Prabhakar. *Spin Waves: Theory and Applications*. Springer, 2009.

[3] Pavol Krivosik and Carl E. Patton. Hamiltonian formulation of nonlinear spin-wave dynamics: Theory and applications. *Physical Review B - Condensed Matter and Materials Physics*, 82(18):184428, 2010. ISSN 10980121. doi: 10.1103/PhysRevB.82.184428.

[4] A. N. Slavin and I. V. Rojdestvenski. 'Bright' and 'dark' spin wave envelope solitons in magnetic films. *Ieee Transactions on Magnetics*, 30(1):37–45, 1994. ISSN 00189464. doi: 10.1109/20.272513.

[5] Mark M. Scott, Mikhail P. Kostylev, Boris A. Kalinikos, and Carl E. Patton. Excitation of bright and dark envelope solitons for magnetostatic waves with attractive nonlinearity. *Physical Review B - Condensed Matter and Materials Physics*, 71(17): 174440, 2005. ISSN 10980121. doi: 10.1103/PhysRevB.71.174440.

[6] M. P. Kostylev. Self-generation of bright spin-wave envelope solitons in active ferromagnetic-film rings. *Journal of Communications Technology and Electronics*, 50 (3):313–320, 2005. ISSN 10642269.

[7] Boris A. Kalinikos, Nikolai G. Kovshikov, and Carl E. Patton. Excitation of bright and dark microwave magnetic envelope solitons in a resonant ring. *Applied Physics Letters*, 75(2):265–267, 1999. ISSN 00036951. doi: 10.1063/1.124343.

[8] N. Kovshikov, B. Kalinikos, C. Patton, E. Wright, and J. Nash. Formation, propagation, reflection, and collision of microwave envelope solitons in yttrium iron garnet films. *Physical Review B - Condensed Matter and Materials Physics*, 54(21):15210–15223, 1996. ISSN 1550235X. doi: 10.1103/PhysRevB.54.15210.

[9] Boris A. Kalinikos, Mark M. Scott, and Carl E. Patton. Self-generation of fundamental dark solitons in magnetic films. *Physical Review Letters*, 84(20):4697–4700, 2000. ISSN 10797114. doi: 10.1103/PhysRevLett.84.4697.

[10] B. A. Kalinikos, N. G. Kovshikov, and A. N. Slavin. Envelope solitons of highly dispersive and low dispersive spin waves in magnetic films (invited). *Journal of Applied Physics*, 69(8):5712–5717, 1991. ISSN 00218979. doi: 10.1063/1.347896.

[11] B. A. Kalinikos, N. G. Kovshikov, and A. N. Slavin. Experimental observation of magnetostatic wave envelope solitons in yttrium iron garnet films. *Physical Review B*, 42(13):8658–8660, 1990. ISSN 01631829. doi: 10.1103/PhysRevB.42.8658.

[12] B. A. Kalinikos, N. G. Kovshikov, and A. N. Slavin. Spin-wave envelope solitons in thin ferromagnetic films (invited). *Journal of Applied Physics*, 67(9):5633–5638, 1990. ISSN 00218979. doi: 10.1063/1.345909.

[13] Ming Chen, Mincho A. Tsankov, Jon M. Nash, and Carl E. Patton. Backward-volume-wave microwave-envelope solitons in yttrium iron garnet films. *Physical Review B*, 49 (18):12773–12790, 1994. ISSN 0163-1829. doi: 10.1103/PhysRevB.49.12773.

[14] B. A. Kalinikos, N. G. Kovshikov, and C. E. Patton. Observation of self-generation of dark envelope solitons for spin waves in ferromagnetic films. *Jetp Letters*, 68(3): 243–247, 1998. ISSN 00213640. doi: 10.1134/1.567853.

[15] B. A. Kalinikos, N. G. Kovshikov, and A. N. Slavin. Effect of magnetic dissipation on propagation of dipole spin-wave envelope solitons in Yttrium-Iron-Garnet films. *IEEE Transactions on Magnetics*, 28(5, Part 2):3207–3209, 1992. ISSN 0018-9464. doi: 10.1109/20.179760.

[16] H. Benner, B. A. Kalinikos, N. G. Kovshikov, and M. P. Kostylev. Observation of spin-wave envelope dark solitons in ferromagnetic films. *Jetp Letters*, 72(4):306–311, 2000. ISSN 00213640. doi: 10.1134/1.1320116.

[17] A. N. Slavin and H. Benner. Formation and propagation of spin-wave envelope solitons in weakly dissipative ferrite waveguides. *Physical Review B - Condensed Matter and Materials Physics*, 67(17):174421, 2003. ISSN 1550235X. doi: 10.1103/PhysRevB.67. 174421.

[18] A. D. Boardman, S. A. Nikitov, K. Xie, and H. Mehta. Bright magnetostatic spin-wave envelope solitons in ferromagnetic films. *Journal of Magnetism and Magnetic Materials*, 145(3):357–378, 1995. ISSN 03048853. doi: 10.1016/0304-8853(94)01624-0.

[19] B. A. Kalinikos, N. G. Kovshikov, M. P. Kostylev, and H. Benner. Self-Generation of Spin-Wave Envelope Soliton Trains with Different Periods. *Jetp Letters*, 76(5):253–257, 2002. ISSN 00213640. doi: 10.1134/1.1520616.

[20] Mingzhong Wu, Boris A. Kalinikos, and Carl E. Patton. Generation of dark and bright spin wave envelope soliton trains through self-modulational instability in magnetic films. *Physical Review Letters*, 93(15):157207, 2004. ISSN 00319007. doi: 10.1103/ PhysRevLett.93.157207.

[21] Boris A. Kalinikos, Nikolai G. Kovshikov, and Carl E. Patton. Self-generation of microwave magnetic envelope soliton trains in yttrium iron garnet thin films. *Physical Review Letters*, 80(19):4301–4304, 1998. ISSN 10797114. doi: 10.1103/PhysRevLett. 80.4301.

[22] Sergej O. Demokritov, Alexander A. Serga, Vladislav E. Demidov, Burkard Hillebrands, Michail P. Kostylev, and Boris A. Kalinikos. Experimental observation of symmetry-breaking nonlinear modes in an active ring. *Nature*, 426(6963):159–162, 2003. ISSN 00280836. doi: 10.1038/nature02042.

[23] Mingzhong Wu and Carl E. Patton. Experimental observation of fermi-pasta-ulam recurrence in a nonlinear feedback ring system. *Physical Review Letters*, 98(4):47202, 2007. ISSN 00319007. doi: 10.1103/PhysRevLett.98.047202.

[24] Mark M. Scott, Boris A. Kalinikos, and Carl E. Patton. Spatial recurrence for nonlinear magnetostatic wave excitations. *Journal of Applied Physics*, 94(9):5877–5880, 2003. ISSN 00218979. doi: 10.1063/1.1615297.

[25] Mingzhong Wu, Boris A. Kalinikos, Lincoln D. Carr, and Carl E. Patton. Observation of spin-wave soliton fractals in magnetic film active feedback rings. *Physical Review Letters*, 96(18):187202, 2006. ISSN 00319007. doi: 10.1103/PhysRevLett.96.187202.

[26] Mingzhong Wu, Pavol Krivosik, Boris A. Kalinikos, and Carl E. Patton. Random generation of coherent solitary waves from incoherent waves. *Physical Review Letters*, 96(22):227202, 2006. ISSN 00319007. doi: 10.1103/PhysRevLett.96.227202.

[27] Mingzhong Wu, Boris A. Kalinikos, and Carl E. Patton. Self-generation of chaotic solitary spin wave pulses in magnetic film active feedback rings. *Physical Review Letters*, 95(23):237202, 2005. ISSN 00319007. doi: 10.1103/PhysRevLett.95.237202.

[28] Aaron M. Hagerstrom, Wei Tong, Mingzhong Wu, Boris A. Kalinikos, and Richard Eykholt. Excitation of chaotic spin waves in magnetic film feedback rings through three-wave nonlinear interactions. *Physical Review Letters*, 102(20):207202, 2009. ISSN 00319007. doi: 10.1103/PhysRevLett.102.207202.

[29] A. V. Kondrashov, A. B. Ustinov, B. A. Kalinikos, and H. Benner. Chaotic microwave self-generation in active rings based on ferromagnetic films. *Technical Physics Letters*, 34(6):492–494, 2008. ISSN 10637850. doi: 10.1134/S1063785008060126.

[30] Mingzhong Wu, Michael A. Kraemer, Mark M. Scott, Carl E. Patton, and Boris A. Kalinikos. Spatial evolution of multipeaked microwave magnetic envelope solitons in yttrium iron garnet thin films. *Physical Review B - Condensed Matter and Materials Physics*, 70(5):54402, 2004. ISSN 01631829. doi: 10.1103/PhysRevB.70.054402.

[31] Zihui Wang, Aaron Hagerstrom, Justin Q. Anderson, Wei Tong, Mingzhong Wu, Lincoln D. Carr, Richard Eykholt, and Boris A. Kalinikos. Chaotic spin-wave solitons in magnetic film feedback rings. *Physical Review Letters*, 107(11), 2011. ISSN 00319007. doi: 10.1103/PhysRevLett.107.114102.

[32] Alexey B. Ustinov, Vladislav E. Demidov, Alexander V. Kondrashov, Boris A. Kalinikos, and Sergej O. Demokritov. Observation of the chaotic spin-wave soliton trains in magnetic films. *Physical Review Letters*, 106(1):17201, 2011. ISSN 00319007. doi: 10.1103/PhysRevLett.106.017201.

[33] Justin Q. Anderson, P. A. Praveen Janantha, Diego A. Alcala, Wu Mingzhong, and Lincoln D. Carr. Physical realization of complex dynamical pattern formation in magnetic active feedback rings. *Physical Review X [submitted]*, 2020.

[34] Justin Q. Anderson, Rachel A. Ryan, Mingzhong Wu, and Lincoln D. Carr. Complex solitary wave dynamics, pattern formation and chaos in the gain-loss nonlinear Schrödinger equation. *New Journal of Physics*, 16(2):23025, 2014. ISSN 13672630. doi: 10.1088/1367-2630/16/2/023025.

[35] Igor S. Aranson and Lorenz Kramer. The world of the complex Ginzburg-Landau equation. *Reviews of Modern Physics*, 74(1):99–143, 2002. ISSN 00346861. doi: 10.1103/RevModPhys.74.99.

[36] B. A. Kalinikos and A. N. Slavin. Theory of dipole-exchange spin wave spectrum for ferromagnetic films with mixed exchange boundary conditions. *Journal of Physics C: Solid State Physics*, 19(35):7013–7033, 1986. ISSN 00223719. doi: 10.1088/0022-3719/19/35/014.

[37] A. N. Slavin and B. A. Kalinikos. Nonlinear-theory of Spin-waves in Ferromagnetic Films. *Sov. Phys. Tech. Phys.*, 57(12):2387–2389, 1987.

[38] Cristiano Ciuti. Quantum fluids of light. *Conference on Lasers and Electro-optics Europe - Technical Digest*, 2014-January(1):299–366, 2014. doi: 10.1364/cleo_qels.2014.fm3b.1.

[39] L. P. Pitaevskii and S. Stringari. {*Bose-Einstein*} *Condensation*. Int. Ser. Mono. Phys. Clarendon Press, Oxford, 2003.

[40] Lincoln D. Carr, David DeMille, Roman V. Krems, and Jun Ye. Cold and ultracold molecules: Science, technology and applications. *New Journal of Physics*, 11(5):55049, 2009. ISSN 13672630. doi: 10.1088/1367-2630/11/5/055049.

[41] Mingzhong Wu. Nonlinear spin waves in magnetic film feedback rings. In Robert E Camley and Robert L Stamps, editors, *Solid State Physics - Advances in Research and Applications*, volume 62 of *Solid State Physics*, pages 163–224. Academic Press, 2010. doi: 10.1016/B978-0-12-374293-3.00003-1.

[42] M. M. Scott. *Nonlinear Magnetostatic Spin Waves, Induced Modulational Instability and Envelope Solitons*. PhD thesis, Colorado State University, 2002.

[43] Zihui Wang. *Spin Waves in Magnetic Thin Films: New Types of Solitons and Electrical Control*. PhD thesis, Colorado State University, 2017.

[44] Pasdunkorale Arachchige Praveen Janantha. *Nonlinear Spin Waves in Magnetic Thin Films Foldover, Dispersive Shock Waves, and Spin Pumping*. PhD thesis, Colorado State University, 2016.

[45] L. Landau and E. Lifshitz. On the theory of the dispersion of magnetic permeability in ferromagnetic bodies. In *Perspectives in Theoretical Physics*, pages 51–65. Elsevier, 1992. doi: 10.1016/b978-0-08-036364-6.50008-9.

[46] B. A. Kalinikos. Excitation of propagating spin waves in ferromagnetic films. *IEE Proceedings H Microwaves, Optics and Antennas*, 127(1):4–10, 1980. ISSN 0143-7097. doi: 10.1049/ip-h-1.1980.0002.

[47] H. Leblond. Electromagnetic waves in ferromagnets: a Davey-Stewartson-type model. *Journal of Physics a: Mathematical and General*, 32(45):7907–7932, 1999. ISSN 0305-4470. doi: 10.1088/0305-4470/32/45/308.

[48] Mark J. Ablowitz, Gino Biondini, and Lev A. Ostrovsky. Optical solitons: Perspectives and applications. *Chaos*, 10(3):471–474, 2000. ISSN 10541500. doi: 10.1063/1.1310721.

[49] Hermann A. Haus and William S. Wong. Solitons in optical communications. *Reviews of Modern Physics*, 68(2):423–444, 1996. ISSN 00346861. doi: 10.1103/RevModPhys. 68.423.

[50] William H. Press, Saul A. Teukolsky, William T. Vetterling, and Brian P. Flannery. *Numerical Recipes 3rd Edition: The Art of Scientific Computing*. Cambridge University Press, USA, 3 edition, 2007. ISBN 0521880688. doi: 10.5555/1403886.

[51] Victor Snyder. *Quantum Fluctutations in the Dynamics of Bose-Einstein Condensates*. PhD thesis, Colorado School of Mines, 2008.

[52] Henri Poincaré. On the three-body problem and the equations of dynamics. In *History of Modern Physical Sciences*, volume 13, pages 368–376. PUBLISHED BY IMPERIAL COLLEGE PRESS AND DISTRIBUTED BY WORLD SCIENTIFIC PUBLISHING CO., 2003. doi: 10.1142/9781848161337_0018.

[53] Edward N. Lorenz. Deterministic Nonperiodic Flow. *Journal of the Atmospheric Sciences*, 20(2):130–141, 1963. ISSN 1520-0469. doi: 10.1175/1520-0469(1963)020⟨0130: dnf⟩2.0.co;2.

[54] J. Sokol. The hidden heroines of chaos, 2019. URL https://www.quantamagazine.org/hidden-heroines-of-chaos-ellen-fetter-and-margaret-hamilton-20190520/.

[55] Peter Grassberger. Generalized dimensions of strange attractors. *Physics Letters A*, 97(6):227–230, 1983. ISSN 03759601. doi: 10.1016/0375-9601(83)90753-3.

[56] Peter Grassberger and Itamar Procaccia. Characterization of strange attractors. *Physical Review Letters*, 50(5):346–349, 1983. doi: 10.1103/PhysRevLett.50.346.

[57] Peter Grassberger and Itamar Procaccia. Measuring the strangeness of strange attractors. *Physica D: Nonlinear Phenomena*, 9(1-2):189–208, 1983. ISSN 01672789. doi: 10.1016/0167-2789(83)90298-1.

[58] J. P. Eckmann and D. Ruelle. Ergodic theory of chaos and strange attractors. *Reviews of Modern Physics*, 57(3):617–656, 1985. ISSN 00346861. doi: 10.1103/RevModPhys. 57.617.

[59] Tien-Yien Li and James A. Yorke. Period Three Implies Chaos. *The American Mathematical Monthly*, 82(10):985, 1975. ISSN 00029890. doi: 10.2307/2318254.

[60] H. Kantz and T. Schreiber. *Nonlinear Time Series Analysis*. Cambridge Univ Pr, 2004. ISBN 0521529026.

[61] Henk Broer and Floris Takens. *Dynamical Systems and Chaos*. Springer New York, 2011. ISBN 9050411096. doi: 10.1007/978-1-4419-6870-8.

[62] Henry D. I. Abarbanel, Reggie Brown, John J. Sidorowich, and Lev Sh Tsimring. The analysis of observed chaotic data in physical systems. *Reviews of Modern Physics*, 65 (4):1331–1392, 1993. ISSN 00346861. doi: 10.1103/RevModPhys.65.1331.

[63] Luis A. Aguirre and Christophe Letellier. Modeling nonlinear dynamics and chaos: A review. *Mathematical Problems in Engineering*, 2009, 2009. ISSN 1024123X. doi: 10.1155/2009/238960.

[64] H. Whitney. Differentiable manifolds. *Studies in Mathematics and Its Applications*, 3 (C):45–58, 1978. ISSN 01682024. doi: 10.1016/S0168-2024(09)70081-5.

[65] T. Sauer, J. A. Yorke, and M. Casdagli. Embedology. *Journal of Statistical Physics*, 65(3):579–616, 1991. ISSN 0022-4715.

[66] Floris Takens. Detecting strange attractors in turbulence. In *Dynamical systems and turbulence*, pages 366–381. Springer, 1981. doi: 10.1007/bfb0091924.

[67] H. S. Kim, R. Eykholt, and J. D. Salas. Nonlinear dynamics, delay times, and embedding windows. *Physica D: Nonlinear Phenomena*, 127(1-2):48–60, 1999. ISSN 01672789. doi: 10.1016/S0167-2789(98)00240-1.

[68] J. P. Huke and D. S. Broomhead. Embedding theorems for non-uniformly sampled dynamical systems. *Nonlinearity*, 20(9):2205–2244, 2007. ISSN 09517715. doi: 10.1088/0951-7715/20/9/011.

[69] C. J. Cellucci, A. M. Albano, and P. E. Rapp. Comparative study of embedding methods. *Physical Review E - Statistical Physics, Plasmas, Fluids, and Related Interdisciplinary Topics*, 67(6):13, 2003. ISSN 1063651X. doi: 10.1103/PhysRevE.67.066210.

[70] Th Buzug and G. Pfister. Comparison of algorithms calculating optimal embedding parameters for delay time coordinates. *Physica D: Nonlinear Phenomena*, 58(1-4): 127–137, 1992. ISSN 01672789. doi: 10.1016/0167-2789(92)90104-U.

[71] Liangyue Cao. Practical method for determining the minimum embedding dimension of a scalar time series. *Physica D: Nonlinear Phenomena*, 110(1-2):43–50, 1997. ISSN 01672789. doi: 10.1016/S0167-2789(97)00118-8.

[72] Sara P. Garcia and Jonas S. Almeida. Nearest neighbor embedding with different time delays. *Physical Review E - Statistical, Nonlinear, and Soft Matter Physics*, 71(3), 2005. ISSN 15393755. doi: 10.1103/PhysRevE.71.037204.

[73] Detlef Holstein and Holger Kantz. Optimal Markov approximations and generalized embeddings. *Physical Review E - Statistical, Nonlinear, and Soft Matter Physics*, 79 (5), 2009. ISSN 15393755. doi: 10.1103/PhysRevE.79.056202.

[74] Matthew B. Kennel, Reggie Brown, and Henry D. I. Abarbanel. Determining embedding dimension for phase-space reconstruction using a geometrical construction. *Physical Review A*, 45(6):3403–3411, 1992. ISSN 10502947. doi: 10.1103/PhysRevA.45.3403.

[75] W. Liebert and H. G. Schuster. Proper choice of the time delay for the analysis of chaotic time series. *Physics Letters A*, 142(2-3):107–111, 1989. ISSN 03759601. doi: 10.1016/0375-9601(89)90169-2.

[76] Yusuke Manabe and Basabi Chakraborty. A novel approach for estimation of optimal embedding parameters of nonlinear time series by structural learning of neural network. *Neurocomputing*, 70(7-9):1360–1371, 2007. ISSN 09252312. doi: 10.1016/j.neucom. 2006.06.005.

[77] Qing Fang Meng, Yu Hua Peng, and Pei Jun Xue. A new method of determining the optimal embedding dimension based on nonlinear prediction. *Chinese Physics*, 16(5): 1252–1257, 2007. ISSN 10091963. doi: 10.1088/1009-1963/16/5/014.

[78] Michael Small and C. K. Tse. Optimal embedding parameters: A modelling paradigm. *Physica D: Nonlinear Phenomena*, 194(3-4):283–296, 2004. ISSN 01672789. doi: 10. 1016/j.physd.2004.03.006.

[79] Yinggan Tang, Mingyong Cui, Lixiang Li, Haipeng Peng, and Xinping Guan. Parameter identification of time-delay chaotic system using chaotic ant swarm. *Chaos, Solitons and Fractals*, 41(4):2097–2102, 2009. ISSN 09600779. doi: 10.1016/j.chaos.2008.09.044.

[80] Yinggan Tang and Xinping Guan. Parameter estimation of chaotic system with time-delay: A differential evolution approach. *Chaos, Solitons and Fractals*, 42(5):3132–3139, 2009. ISSN 09600779. doi: 10.1016/j.chaos.2009.04.045.

[81] M. Thiel, M. C. Romano, P. L. Read, and J. Kurths. Estimation of dynamical invariants without embedding by recurrence plots. *Chaos*, 14(2):234–243, 2004. ISSN 10541500. doi: 10.1063/1.1667633.

[82] Anastasios A. Tsonis. Reconstructing dynamics from observables: The issue of the delay parameter revisited. *International Journal of Bifurcation and Chaos*, 17(12): 4229–4243, 2007. ISSN 02181274. doi: 10.1142/S0218127407019913.

[83] *Selection of delay time window and delay time in phase space reconstruction*, 2007. IEEE Computer Society. ISBN 0769530729. doi: 10.1109/CIS.2007.207.

[84] K. T. Alligood, T. Sauer, and J. A. Yorke. *Chaos: An Introduction to Dynamical Systems*. Springer Verlag, 1996. ISBN 0387946772. doi: 10.1007/978-81-322-2556-0.

[85] Rainer Hegger, Holger Kantz, and Thomas Schreiber. Practical implementation of nonlinear time series methods: The TISEAN package. *Chaos*, 9(2):413–435, 1999. ISSN 10541500. doi: 10.1063/1.166424.

[86] W. D. Ray, W. A. Brock, D. A. Hsieh, and B. LeBaron. *Nonlinear Dynamics, Chaos and Instability Statistical Theory and Economic Evidence.*, volume 44. The MIT press, 1993. ISBN 0262023296. doi: 10.2307/2584373.

[87] James Theiler. Estimating fractal dimension. *Journal of the Optical Society of America A*, 7(6):1055, 1990. ISSN 1084-7529. doi: 10.1364/josaa.7.001055.

[88] M. J. Ablowitz, Gino Biondini, and Steve Blair. Nonlinear Schrödinger equations with mean terms in nonresonant multidimensional quadratic materials. *Physical Review E - Statistical Physics, Plasmas, Fluids, and Related Interdisciplinary Topics*, 63(4):46605, 2001. ISSN 1063651X. doi: 10.1103/PhysRevE.63.046605.

[89] M. J. Ablowitz, S. A. Ablowitz, and N. Antar. Damping of periodic waves in physically significant wave systems. *Studies in Applied Mathematics*, 121(3):313–335, 2008. ISSN 00222526. doi: 10.1111/j.1467-9590.2008.00419.x.

[90] Mark J. Ablowitz and Theodoros P. Horikis. Pulse dynamics and solitons in mode-locked lasers. *Physical Review A*, 78(1):11802, 2008. ISSN 1050-2947. doi: 10.1103/physreva.78.011802.

[91] Mark J. Ablowitz, Theodoros P. Horikis, and Boaz Ilan. Solitons in dispersion-managed mode-locked lasers. *Physical Review a - Atomic, Molecular, and Optical Physics*, 77(3):33814, 2008. ISSN 10502947. doi: 10.1103/PhysRevA.77.033814.

[92] N. Akhmediev, J. M. Soto-Crespo, and G. Town. Pulsating solitons, chaotic solitons, period doubling, and pulse coexistence in mode-locked lasers: Complex Ginzburg-Landau equation approach. *Physical Review E - Statistical Physics, Plasmas, Fluids, and Related Interdisciplinary Topics*, 63(5):56602, 2001. ISSN 1063651X. doi: 10.1103/PhysRevE.63.056602.

[93] N. Akhmediev and A. Ankiewicz. Dissipative solitons in the complex ginzburg-landau and swift-hohenberg equations. In Nail Akhmediev and Adrian Ankiewicz, editors, *Lecture Notes in Physics*, volume 661 of *Lecture Notes in Physics*, pages 1–17. Springer Berlin Heidelberg, 2005. doi: 10.1007/10928028_1.

[94] N. Akhmediev, J. M. Soto-Crespo, and Ph. Grelu. Dissipative solitons and their interactions. *Pamm*, 7(1):1130301–1130302, 2007. ISSN 16177061. doi: 10.1002/pamm.200700286.

[95] N. Akhmediev and A. Ankiewicz. *Dissipative Solitons: From Optics to Biology and Medicine*, volume 751. Springer, 2008. doi: 10.1007/978-3-540-78217-9.

[96] Nail Akhmediev, Adrian Ankiewicz, José María Soto-Crespo, and Philippe Grelu. Dissipative solitons: Present understanding, applications and new developments. *International Journal of Bifurcation and Chaos*, 19(8):2621–2636, 2009. ISSN 02181274. doi: 10.1142/S0218127409024372.

[97] Eduard N. Tsoy and Nail Akhmediev. Bifurcations from stationary to pulsating solitons in the cubic-quintic complex Ginzburg-Landau equation. *Physics Letters, Section a: General, Atomic and Solid State Physics*, 343(6):417–422, 2005. ISSN 03759601. doi: 10.1016/j.physleta.2005.05.102.

[98] M. N. Zhuravlev and N. V. Ostrovskaya. Dynamics of NLS solitons described by the cubic-quintic Ginzburg-Landau equation. *Journal of Experimental and Theoretical Physics*, 99(2):427–442, 2004. ISSN 10637761. doi: 10.1134/1.1800200.

[99] Y. Kominis, S. Droulias, P. Papagiannis, and K. Hizanidis. Gain-controlled soliton routing in dissipative optical lattices. *Optics Infobase Conference Papers*, 85(6):63801, 2012. ISSN 21622701. doi: 10.1364/anic.2012.jm5a.53.

[100] Yannis Kominis, Panagiotis Papagiannis, and Sotiris Droulias. Dissipative soliton acceleration in nonlinear optical lattices. *Optics Express*, 20(16):18165, 2012. ISSN 1094-4087. doi: 10.1364/oe.20.018165.

[101] H. Leblond. Rigorous derivation of the NLS in magnetic films. *Journal of Physics a: Mathematical and General*, 34(45):9687–9712, 2001. ISSN 03054470. doi: 10.1088/0305-4470/34/45/309.

[102] R. Kosloff and H. Tal-Ezer. A direct relaxation method for calculating eigenfunctions and eigenvalues of the schrödinger equation on a grid. *Chemical Physics Letters*, 127 (3):223–230, 1986. ISSN 00092614. doi: 10.1016/0009-2614(86)80262-7.

[103] Mark M. Scott, Carl E. Patton, Mikhail P. Kostylev, and Boris A. Kalinikos. Nonlinear damping of high-power magnetostatic waves in yttrium-iron-garnet films. *Journal of Applied Physics*, 95(11 I):6294–6301, 2004. ISSN 00218979. doi: 10.1063/1.1699503.

[104] M. C. Cross and P. C. Hohenberg. Pattern formation outside of equilibrium. *Reviews of Modern Physics*, 65(3):851–1112, 1993. ISSN 00346861. doi: 10.1103/RevModPhys. 65.851.

[105] Wei Tong, Mingzhong Wu, Lincoln D. Carr, and Boris A. Kalinikos. Formation of random dark envelope solitons from incoherent waves. *Physical Review Letters*, 104 (3), 2010. ISSN 00319007. doi: 10.1103/PhysRevLett.104.037207.

[106] Akira Hasegawa. An historical review of application of optical solitons for high speed communications. *Chaos*, 10(3):475–485, 2000. ISSN 10541500. doi: 10.1063/1.1286914.

[107] Iraj Sadegh Amiri, Sayed Ehsan Alavi, and Sevia Mahdaliza Idrus. *Soliton coding for secured optical communication link*. Number 9789812871602. Springer Singapore, 2015. doi: 10.1007/978-981-287-161-9.

[108] S. A. Nikitov, D. V. Kalyabin, I. V. Lisenkov, A. Slavin, Yu N. Barabanenkov, S. A. Osokin, A. V. Sadovnikov, E. N. Beginin, M. A. Morozova, Yu A. Filimonov, Yu V. Khivintsev, S. L. Vysotsky, V. K. Sakharov, and E. S. Pavlov. Magnonics: a new research area in spintronics and spin wave electronics. *Physics-uspekhi*, 58(10):1002–1028, 2015. ISSN 1063-7869. doi: 10.3367/ufne.0185.201510m.1099.

[109] A. V. Chumak, V. I. Vasyuchka, A. A. Serga, and B. Hillebrands. Magnon spintronics. *Nature Physics*, 11(6):453–461, 2015. ISSN 17452481. doi: 10.1038/nphys3347.

[110] A. B. Ustinov, A. V. Kondrashov, A. A. Nikitin, A. V. Drozdovskii, and B. A. Kalinikos. Self-Generation of Chaotic Microwave Signal in Spin Wave Optoelectronic Generator. *Physics of the Solid State*, 60(11):2127–2131, 2018. ISSN 10637834. doi: 10.1134/S106378341811032X.

[111] Xu Yi, Qi Fan Yang, Ki Youl Yang, and Kerry Vahala. Imaging soliton dynamics in optical microcavities. *Nature Communications*, 9(1), 2018. ISSN 20411723. doi: 10.1038/s41467-018-06031-5.

[112] Pablo Marin-Palomo, Juned N. Kemal, Maxim Karpov, Arne Kordts, Joerg Pfeifle, Martin H. P. Pfeiffer, Philipp Trocha, Stefan Wolf, Victor Brasch, Miles H. Anderson, Ralf Rosenberger, Kovendhan Vijayan, Wolfgang Freude, Tobias J. Kippenberg, and Christian Koos. Microresonator-based solitons for massively parallel coherent optical communications. *Nature*, 546(7657):274–279, 2017. ISSN 14764687. doi: 10.1038/nature22387.

[113] Tobias J. Kippenberg, Alexander L. Gaeta, Michal Lipson, and Michael L. Gorodetsky. Dissipative Kerr solitons in optical microresonators. *Science*, 361(6402):eaan8083, 2018. ISSN 10959203. doi: 10.1126/science.aan8083.

[114] Krassimir Panajotov and Mustapha Tlidi. Chaotic behavior of cavity solitons induced by time delay feedback. *Optics Letters*, 39(16):4739, 2014. ISSN 0146-9592. doi: 10.1364/ol.39.004739.

[115] Heng Zhou, Yong Geng, Wenwen Cui, Shu Wei Huang, Qiang Zhou, Kun Qiu, and Chee Wei Wong. Soliton bursts and deterministic dissipative Kerr soliton generation in auxiliary-assisted microcavities. *Light: Science and Applications*, 8(1), 2019. ISSN 20477538. doi: 10.1038/s41377-019-0161-y.

[116] E. Lucas, M. Karpov, H. Guo, M. L. Gorodetsky, and T. J. Kippenberg. Breathing dissipative solitons in optical microresonators. *Nature Communications*, 8(1), 2017. ISSN 20411723. doi: 10.1038/s41467-017-00719-w.

[117] M. Riou, J. Torrejon, B. Garitaine, F. Abreu Araujo, P. Bortolotti, V. Cros, S. Tsunegi, K. Yakushiji, A. Fukushima, H. Kubota, S. Yuasa, D. Querlioz, M. D. Stiles, and J. Grollier. Temporal pattern recognition with delayed-feedback spin-torque nano-oscillators. *Physical Review Applied*, 12(2), 2019. ISSN 23317019. doi: 10.1103/PhysRevApplied.12.024049.

[118] Stuart Watt and Mikhail Kostylev. Reservoir computing using a spin-wave delay line active ring resonator. *Phys. Rev. Applied*, 2019.

[119] Ryosho Nakane, Gouhei Tanaka, and Akira Hirose. Reservoir Computing with Spin Waves Excited in a Garnet Film. *Ieee Access*, 6:4462–4469, 2018. ISSN 21693536. doi: 10.1109/ACCESS.2018.2794584.

[120] L. A. Lugiato and R. Lefever. Spatial dissipative structures in passive optical systems. *Physical Review Letters*, 58(21):2209–2211, 1987. ISSN 00319007. doi: 10.1103/PhysRevLett.58.2209.

[121] Amdad Chowdury, Wieslaw Krolikowski, and N. Akhmediev. Breather solutions of a fourth-order nonlinear Schrödinger equation in the degenerate, soliton, and rogue wave limits. *Physical Review E*, 96(4), 2017. ISSN 24700053. doi: 10.1103/PhysRevE.96.042209.

[122] Chen Yue, Dianchen Lu, Muhammad Arshad, Naila Nasreen, and Xiaoyong Qian. Bright-Dark and multi solitons solutions of $(3 + 1)$-dimensional cubic-quintic complex ginzburg-landau dynamical equation with applications and stability. *Entropy*, 22(2):202, 2020. ISSN 10994300. doi: 10.3390/e22020202.

[123] V. N. Serkin, A. Ramirez, and T. L. Belyaeva. Nonlinear-optical analogies to the Moses sea parting effect: Dark soliton in forbidden dispersion or nonlinearity. *Optik*, 192:162928, 2019. ISSN 00304026. doi: 10.1016/j.ijleo.2019.06.028.

[124] P. G. Kevrekidis, Wenlong Wang, G. Theocharis, D. J. Frantzeskakis, R. Carretero-González, and B. P. Anderson. Dynamics of interacting dark soliton stripes. *Physical Review A*, 100(3), 2019. ISSN 24699934. doi: 10.1103/PhysRevA.100.033607.

[125] J. L. Helm, S. L. Cornish, and S. A. Gardiner. Sagnac interferometry using bright matter-wave solitons. *Physical Review Letters*, 114(13):134101, 2015. ISSN 10797114. doi: 10.1103/PhysRevLett.114.134101.

[126] J. H. V. Nguyen, D. Luo, and R. G. Hulet. Formation of matter-wave soliton trains by modulational instability. *Science*, 356(6336):422–426, 2017. doi: 10.1126/science.aal3220.

[127] Oleksandr V. Marchukov, Boris A. Malomed, Maxim Olshanii, Vanja Dunjko, Randall G. Hulet, and Vladimir A. Yurovsky. Quantum fluctuations of the center-of-mass and relative parameters of NLS breathers, 2019.

[128] Oliver J. Wales, Ana Rakonjac, Thomas P. Billam, John L. Helm, Simon A. Gardiner, and Simon L. Cornish. Splitting and recombination of bright-solitary-matter waves. *Communications Physics*, 3(1):1–9, 2020. ISSN 23993650. doi: 10.1038/s42005-020-0320-8.

[129] Mark M. Scott, Boris A. Kalinikos, and Carl E. Patton. Self-generation of bright microwave magnetic envelope soliton trains in ferrite films through frequency filtering. *Applied Physics Letters*, 78(7):970–972, 2001. ISSN 00036951. doi: 10.1063/1.1347401.

[130] Philip E. Wigen and P. E. Wigen. Nonlinear Phenomena and Chaos in Magnetic Materials. In *Nonlinear Phenomena and Chaos in Magnetic Materials*, pages 1–12. World Scientific, 1994. doi: 10.1142/9789814355810_0001.

[131] Wonbae Bang, Jinho Lim, Jonathan Trossman, C. C. Tsai, and John B. Ketterson. Propagation of magnetostatic spin waves in an yttrium iron garnet film for out-of-plane magnetic fields. *Journal of Magnetism and Magnetic Materials*, 456:241–250, 2018. ISSN 03048853. doi: 10.1016/j.jmmm.2018.02.030.

[132] M. A. Ablowitz and P. A. Clarkson. *Solitons, Nonlinear Evolution Equations and Inverse Scattering*. Cambridge University Press, 1991. ISBN 9780521387309. doi: 10.1017/cbo9780511623998.

[133] Yuri S. Kivshar and Barry Luther-Davies. Dark optical solitons: Physics and applications. *Physics Report*, 298(2-3):81–197, 1998. ISSN 03701573. doi: 10.1016/S0370-1573(97)00073-2.

[134] Rina Kanamoto, Lincoln D. Carr, and Masahito Ueda. Topological winding and unwinding in metastable Bose-Einstein condensates. *Physical Review Letters*, 100(6):60401, 2008. ISSN 00319007. doi: 10.1103/PhysRevLett.100.060401.

[135] M. Abramowitz and I. A. Stegun, editors. *Handbook of Mathematical Functions*. National Bureau of Standards, Washington, D. C., 1964.

[136] Elizabeth Bradley and Holger Kantz. Nonlinear time-series analysis revisited. *Chaos*, 25(9):97610, 2015. ISSN 10541500. doi: 10.1063/1.4917289.